Winds in the Thermosphere of Mars: Exploring the Behavior of the Neutral Winds in the Upper Atmosphere and Examining Connections to the Lower Atmosphere

by

Kali Jean Roeten

A dissertation submitted in partial fulfillment
of the requirements for the degree of
Doctor of Philosophy
(Climate and Space Sciences and Engineering)
in the University of Michigan
2022

Doctoral Committee:

Research Professor Stephen W. Bougher, Chair
Professor Christiane Jablonowski
Associate Professor Emily Rauscher
Professor Aaron Ridley
Associate Professor Erdal Yiğit

Kali Jean Roeten
kjroeten@umich.edu
ORCID iD: 0000-0002-6942-0818

Dedicated to all my family.

ACKNOWLEDGMENTS

Thank you to the many people who have helped me in the process of finishing my PhD. I want to express my gratitude to my PhD advisor, Stephen Bougher, for all his help and encouragement. I would also like to thank my committee members, Christiane Jablonowski, Emily Rauscher, Aaron Ridley, and Erdal Yiğit. To all my co-authors of the three papers that were a part of this dissertation, thank you for your help and your collaboration; sincere thanks as well to all my collaborators who have allowed me to be a co-author on their projects. I am especially grateful to everyone on the MAVEN team; it has been a privilege to have been a part of that group. In addition, thank you to those individuals who have helped me learn how to use and troubleshoot the M-GITM model. Thanks as well to everyone in the CLaSP department, the faculty, staff, and fellow students who have helped me in the progress of this degree. I would also like to thank those at the Rackham Merit Fellowship for their support. Finally, thank you to all of my family and friends who have supported me throughout this process.

This PhD was supported through the NASA Earth and Space Science Fellowship (NESSF) program, under grant number 80NSSC18K1238. Additional funding was provided through the Rackham Merit Fellowship (RMF) program. Funding support was also provided by the MAVEN project.

PREFACE

Three of the chapters in this dissertation are fist-author publications that have already been published or have been submitted for publication. Chapter 2 has been published in the *Journal of Geophysical Research: Planets* [*Roeten et al.*, 2019]. Chapter 4 has been published in *Icarus* [*Roeten et al.*, 2022a]. Chapter 3 has been submitted and is under review.

The MAVEN/NGIMS datasets used in this work can be found on the NASA Planetary Data System at http://pds-atmospheres.nmsu.edu/data_and_services/atmospheres_data/MAVEN/ngims.html. The neutral wind measurements are an NGIMS Level 3 data product and the neutral densities are an NGIMS Level 2 data product. M-GITM output from simulations used in these studies can be found at the University of Michigan Deep Blue Data repository.

TABLE OF CONTENTS

LIST OF FIGURES

FIGURE

LIST OF TABLES

TABLE

ABSTRACT

This dissertation presents an analysis of the behavior of the neutral winds in the thermosphere of Mars, including impacts on this behavior due to coupling with the lower atmosphere. Using a 3-D ground to exobase Mars general circulation model called M-GITM (Mars Global Ionosphere-Thermosphere Model) and new in-situ thermospheric neutral wind observations at altitudes of $\sim$140-240 km from the MAVEN (Mars Atmosphere and Volatile Evolution) mission at Mars, the behavior of the winds in the upper atmosphere of Mars and different processes which drive them were examined. These model simulations and observations were also utilized to analyze the impacts of vertical coupling between the lower and upper atmosphere of Mars, focusing on two phenomena in particular: the effects of gravity waves propagating up from the lower atmosphere as well as the impacts of the most recent global dust storm.

In the first part of this analysis, M-GITM simulations are compared to five MAVEN wind observational campaigns. Some campaigns show a clear correspondence between measured velocities and simulated velocities. However, other campaigns show notable disparities between modeled and observed speeds, directions, or both. Since M-GITM is primarily driven by forcing from EUV heating at these altitudes, this indicates that those campaigns which M-GITM was able to replicate to a better degree are also primarily being driven by solar forcing. In the areas of poorer comparison, likely other physical processes not currently represented in the model play a larger role.

The second part of this analysis examines the impacts of one of those processes that was previously not included in M-GITM. A modern whole atmosphere, non-orographic gravity wave (GW) parameterization scheme was incorporated into M-GITM so that the effects of subgrid-scale GWs could be represented in numerical simulations of the upper atmosphere. In both equinox and solstice simulations, significant GW momentum deposition was seen at altitudes from $\sim$90-170 km, with average magnitudes of several hundred to over a thousand meters per second per sol. Additionally, mean thermospheric winds were reduced by up to a factor of two in the summer hemisphere, and mean temperatures above 120 km were cooler at most latitudes. Overall, the thermal and dynamical impact of these subgrid-scale GWs in M-GITM is substantial, indicating the importance of GWs as a coupling mechanism, and the need to include their effects in future modeling studies.

In the final section of this work, the MAVEN wind measurements are examined to determine whether the 2018 Mars global dust storm had an observable impact on the behavior of the thermospheric velocities. The campaign averaged wind speed increased slightly, up to nearly 200 m/s, near the onset of the storm before gradually decreasing during the mature phase of the storm. Substantial small-scale variability was seen during the peak of the storm and into the decay phase. However, the effects of changing local time and latitude of the MAVEN observations also need to be considered when interpreting the importance of the role of the dust storm on the behavior of the neutral thermospheric winds.

Overall, this work provides some of the first analysis of the MAVEN thermospheric wind observations, supported by numerical simulations from M-GITM. Through analysis of the impacts produced by lower atmospheric phenomena on observed and simulated thermospheric winds, this work also demonstrates the importance of vertical coupling in the Martian atmosphere.

CHAPTER 1

Introduction

1.1 Preface

Every ten years, a report is issued by the National Academies of Sciences, Engineering, and Medicine for several different scientific fields in order to identify the highest research priorities, highlight key questions, and propose recommendations based on input from that particular scientific community. In planetary sciences, this decadal survey process most recently released reports in 2012 and 2022. The 2012 document, titled "Vision and Voyages", has a section devoted to the understanding of physical processes currently acting in the Martian atmosphere. One key question it proposes is "what is the four-dimensional wind structure of the Martian atmosphere from the surface boundary layer to the upper atmosphere?" [*National Academies of Sciences*, 2011]. While there is still much to be learned regarding the characteristics of the winds and circulation pattern in the lower and middle atmosphere of Mars, much less is known for the upper atmosphere. The primary focus of this dissertation is to help improve the understanding of the neutral winds in the thermosphere of Mars and the physical processes that drive them, using a novel dataset of upper atmospheric wind velocity measurements from the MAVEN (Mars Atmosphere and Volatile Evolution) mission at Mars [i.e., *Benna et al.*, 2019], as well as numerical simulations from M-GITM (Mars Global Ionosphere-Thermosphere Model), a 3-D Mars general circulation model which extends from the surface to the exobase [i.e., *Bougher et al.*, 2015c]. Furthermore, in this dissertation, coupling between the lower and upper atmosphere will be examined through studies looking at how two lower atmospheric phenomena can impact the winds in the Martian thermosphere: upward propagation of gravity waves and the development of a global dust storm. The newest decadal survey for planetary science and astrobiology, "Origins, Worlds, and Life", also places emphasis on questions related to vertical coupling in atmospheres, asking "how do horizontally and vertically propagating waves drive planetary atmosphere dynamics?" [*National Academies of Sciences*, 2022]. The 2022 decadal survey also acknowledges the mysteries that remain surrounding development of global dust storms at Mars [*National Academies of Sciences*, 2022]. The potential

impacts of such a storm on the upper atmosphere have been previously examined through numerical simulations, but prior to having spacecraft like MAVEN at Mars, upper atmospheric datasets during a global dust storm have been extremely limited. With the aid of modern orbiting spacecraft such as MAVEN which have reached Mars in this decade, and supported by improvements to general circulation models like M-GITM, the effects which processes such as upward propagating gravity waves and the development of global dust storms can have on the upper atmosphere are being explored in ways that were not possible previously. Such exploration is the aim of the studies presentation in this dissertation.

1.2 Describing the Thermosphere of Mars

The uppermost layer of the Martian atmosphere, the thermosphere, is typically defined as extending from ∼100-250 km altitude, though the exact altitudes vary according to internal and external drivers [*Bougher et al.*, 2015a]. The bottom of the thermosphere is called the mesopause, where zonally averaged temperatures reach a local minimum with altitude. Traditionally, the top of the thermosphere, the exobase, is said to start where the mean free path equals the pressure scale height; essentially above which, the gas is so sparse it is considered collisionless [e.g. *Schunk and Nagy*, 2009]. Realistically, however, the exobase is not a line that can be drawn at a particular altitude, but consists of a more spatially extended transition between the collisional thermosphere and the kinetic dominated exosphere [*Bougher et al.*, 2015a]. As an example of the number densities observed by spacecraft in the thermosphere of Mars, the Viking 1 and 2 landers found densities of on the orders of approximately $10^6 - 10^{11}$ cm^{-3} during their descent through the thermosphere at altitudes of 120–200 km [*Nier and McElroy*, 1977]. Similar values were also observed by the orbiting MAVEN mission [*Mahaffy et al.*, 2015a] more recently, as shown in Figure 1.1. Although the thermosphere is the least dense region of the atmosphere, it can still largely be described using fluid equations.

One of the defining characteristics of the dayside thermosphere is an increase in temperature with altitude from the mesopause until temperatures become approximately constant with height in the upper thermosphere. Around the mesopause, mean temperatures around ∼100-120 K have been found from Mars Express / SPICAM (Spectroscopy for Investigation of Characteristics of the Atmosphere of Mars) derived temperature profiles [*Forget et al.*, 2009, e.g.], though colder temperatures, low enough to reach the CO_2 frost point, have also been observed [*Montmessin et al.*, 2006; *Forget et al.*, 2009]. Examples of exobase temperatures derived from MAVEN/NGIMS (Neutral Gas and Ion Mass Spectrometer) range from 130 K on the nightside and 260 K on the dayside [*Stone et al.*, 2018], as seen in Figure 1.2. Mean temperatures at 170-190 km derived from MAVEN/IUVS (Imaging Ultraviolet Spectrograph) observations of CO_2^+ UV doublet emissions

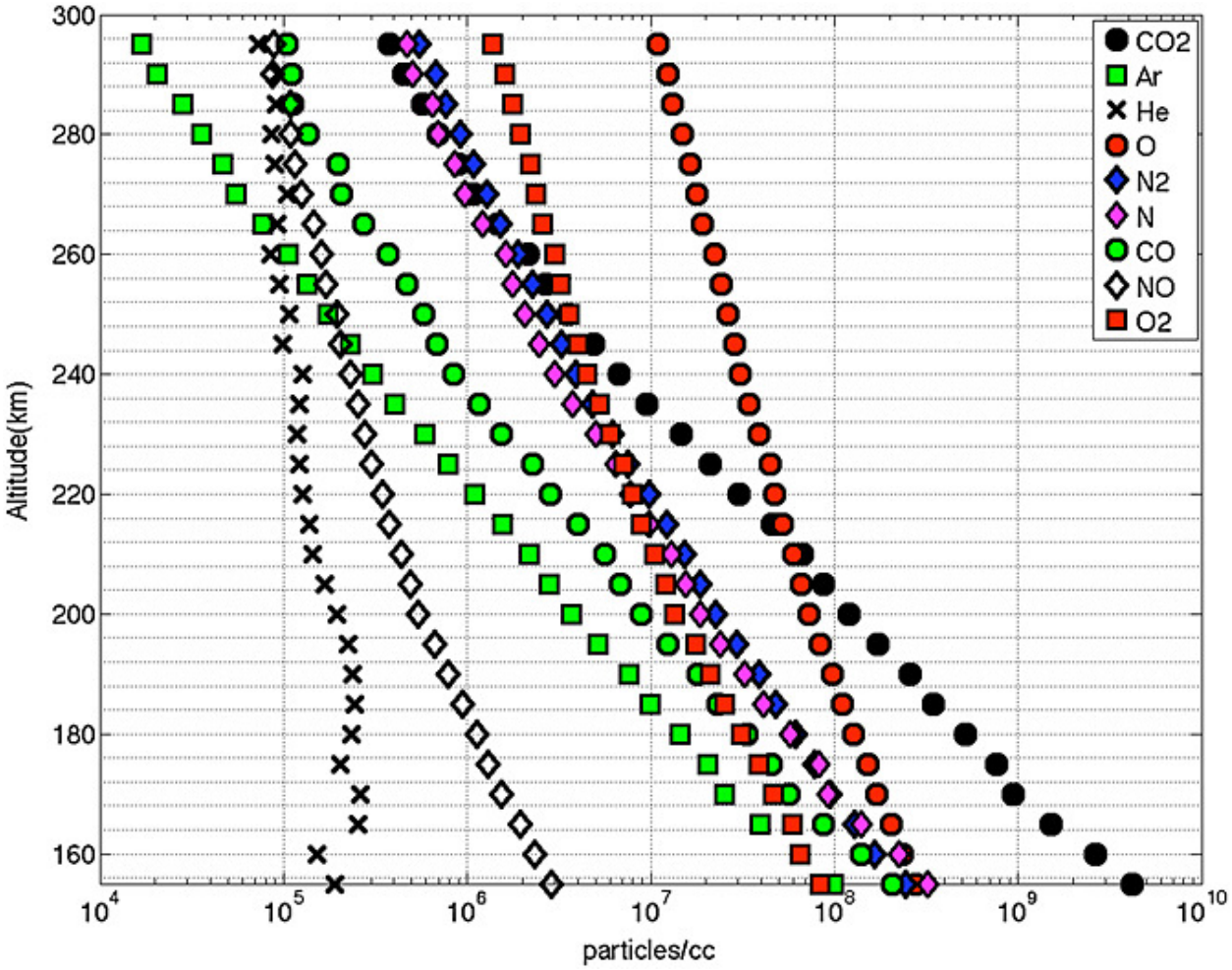

Figure 1.1: Vertical density profiles of several species found in the thermosphere of Mars measured by the Neutral Gas and Ion Mass Spectrometer (NGIMS) onboard the MAVEN spacecraft from *Mahaffy et al.* [2015a]. These profiles are averaged over several orbits near the $L_s = 288 - 326°$ season at a solar zenith angle of 45° [*Mahaffy et al.*, 2015a].

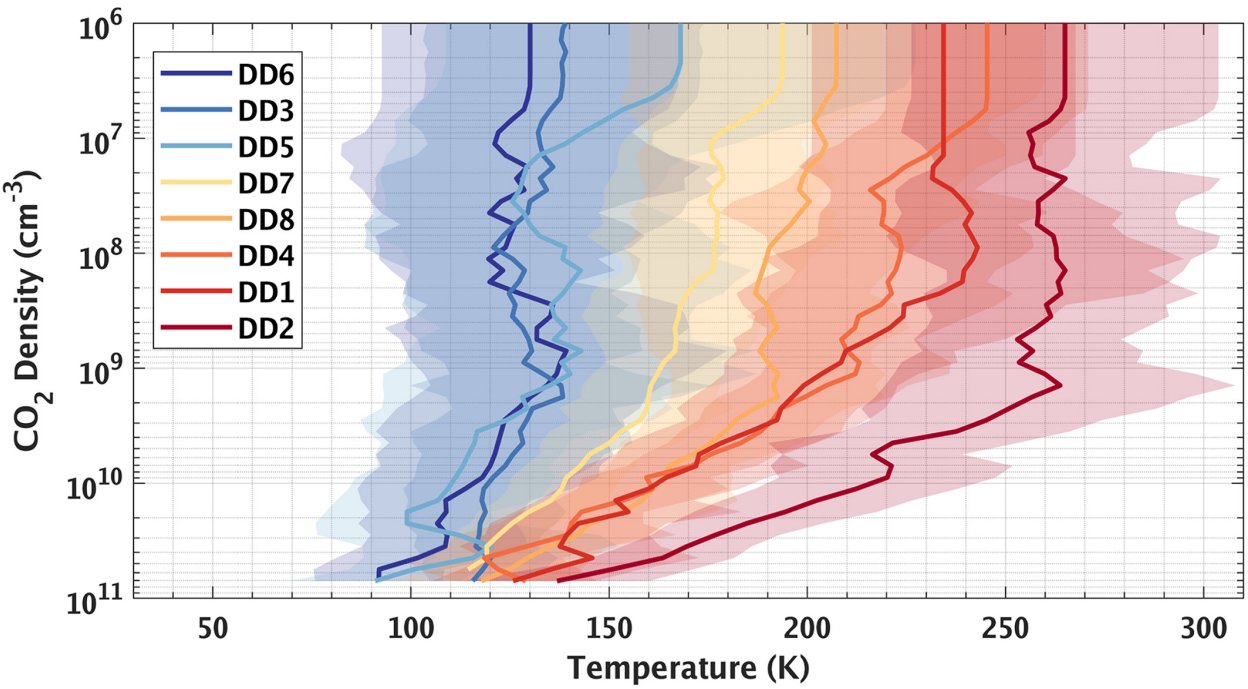

Figure 1.2: Averaged thermospheric temperature profiles derived from MAVEN/NGIMS density measurements for several special MAVEN observational deep dip campaigns (i.e., DD1, DD2, etc.) from *Stone et al.* [2018]. Shaded areas indicate the one-sigma variability. Campaigns also occur across different latitudes, local times, and seasons; see *Stone et al.* [2018] for further details. Altitudes of observations range from ∼125-270 km.

range from ∼130-300 K [*Jain et al.*, 2015; *Jain et al.*, 2021].

The increase in temperature in the dayside thermosphere is largely due to heating at these altitudes by absorption of solar extreme ultra-violet (EUV) radiation by the primary constituent of the thermosphere, CO_2. At altitudes near or above ∼200 km, the most abundant species in the thermosphere becomes atomic oxygen, a photodissociation product of CO_2 which also absorbs EUV radiation [e.g. *Bougher et al.*, 2017a]. EUV heating in the Martian thermosphere is primarily countered by cooling through molecular thermal heat conduction, which acts to redistribute heat in order to reduce the temperature gradient. On the dayside of the planet, EUV thermal energy deposited at higher thermospheric altitudes is conducted downward to ∼130-100 km or below. At these altitudes in the lower thermosphere, cooling by CO_2 15 μm emission plays a somewhat larger role in the energy balance than it does at higher altitudes [*Bougher et al.*, 1999].

Heat is redistributed from the dayside thermosphere to the nightside by global-scale winds. Local thermosphere heating and cooling occurs through horizontal temperature advection by the winds as well as from adiabatic heating and cooling associated with descending and ascending motions in the general circulation [e.g *Bougher et al.*, 2017a]. Modeling studies have suggested that in the thermosphere, near the dayside subsolar point (the location on the planet where the sun

is directly overhead), winds diverge and upwelling motions result in adiabatic cooling. On the nightside, converging winds and downwelling result in adiabatic heating [e.g. *González-Galindo et al.*, 2010; *Bougher et al.*, 2015c]. Thus, closely intertwined feedbacks exist between temperature and winds in the thermosphere.

Thermospheric densities, temperatures, and winds at Mars experience significant variability across a wide range of time scales due to both solar variability and different types of coupling processes with the lower atmosphere. In addition to diurnal variability, one of the most significant sources of upper atmospheric variability is the annual seasonal/orbital periodicity. Since the orbit of Mars is more eccentric than that of Earth, the variation in the solar EUV-UV flux over the course of a year solely due to the changing heliocentric distance (from 1.38-1.67 AU over the course of Mars' orbit) is relatively large, at 44% [e.g. *Bougher et al.*, 2017a].

At Mars, a common way to describe progression of time during the year is through solar longitude, L_s, with a full year consisting of 360°, starting with $L_s = 0°$ at northern hemisphere vernal equinox, and the middle of the year at $L_s = 180°$, the northern hemisphere autumnal equinox. At Mars, the cardinal seasons of northern hemisphere winter solstice (i.e. southern hemisphere summer solstice, $L_s = 270°$) and northern hemisphere summer solstice (i.e. southern hemisphere winter solstice $L_s = 90°$) align relatively closely in time with perihelion (when Mars is closest in its orbit to the Sun, $L_s = 251°$) and aphelion (when Mars is farthest from the Sun, $L_s = 71°$), respectively. In the thermosphere, at a constant pressure level, mean temperatures are warmer during the perihelion season than the aphelion season [e.g. *Forget et al.*, 2009; *González-Galindo et al.*, 2009]. Near the mesopause, the difference between perihelion and aphelion average temperatures has been found to be 10-20 K [*Forget et al.*, 2009], while from ∼150-180 km on the dayside, a temperature difference of 50 K has been found between these two seasons [*Jain et al.*, 2015], and dayside temperatures at the exobase are suggested to vary by up to ∼100 K seasonally [*González-Galindo et al.*, 2009; *Bougher et al.*, 2002]. Due to both seasonal solar flux and increased dust concentrations (and thus increased aerosol heating) in the lower atmosphere, the lower atmosphere is on average warmer during this season as well and expands, causing the rest of the atmosphere to expand with it, so densities at any given altitude in the thermosphere will also be greater during the perihelion season. This effect is seen repeatedly across various spacecraft observations when comparing perihelion and aphelion seasons, including in Mars Express / SPICAM temperature profiles [*Forget et al.*, 2009], density measurements extracted from MGS (Mars Global Surveyor) electron reflectometry data [*Lillis et al.*, 2010], and when comparing MGS and MRO (Mars Reconnaissance Orbiter) accelerometer derived mass densities [*Bougher et al.*, 2017a].

Considering the winds in the atmosphere of Mars, until recently, more extensive modeling studies and observable proxies for the general circulation in the lower to middle atmosphere (below 90 km) have been available. In the lower to middle atmosphere, zonal gradient winds were de-

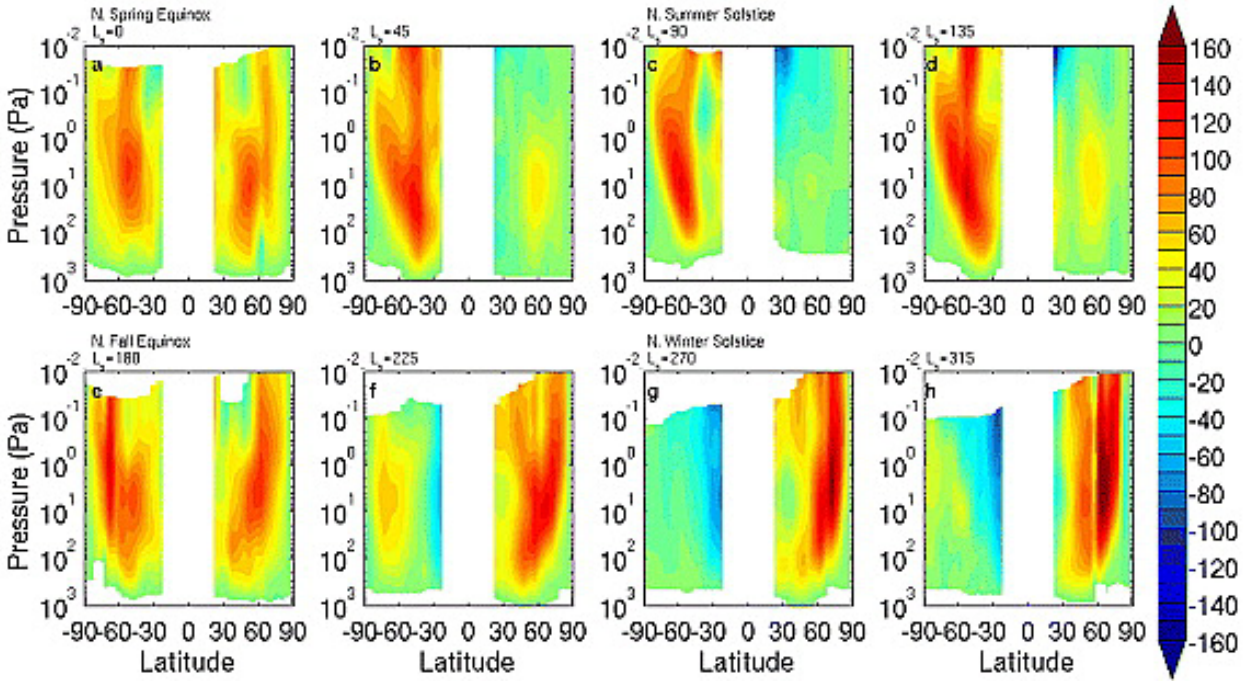

Figure 1.3: Mean dayside zonal wind velocities (m/s) calculated from MRO/MCS data from *McCleese et al.* [2010]. Data comes from Mars Year 29 with L_s bins labeled at the top of each individual panel, at altitudes from the surface to ∼80 km [*McCleese et al.*, 2010].

rived from MRO/MCS (Mars Climate Sounder) temperature data using the thermal wind relation [*McCleese et al.*, 2010] (see Figure 1.3). It was seen that at equinox, westerly winds exist in each hemisphere at mid latitudes, symmetrical to the equator. This symmetry does not remain long after the equinox, but rapidly changes to the solstical pattern of strong westerlies in the winter hemisphere and easterlies in the summer hemisphere [*McCleese et al.*, 2010; *Heavens et al.*, 2011a; *Barnes et al.*, 2017]. Modeling studies assimilating available data indicate that the strongest zonal mean winds occur during the perihelion season at high latitudes in the northern winter hemisphere (the increased solar insolation during perihelion produces the greatest summer to winter temperature gradient) [*Lewis et al.*, 1999; *Barnes et al.*, 2017]. From MRO/MCS data, these westerly jets are centered roughly at 0.1-10 Pa, or ∼40-60 km [*Barnes et al.*, 2017]. Such studies also strongly indicate that during the equinox, the accompanying meridional circulation is roughly Earth-like, with two Hadley cells centered at the equator. However, during the solstices, the mean meridional circulation is dominated by a large interhemispheric overturning cell that connects the summer to the winter hemisphere. Like the mean zonal winds, the most intense meridional circulation is thought to occur during the perihelion season [*Barnes et al.*, 2017].

The seasonal cycle is also predicted to have notable impacts on the circulation in the upper atmosphere. While winds at these altitudes largely circulate from the subsolar region to the nightside

of the planet, the pattern of the flow will vary according to true season (i.e. due to obliquity). Models that extend through at least part of the thermosphere suggest that near the solstices, more of an interhemispheric circulation will develop, from summer hemisphere to winter hemisphere (see Figure 1.4), while during equinox, when the subsolar region is more centered on the equator, a more symmetrical but less intense flow results (see Figure 1.5) [e.g. *Bougher et al.*, 2000; *González-Galindo et al.*, 2009]. During the solstice, many models suggest that zonally averaged zonal winds in the thermosphere are predominantly easterly, centered in the summer hemisphere at low to middle latitudes (though there is some westerly flow at high latitudes over the evening terminator) [e.g *González-Galindo et al.*, 2009; *Bougher et al.*, 2015c]. The westerly jet in the lower-middle atmosphere is predicted to decrease in intensity with height, becoming close to mean zero or weak westerlies by $\sim$120 km [*González-Galindo et al.*, 2009] . However, the details of these features and their altitudes are dependent on what other kinds of forcings (such as small-scale waves and other subgrid-scale physical processes) are included in models in addition to radiative forcing. Meanwhile, the simulated meridional circulation above $\sim$90 km can be characterized as being strongly pole-to-pole [*González-Galindo et al.*, 2009; *Bougher et al.*, 2015c]. There may be some indication of this meridional circulation observable in the lower thermosphere ($\sim$100-130 km) in the form of a winter polar warming that has been attributed in part to this flow from the summer hemisphere to the winter pole, where descending motions are thought to generate the observed notable heating [*Bougher et al.*, 2006; *González-Galindo et al.*, 2009]. It is still unclear how closely this meridional circulation in the upper, or even the middle atmosphere is connected to the Hadley cell in the lower atmosphere. Some studies have suggested that the mean meridional circulation in the middle atmosphere could be partially decoupled with the one in the lower atmosphere, even though they have the same circulation direction [*Heavens et al.*, 2011a; *Guzewich et al.*, 2013]. The large scale meridional circulation in the thermosphere is maintained by large scale eddy fluxes, gravity wave momentum deposition, and the Coriolis effect [*Medvedev and Yiğit*, 2019]

In addition to the annual cycle, the solar flux received at Mars also varies with the eleven-year solar cycle [*Thiemann et al.*, 2018]. Since the solar cycle and seasonal cycle both have a large impact on the mean state of the thermosphere, they are often considered in tandem, especially in modeling studies. One estimate of the extremes of solar cycle plus seasonal variation (comparing conditions from perihelion at solar maximum with those from aphelion during solar minimum) of temperatures at the exobase based on available Martian observations indicated differences spanning $\sim$100-140 K [*Bougher et al.*, 2017a]. Modeling studies predict similarly large differences [e.g. *Bougher et al.*, 2000; *González-Galindo et al.*, 2009]. These seasonal plus solar cycle extremes are also predicted to produce notable variation in the strength of the circulation in the upper atmosphere as well. Between the aphelion solar minimum and perihelion solar maximum cases, maximum horizontal winds in the thermosphere are predicted to double [*Bougher et al.*, 2000].

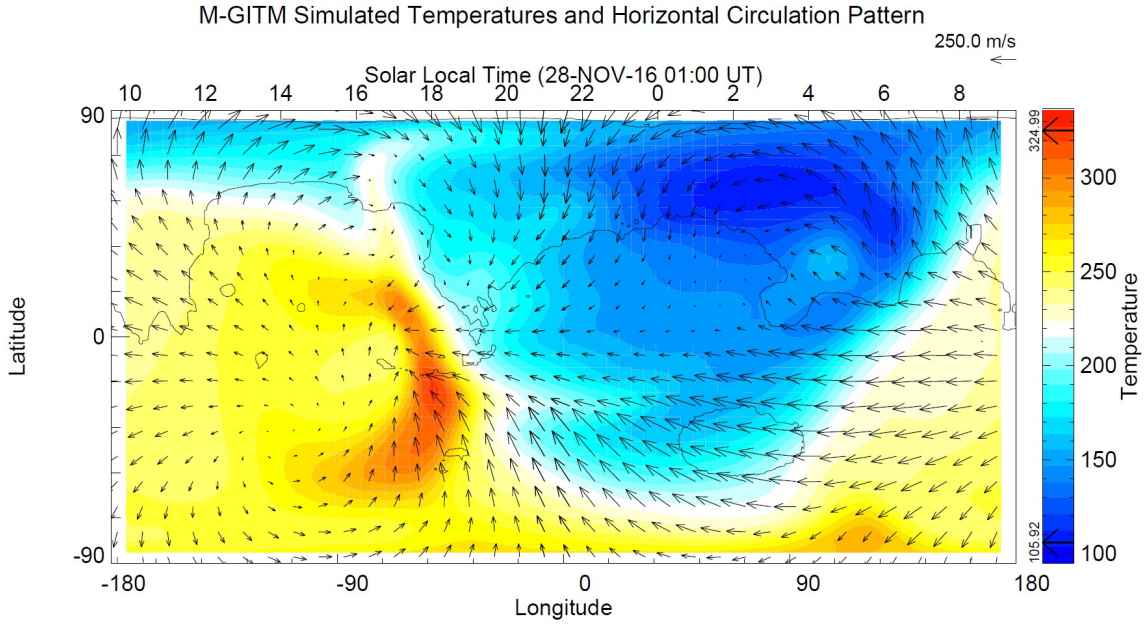

Figure 1.4: A M-GITM simulation for the $L_s = 270°$ solstice. A latitude-local time slice at 150 km. Colored contours show temperature (K) and vectors show wind velocities (m/s). (Note that this simulation does not include the effects of small-scale gravity waves.)

Though not the emphasis of this work here, solar fluxes received at Mars can also vary significantly on shorter time scales, which can also produce changes in thermospheric composition, temperatures, and likely wind velocities. This includes the effects of the 27-day solar rotation [e.g. *Forbes et al.*, 2006; *Hughes et al.*, 2022] and during episodic solar activity such as extreme flares [e.g. *Elrod et al.*, 2018; *Jain et al.*, 2018].

1.3 Connections to the Lower Atmosphere

In addition to responding to direct solar forcing from above, the Martian thermosphere is also coupled to the atmosphere below. An increase in the number of observations of the Martian middle and upper atmosphere in recent years as well as more sophisticated modeling has allowed for more studies of the nature of this vertical coupling. While many aspects are left to be explored, it has been found that waves, tides, and dust storms can also have a significant impact on thermospheric temperature structure and dynamics (see reviews by *Bougher et al.* [2015a]; *Bougher et al.* [2017a]; *Wu et al.* [2022]). In this work, two lower atmospheric phenomena that can impact the winds and temperature structure in the upper atmosphere will be highlighted: gravity waves and global dust storms.

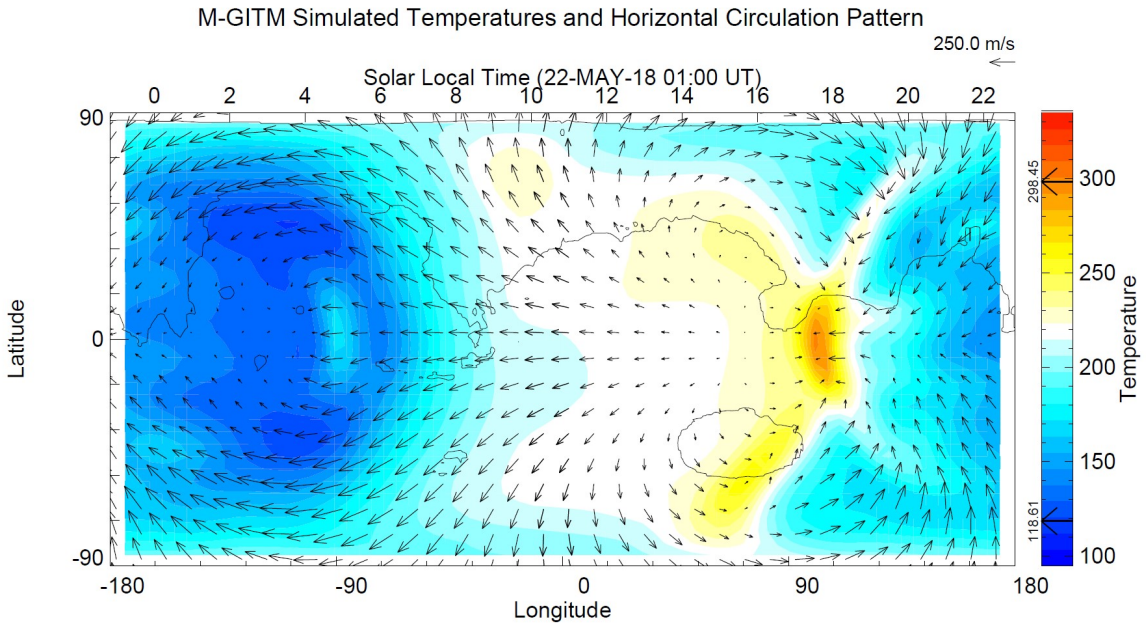

Figure 1.5: A M-GITM simulation for the $L_s = 180°$ equinox. A latitude-local time slice at 150 km. Colored contours show temperature (K) and vectors show wind velocities (m/s). (Note that this simulation does not include the effects of small-scale gravity waves.)

1.3.1 Gravity Waves

Internal gravity waves (GWs) are a common physical phenomenon in stably stratified planetary atmospheres, including that of Mars. Gravity waves are buoyancy waves, formed when something forces a displacement of air in a stable atmosphere, the stability causing the flow to oscillate as it tries to regain equilibrium [e.g. *Holton*, 2004]. GWs can be triggered in the lower atmosphere by flow over topography (orographic GWs), convection, vertical wind shear, and other various weather-related phenomena. Non-orographic GW sources produce a spectrum of waves with different phase speeds. Depending on their characteristics and the nature of the background environment, GWs can propagate vertically upward through the atmosphere over large distances, transferring energy and momentum from the lower atmosphere to the middle and upper atmosphere [e.g. *Yiğit and Medvedev*, 2015]. As such, they act as a coupling mechanism in the atmosphere. The background mean zonal winds the GWs propagate through can act to selectively filter GW harmonics. GW harmonics with faster phase speeds are more likely to reach higher altitudes, surviving filtering and dissipation [*Yiğit et al.*, 2008]. As waves propagate up in the atmosphere, their amplitudes increase exponentially as ambient atmospheric density decreases exponentially with height [e.g. *Yiğit and Medvedev*, 2015]. These waves are damped or dissipated in the upper

atmosphere. Wave breaking/saturation can occur due to nonlinear effects. GWs have nonlinear interactions with other waves and themselves; these interactions are scale dependent as smaller harmonics will interact with larger harmonics, producing a damping effect [*Yiğit et al.*, 2008]. GWs also undergo dissipation due to the effects of molecular viscosity, particularly at upper thermospheric altitudes. This dissipation/damping is how momentum and energy are transferred from the GW disturbances to the mean flow. The divergence of the GW momentum flux produces a body force per unit mass that acts to accelerate or decelerate the mean flow. GWs can also have thermal effects on the background atmosphere resulting from differential cooling or heating caused by the downward transport of the sensible heat flux, as well as from irreversible heating due to transfer of mechanical energy into heat [e.g. *Yiğit and Medvedev*, 2015].

Evidence of GW effects in the middle and upper atmosphere of Mars has been identified in an increasing number of observations. For instance, analysis of density observations obtained during MGS and Mars Odyssey aerobraking found GW momentum deposition (i.e., GW drag) at $\sim$100 km on the order of 1000 m/s/sol at thermospheric altitudes, with apparent horizontal scales of tens to hundreds of km [*Fritts et al.*, 2006]. This study also found that GW amplitudes vary with season, and are larger in winter and at middle to high latitudes. Another analysis of the MGS accelerometer data identified GWs with dominant horizontal wavelengths of 100-300 km along the orbital path [*Creasey et al.*, 2006]. This study found no clear correlation of thermospheric GW activity with underlying topography, indicating that orographic waves may not be the main source of GW activity in the upper atmosphere [*Creasey et al.*, 2006]. In addition to MGS and Mars Odyssey, GW-induced density perturbations have also been found in aerobreaking density datasets from MRO and ExoMars Trace Gas Orbiter [e.g. *Tolson et al.*, 2007; *Vals et al.*, 2019; *Jesch et al.*, 2019]. Several analyses have looked at GW induced density perturbations in the MAVEN/NGIMS dataset to try to further characterize thermospheric GW activity [e.g., *Yiğit et al.*, 2015; *England et al.*, 2017; *Terada et al.*, 2017; *Siddle et al.*, 2019]. GW activity in these studies has been found over all thermospheric altitudes, starting from the lowest altitudes of MAVEN's trajectory ($\sim$125 km) [*Siddle et al.*, 2019] up to $\sim$250 km [*Yiğit et al.*, 2015]. These GW-induced density perturbations can be up to 20-40% of the background density, though this varies with local time, altitude, and latitude [*Yiğit et al.*, 2015]. One NGIMS analysis suggested that GWs at these altitudes could generate a heating/cooling rate of up to several hundreds of Kelvin per sol [*England et al.*, 2017]. Overall, these observations demonstrate the presence of small-scale GWs with horizontal wavelengths of tens to hundreds of kilometers in the thermosphere, where they can induce notable variability, and seem to have significant dynamical and thermal implications for the mean flow and temperature structure.

In addition to the observations, modeling studies have suggested that GWs are a key coupling mechanism due to the dynamical and thermal effects in the thermosphere. The linearized 1-D full

wave model from *Parish et al.* [2009] first demonstrated that GWs originating from the Martian lower atmosphere could propagate into the thermosphere. Following this study, a few Mars general circulation models (GCMs) which extended to the upper atmosphere began incorporating the effects of subgrid-scale GWs. Since typical GCMs cannot resolve small-scale GWs, this requires the use of parameterization schemes to compensate for the missing physical impacts GWs produce in the real atmosphere. When the Max Planck Institute Mars GCM (MPI-MGCM) began to include a whole atmosphere, non-orographic GW parameterization scheme [*Yiğit et al.*, 2008] in their global model, a very strong dynamical influence of the subgrid-scale GWs was seen on the mean winds (especially decelerating the zonal wind and producing jet reversals) at altitudes of ∼100-130 km (i.e., up to the top altitudes of their model) [*Medvedev et al.*, 2011b]. Another study by *Medvedev and Yiğit* [2012] extended the top altitude of that GCM to ∼160 km, while also examining the thermal effects of subgrid-scale GWs. That study found a much cooler mesosphere and lower thermosphere, especially in the winter hemisphere, where the zonal mean temperature decreased by over 45 K after the GW parameterization scheme was added into the model [*Medvedev and Yiğit*, 2012]. While some other Mars GCMs include the effects of small-scale GWs, there is a limited number that both include the effects of GWs and extend through the thermosphere. Another Mars GCM that extends from the surface through the thermosphere and includes a GW scheme is the LMD-MGCM (Laboratoire de Météorologie Dynamique Mars GCM) [e.g. *González-Galindo et al.*, 2009]. However, the LMD-MGCM only includes a scheme for orographic GWs, currently.

1.3.2 Dust Storms

At Mars, dust suspended in the atmosphere plays a significant role in the weather and climate. Dust has a major influence in the lower atmosphere of Mars due to aerosol heating [e.g. *Kahre et al.*, 2017]. Dust is not transported to the upper atmosphere, typically staying below 15-25 km [*Heavens et al.*, 2011a] except during the largest dust storms, in which it has a greater vertical extent but still does not reach the thermosphere. Therefore, dust does not directly impact the thermosphere; however, large-scale dust storms seen in the lower atmosphere have been found to have indirect impacts in the thermosphere. While small, local dust storms can happen throughout the year, the largest regional storms and global storms are typically only observed within the part of the year near perihelion called the dust storm season, from $L_s = 210 - 330°$ [e.g. *Cantor et al.*, 2001]. Every Mars year during dust storm season, three large-scale regional dust storms typically occur. These events are large enough to produce appreciable warming even up to the middle atmosphere, around 50 Pa (∼25-30 km), and some even trigger a mirrored dynamical warming in the opposite hemisphere [*Kass et al.*, 2016]. A couple of studies have also suggested the impact of these large-scale storms can also be felt at higher altitudes. For example, zonal winds derived

from MGS accelerometer and rate data were found to increase by more than 100 m/s, peaking at 300 m/s, during a large-scale regional storm [*Baird et al.*, 2007]. However, in the thermosphere, the largest impacts may be expected from the largest dust storms Mars produces - the global dust storm (or alternatively, planet encircling dust event, PEDE). These storms can cover most or all of the planet in a dust haze within a couple of weeks from their initial onset, and then over the course of several months, will decay back to the seasonally typical state for the atmosphere [e.g. *Kass et al.*, 2020; *Kahre et al.*, 2017]. Global dust storms only occur approximately every one out of three Mars years [e.g. *Kahre et al.*, 2017], though the processes that control the formation of global dust storms in some years and not others are very poorly understood [*Kahre et al.*, 2017]. The most recent global dust storm, which occurred in 2018, provided a significant opportunity for novel studies since a larger fleet of spacecraft was operating at Mars at this time than during previous global dust storms, and notably, orbiting spacecraft such as MAVEN were in place to study the impact of the storm on the upper atmosphere. For instance, analysis of data from both MAVEN and India's Mars Orbiter Mission suggest that thermospheric densities increased by a factor of 2-3 [*Elrod et al.*, 2020; *Venkateswara Rao et al.*, 2020]. Additionally, MAVEN/IUVS data suggested the dayside thermosphere warmed $\sim$20 K during the early stage of the storm [*Jain et al.*, 2020]. More details about the development of the 2018 global dust storm and impacts seen in the thermosphere are presented in Chapter 4.

1.4 Using Observations to Explore the Winds in the Upper Atmosphere of Mars

It can be challenging to determine, characterize, and understand the behavior of the winds in a planet's upper-most atmosphere, as well as the relative importance and variability of the physical processes that produce and modify this behavior. At Mars, traditional wind sensors have typically been limited to those at the surface, within the meteorology suite of sensors onboard landers and rovers [e.g. *Martinez et al.*, 2017]. Nonetheless, winds above the Martian surface at various altitude ranges have been able to be inferred through a couple different methods. Mean zonal winds in the lower to middle atmosphere have been inferred through application of the gradient wind relation on the temperature structure observed by MRO/MCS. Using this technique, westerly jets were identified at mid-latitudes in both hemispheres near the equinox, and one strong westerly jet at mid-latitudes in the winter hemisphere during solstice [*McCleese et al.*, 2010]. At altitudes of $\sim$60-80 km, east-west wind speeds were able to be calculated from the movement of CO_2 clouds found mostly at low latitudes in Mars Express observations. Primarily easterly winds were identified, with speeds ranging from $\sim$5-100 m/s with an accuracy of $\pm$15-20 m/s [*Määttänen et al.*, 2010].

Furthermore, NO nightglow emissions in the middle atmosphere (centered ∼70-80 km) are a good indicator of locations of downwelling in the atmosphere, and thus give insight about the general circulation around these altitudes [e.g. *Bertaux et al.*, 2005; *Schneider et al.*, 2020]. One such recent study found a nightglow emission peak form at low latitudes near equinox, and enhanced polar emissions during the winter solstices [*Schneider et al.*, 2020]. This implies downwelling occurs on the nightside of the planet, especially near the winter pole during solstice and also near the equator during equinox.

Historically, in the upper atmosphere of Mars (above ∼100 km) even fewer observations of winds, direct or indirect, are available. The key example of previous extant upper atmospheric wind observations is that of zonal winds derived from MGS accelerometer and rate data while the spacecraft was undergoing aerobraking to change its orbit. In that study, mean wind speeds typical of ∼75-200 m/s were calculated over an altitude range of 115-135 km, during the northern hemisphere winter season [*Baird et al.*, 2007].

1.5 The MAVEN/NGIMS Neutral Wind Observations

To address the lack of other observational data on the winds in the upper atmosphere of Mars, starting in April 2016, the MAVEN mission at Mars developed a novel technique that allowed the NGIMS instrument to be able to measure horizontal neutral wind velocities in-situ along the spacecraft's trajectory, at altitudes of ∼140-240 km [*Benna et al.*, 2019]. This has provided a dataset that can be used to help characterize the winds in the upper atmosphere of Mars across a range of latitudes, local times, and seasons.

The MAVEN spacecraft began its primary science mission in Mars orbit in November 2014 [*Jakosky et al.*, 2015]. Exploring atmospheric escape and Mars aeronomy, one of MAVEN's key science objectives is to "measure the composition and structure of the upper atmosphere and ionosphere today, and determine the processes responsible for controlling them" [*Jakosky et al.*, 2015]. One of several instruments included onboard the spacecraft to meet this objective is NGIMS, a quadrupole mass spectrometer. The NGIMS instrument samples neutral and ion species through two inlets (a closed source and open source), ionizes the neutrals, and then uses a quadrupole mass filter which allows ions of specific charge to reach a counting detector [*Mahaffy et al.*, 2015b]. Thus, NGIMS provides in-situ measurements of the neutral gas and ambient ion composition of the upper atmosphere and how it varies with altitude, latitude, longitude, local time, and season over the course of the MAVEN mission [*Mahaffy et al.*, 2015b]. MAVEN's unique science orbit is key to making measurements across a range of conditions. The science orbit was elliptical to allow in-situ sampling throughout the thermosphere, down to the nominal periapsis altitude of ∼150 km. The periapsis of MAVEN's orbit also precesses in time, moving gradually in latitude and local

time. The science orbit is such that over the course of about five spacecraft orbits, and the periapsis of the trajectory would round the full 360° of longitude [*Jakosky et al.*, 2015].

In 2016, a new mode of operating NGIMS was developed that allows it to temporarily pause its nominal observations and begin to take measurements of horizontal neutral wind velocities in-situ along the spacecraft's trajectory near the periapsis segment of the orbit, from ∼140-240 km in altitude [*Benna et al.*, 2019]. This new measurement technique relies on the ability of the instrument's pointing direction to be adjusted. NGIMS is mounted on an articulated payload platform (APP) which during the wind measurement mode of data collection is rapidly nodded back and forth such that the instrument boresight pointing direction is varied ±8° off of the spacecraft ram direction. With the instrument using its retarding potential analyzer mode, cross-track and along-track wind speeds are then extracted from the observed modulations in the CO_2 abundance produced as NGIMS's pointing direction is changed. The measurement frequency is about 30 s, and it is assumed that winds do not change significantly during this time period. Between two successive measurements in a campaign, the spacecraft moves in space about ∼10 km vertically and ∼130 km horizontally [*Benna et al.*, 2019]. This technique also assumes that vertical velocities are negligible, which is generally considered a reasonable assumption outside of periods of extreme solar activity [*Bougher et al.*, 2015c]. Uncertainties are typical of 20 and 6 m/s for along- and across-track winds, respectively [*Benna et al.*, 2019]. Using spacecraft trajectory information, cross-track and along-track winds are reconstructed into Mars-referential zonal and meridional winds. The complete data reduction method can be found in *Benna et al.* [2019].

Since during wind observations, the typical ion and neutral abundance measurements from NGIMS have to be paused, winds are only observed in once-a-month campaigns, during which five to ten consecutive orbits are devoted to neutral wind measurements. During a typical two-to-three-day long wind observational campaign, NGIMS periapsis will traverse roughly the same trajectory in latitude, local time, and altitude (but over different longitudes). Over the course of a month between campaigns, however, the periapsis location will have shifted to a new latitude and local time sector [*Roeten et al.*, 2019]. Thus, over the course of two Mars years of wind campaigns, NGIMS has been able to take these observations over a variety of combinations of Mars seasons, latitudes, and local times. Note that most of the NGIMS wind observations were taken during the declining solar moderate phase of solar cycle 24 and into the following solar minimum, so while modeling studies suggest the solar cycle can impact upper atmospheric winds [e.g. *Bougher et al.*, 2015c], it is unlikely that this gradual change in solar conditions has had as large of an effect in driving changes between wind campaigns as other factors, such as changing season, latitude, and local time.

Most of the NGIMS neutral wind observations to date can be seen in Figure 1.6 as the separate sets of velocity whiskers plotted along a solid line which represents the trajectory of each

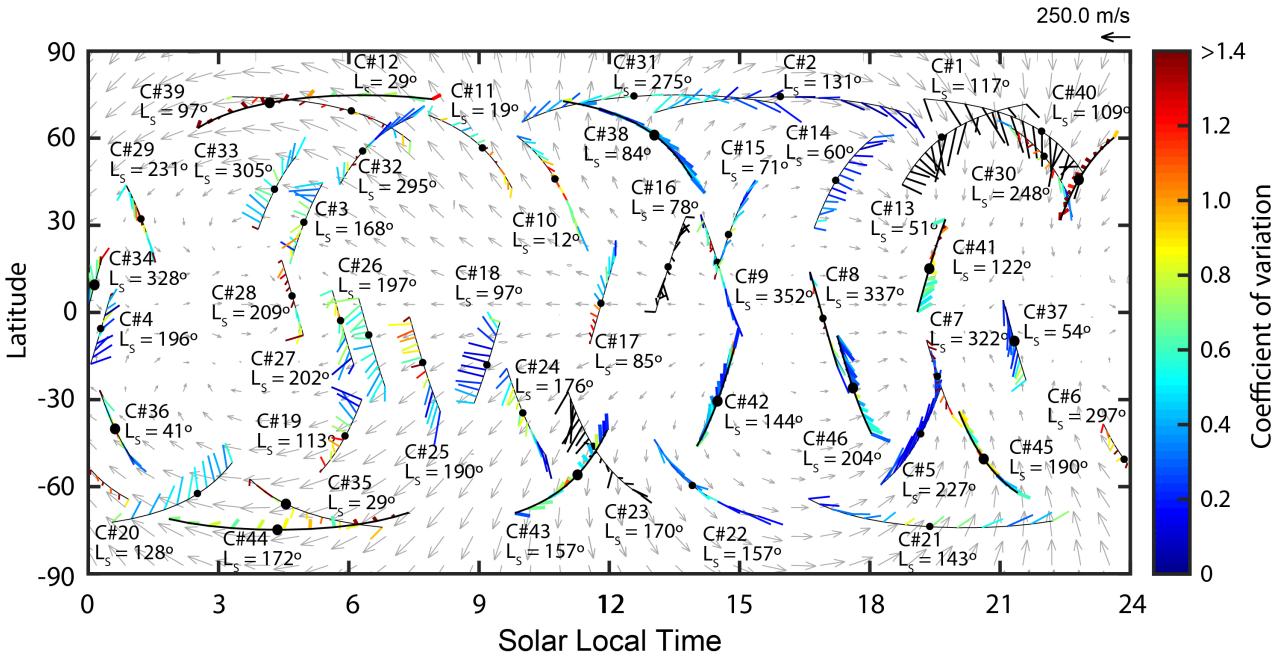

Figure 1.6: NGIMS neutral wind campaigns through 2020. Campaign-averaged wind velocities are plotted as whiskers along a black line (the trajectory of each campaign in latitude and local time). Colors represent a dimensionless measure of orbit-to-orbit variability in speed and direction, with higher values (redder colors) indicating greater variability (see Chapter 4 for a more detailed explanation). Black whiskers denote a single orbit observational campaign. Gray vectors are from an equinox simulation from the M-GITM model at 150 km. Text on the plot notates the number of each campaign and the season the observation occurred in. This is an updated version of the plot originally published in *Benna et al.* [2019], used with permission.

campaign. Though this dataset is just beginning to be explored, initial results from *Benna et al.* [2019] indicate winds that generally flow from the equatorial post-noon region on the dayside to the nightside, either as equatorial easterlies or through high-latitude transpolar eastward or westward flows. The high latitude flows tend to have less orbit-to-orbit variability, and higher wind speeds ($\sim$200 m/s or higher) compared to the areas of apparent divergence (post-noon) and convergence (post-dusk as well as predawn) which have slower and highly variable winds [*Benna et al.*, 2019].

1.6 Using Mars General Circulation Models to Explore the Winds in the Upper Atmosphere

For the Mars upper atmosphere, like at Earth, to counter a scarcity of observations, as well as to better understand the physical processes that shape the nature of available observations, general circulation models are often relied upon. Especially prior to the MAVEN/NGIMS wind measure-

ments becoming available, GCMs have been the main tool used to study the winds in the Martian upper atmosphere, providing an idea of what flow patterns and wind speeds might be expected at these altitudes. Even as more wind observations become available, GCMs will still be a key tool to explore the roles and impacts of different physical processes driving the winds in the upper atmosphere, and provide a more global picture across a range of conditions than observations will be able to provide for quite some time.

For Mars, a handful of GCMs have been developed that extend partially or completely through the upper atmosphere; a selection of these will be highlighted in this section (see the review chapter *Bougher et al.* [2017a] for a more thorough overview). The MGCM-MTGCM (Mars General Circulation Model – Mars Thermospheric General Circulation Model) coupled the NASA Ames MGCM, a lower atmospheric model, with MTGCM, a model that only simulates the upper atmosphere, in order to extend from the surface to 250 km [e.g. *Bougher et al.*, 1999; *Bell et al.*, 2007]. MGCM-MTGCM simulations produce a strong summer to winter interhemispheric circulation in the middle to upper atmosphere that is largely consistent with the circulation inferred through the NO nightglow emission observations [*Bertaux et al.*, 2005]. GCMs that seamlessly extend from the surface to the upper atmosphere are inherently more self-consistent than coupled codes. The Max Planck Institute Martian GCM (MPI-MGCM) has been gradually extended to higher altitudes in the upper atmosphere over several iterations, now reaching from the surface to altitudes of $\sim$160 km [*Hartogh et al.*, 2005; *Medvedev et al.*, 2013]. The MPI-MGCM was one of the first Mars GCMs extending at least partially through the upper atmosphere to employ a modern parameterization for the nonlinear effects of small-scale non-orographic gravity waves. The authors found notable gravity wave momentum deposition and thermal effects in the upper atmosphere up to the top of their model [*Medvedev et al.*, 2011a, b]. Results have also been published for MPI-MGCM simulations of two global dust storm scenarios at Mars, indicating that wind and temperature fields in the upper atmosphere could have a significant response to these events (generally, a warmer upper atmosphere, intensified zonal winds, and an altered meridional circulation) [*Medvedev et al.*, 2013]. Though only extending through the middle atmosphere, the MGCM of *Kuroda et al.* [2015] is also of note since it is one of the few high-resolution GCMs for Mars that extend to these altitudes ($\sim$80 km). This model can resolve gravity waves with horizontal wavelengths of $\sim$180 km and longer, which are subgrid-scale in conventional GCMs, and thus provide one way to validate the parameterization schemes employed in other GCMs. Initial comparisons with the MPI-MGCM find that the magnitude of gravity wave drag in the middle atmosphere is in good agreement with this high-resolution model [*Kuroda et al.*, 2016]. Another GCM that extends from the surface through the Martian upper atmosphere (up to $\sim$240 km) is the LMD-MGCM (Laboratoire de Météorologie Dynamique Mars GCM) [e.g. *Angelats i Coll et al.*, 2005; *González-Galindo et al.*, 2009]. It includes many physical processes relevant to the lower

atmosphere that other GCMs which focus on the upper atmosphere do not, such as CO_2 condensation and a water cycle [*Montmessin et al.*, 2004]. The circulation pattern in the upper atmosphere by the LMD-MGCM also is largely in agreement with NO nightglow patterns seen by Mars Express/SPICAM [*González-Galindo et al.*, 2008] and MAVEN/IUVS [*Schneider et al.*, 2020]. An orographic gravity wave scheme has also been implemented in this model to study the impact of this type of coupling between lower and upper atmospheric regions; it was found that these waves can modify the zonal mean winds, especially through interactions with tides at high winter latitudes [*Angelats i Coll et al.*, 2005]. This GCM has also produced a simulation of eight Mars years, two of which included global dust storms. These dust storms were found to notably modify the circulation in the upper atmosphere in the LMD-MGCM simulations [*González-Galindo et al.*, 2015].

1.7 The Mars Global Ionosphere-Thermosphere Model

The GCM used in the body of work presented in this dissertation is M-GITM, the Mars Global Ionosphere-Thermosphere Model. M-GITM is a finite difference model which extends from ground to 250 km, and runs with a 5° resolution in latitude and longitude and a constant vertical resolution of 2.5 km [*Bougher et al.*, 2015c]. M-GITM is based on the GITM code originally developed for Earth [i.e. *Ridley et al.*, 2006], but uses physical parameters, chemistry, and radiative processes appropriate for Mars [*Bougher et al.*, 2015c]. Much of the Mars-specific formulations in M-GITM have been imported from the MGCM-MTGCM code. Empirical albedo and thermal inertia maps for the initial prescription of surface temperatures used in M-GITM are the same as was employed in the NASA Ames GCM [*Haberle et al.*, 1999; *Haberle et al.*, 2003]. Initial atmospheric conditions in M-GITM are prescribed to be isothermal, globally uniform temperatures, with a standard density gradient that decreases exponentially with height [*Bougher et al.*, 2015c]. After an integration period of at least twenty days, steady state conditions are achieved and the initial conditions no longer impact simulated output. The modern M-GITM also employs solar fluxes from the FISM-M (Flare Irradiance Spectral Model-Mars) empirical model, which are derived from solar EUV fluxes measured at Mars by the MAVEN Extreme Ultraviolet Monitor instrument [i.e. *Thiemann et al.*, 2017]. In addition, a recent addition to M-GITM was the more realistic CO_2 15μm cooling scheme first used in the LMD-MGCM [i.e. *González-Galindo et al.*, 2013] to accurately portray the feedback of atomic O densities and diurnal temperature changes on cooling rates by this mechanism [*Roeten et al.*, 2019]. Furthermore, in one of the studies presented in Chapter 3 of this dissertation, the whole atmosphere gravity wave parameterization scheme used in the MPI-MGCM [i.e. *Yiğit et al.*, 2008; *Medvedev et al.*, 2011a] is added to M-GITM in order to help produce more realistic upper atmospheric conditions. M-GITM was specifically designed

with the goal of accurately representing the observed upper atmosphere structure as well as allowing investigation of the coupling of the upper atmosphere to the lower atmosphere [*Bougher et al.*, 2015c]. A more thorough description of M-GITM can be found in Chapters 2 and 3.

1.8 Dissertation Overview: Project Goals and Outline

The work presented in this doctoral dissertation primarily focuses on characterizing and understanding the winds in the thermosphere of Mars and the physical processes that drive them. A unique, new dataset of neutral wind observations from the NGIMS instrument onboard the MAVEN spacecraft and a 3-D ground-to-exobase GCM are used, separately as well as together, to explore the winds in the upper atmosphere and ask what sort of process may play an important part shaping the neutral flow at these altitudes, particularly those that can couple the lower and upper atmosphere. Three key research questions will be addressed as a part of this dissertation:

How well do simulations from a general circulation model that is primarily driven by solar forcing at thermospheric altitudes compare to the MAVEN/NGIMS neutral wind observations?

For this data-model comparison study, the M-GITM model is employed to compare to five NGIMS neutral wind campaigns at different locations, seasons, and local times to help assess how well we understand the processes that drive the winds at thermospheric altitudes. While the model appears to capture some of the observed flow, large differences elsewhere suggest that under certain conditions, physical processes not represented in the model may play a large role in shaping the neutral velocities. (Chapter 2)

How do the mean thermospheric winds and temperature structure respond to the effects of gravity waves which propagate up from the lower atmosphere?

A modern whole-atmosphere, nonlinear, non-orographic gravity wave parameterization scheme [*Yiğit et al.*, 2008] is incorporated into the M-GITM model. This allows M-GITM to include a representation of a subgrid-scale physical process which is believed to have a significant dynamical and thermal impact in the thermosphere, but was previously unaccounted for within the model. Numerical simulations are used to investigate the importance of small-scale GWs as a mechanism to couple the lower and upper atmosphere. The impact of these gravity waves is examined through mean differences in the simulated thermospheric temperature and velocity fields for both solstice and equinox seasons once GWs are accounted for within the model. (Chapter 3)

Do winds in the thermosphere respond to global dust storms at Mars?

A global dust storm in 2018 at Mars provided the relatively rare opportunity to study the potential response of the thermospheric winds to this extreme and long-lived Mars weather event using the MAVEN/NGIMS wind observations. The change in wind speed over the course of the storm is examined from the perspective of the trajectory of the MAVEN observations. The orbit-to-orbit variability in velocities throughout this time period is also characterized. (Chapter 4)

These research questions address an aspect of the Mars thermosphere system using a set of new and updated tools - the MAVEN/NGIMS wind observations and the M-GITM model, respectively. This provides a unique perspective to improve understanding of the behavior of thermospheric winds, particularly through an examination of two key ways physical phenomena originating in the lower atmosphere (i.e. small-scale gravity waves and global dust storms) can impact the winds in the thermosphere of Mars.

CHAPTER 2

MAVEN/NGIMS Thermospheric Neutral Wind Observations: Interpretation Using the M-GITM General Circulation Model

The content in this chapter was originally published in 2019 in *Journal of Geophysical Research: Planets*, under the same title, by K. J. Roeten, S. W. Bougher, M. Benna, P. R. Mahaffy, Y. Lee, D. Pawlowski, F. González-Galindo, and M. A. López-Valverde. *Roeten et al.* [2019] is presented here with modified formatting.

2.1 Abstract

Using a new observational technique, the NGIMS (Neutral Gas and Ion Mass Spectrometer) instrument on the MAVEN (Mars Atmosphere and Volatile Evolution) spacecraft has the unique capability to measure horizontal thermospheric winds. Measured along the orbit track from periapsis ($\sim$150 km) to $\sim$200 km, these are the first in-situ observations of thermospheric winds at Mars. Significantly, this also means that simulated winds from a global circulation model can be compared to in-situ observations from this part of the Martian atmosphere for the first time. In this study, observations from five NGIMS neutral wind campaigns have been compared to simulations from the Mars Global Ionosphere-Thermosphere Model (M-GITM), a ground to exosphere 3-D general circulation model. By comparing NGIMS neutral wind observations to model simulations, the processes driving the winds and their variations in the upper atmosphere are examined. These comparisons show that for certain observational periods, the M-GITM simulated winds can generally replicate the magnitude and/or direction of the NGIMS wind observations, while in others, significant differences occur. In general, wind observations from NGIMS campaigns with large orbit-to-orbit variability are not well replicated by M-GITM, while campaigns with higher observed wind speeds are better captured by the model. Additionally, using these data-model comparisons, the relative role of normal solar forcing and corresponding differential heating in driving

thermospheric winds at Mars is found to be variable, likely acting as the primary driver under some conditions and secondary to other physical processes under others.

2.2 Plain Language Summary

The MAVEN (Mars Atmosphere and Volatile Evolution) spacecraft, which is currently in orbit around Mars, has been taking monthly measurements of the speed and direction of the winds in the upper atmosphere of Mars between about 150 to 200 km above the surface. The observed wind speeds and directions change with time and location, and sometimes fluctuate quickly. These measurements are compared to simulations from a computer model of the Mars atmosphere called M-GITM (Mars Global Ionosphere-Thermosphere Model). This is the first comparison between direct measurements of winds in the upper atmosphere of Mars and simulated winds and is important because it can help to inform us what physical process are acting on the observed winds. Some wind measurements have similar wind speeds or directions to those predicted by the M-GITM model, but sometimes, there are large differences between the simulated and measured winds. The disagreements between wind observations and model simulations suggest that processes other than normal solar forcing may become relatively more important during these observations and alter the expected circulation pattern. Understanding the processes that drive the winds in the upper atmosphere of Mars provides key context for understanding how the atmosphere behaves as a whole system.

2.3 Background and Motivation

The thermosphere is a region of the upper atmosphere of Mars where absorption of solar extreme ultraviolet (EUV) radiation heats the atmosphere, causing temperatures to increase with height before approaching isothermal values near the exobase. It extends from the mesopause (the coldest region of the atmosphere, $\sim$100 km) to the exobase (the region where the atmosphere begins to transition to a predominantly collisionless environment, $\sim$200 km) [*Bougher et al.*, 2017a]. The thermosphere is strongly coupled with both the denser atmosphere below and the sparser exosphere above, and as such, regulates how energy and material flow into and out of the middle-lower atmosphere [*Bougher et al.*, 2015a].

Observations from several spacecraft have allowed for improved characterization of the upper atmosphere. This includes densities measured in-situ during the aerobraking campaigns of Mars Global Surveyor (MGS), Mars Odyssey, and Mars Reconnaissance Orbiter (MRO) [e.g. *Keating et al.*, 1998; *Tolson et al.*, 2005; *Keating et al.*, 2007], observations of airglow leading to derived temperatures and densities by the Mariner 6, 7, and 9 missions and Mars Express [e.g. *Stewart*,

1972; *Stewart et al.*, 1972; *Leblanc et al.*, 2006], and temperatures derived from stellar occultations conducted by Mars Express [e.g. *Forget et al.*, 2009]. Since 2014, the MAVEN mission, which was specifically designed to examine the upper atmosphere of Mars, has significantly added to the available observations of the Martian thermosphere by providing both in-situ [e.g. *Mahaffy et al.*, 2015a] and remote [e.g. *Jain et al.*, 2015] observations taken systematically across a range of conditions [*Jakosky et al.*, 2015].

However, prior to the beginning of wind measurements in 2016 by the NGIMS (Neutral Gas and Ion Mass Spectrometer) instrument onboard MAVEN [*Benna et al.*, 2019], no in-situ observations of thermospheric winds existed (see review by *Bougher et al.* [2017a]). The few previous indirect measurements of thermospheric winds available include zonal wind speeds unfolded from MGS accelerometer and rate data during the 1997-1998 Noachis dust storm event, in which wind speeds up to 200 m/s were estimated [*Baird et al.*, 2007]. Characteristics of horizontal wind circulation patterns in the upper atmosphere have also been inferred from nightglow emission distributions [e.g. *Gagné et al.*, 2013; *Stiepen et al.*, 2017].

Most of the current understanding of the expected Martian thermospheric winds is derived from 3-D GCMs (general circulation models) (see review by *Bougher et al.* [2017a]). One such GCM is the Mars Global Ionosphere-Thermosphere Model (M-GITM) [*Bougher et al.*, 2015c], used in the present study. Ground-to-exobase GCMs produce global circulation patterns and thermal structures expected for the thermosphere and thus can help overcome limited spatial and temporal coverage of observational data as well as, based on the physics included in the model, provide information about atmospheric processes not available from observations. However, simulated thermospheric winds have remained largely unconstrained due to the lack of comprehensive, and particularly, in-situ wind measurements (see review by *Bougher et al.* [2017a]).

Many Mars GCMs that extend into the thermosphere generally show a large-scale circulation pattern at these altitudes where strong winds transport heat and energy from the summer to winter hemisphere as well as from dayside to nightside [e.g. *González-Galindo et al.*, 2010; *Bougher et al.*, 1999; *Winchester and Rees*, 1995]. This general behavior is also seen in simulations from M-GITM [*Bougher et al.*, 2015c]. Under typical conditions, it is largely expected that pressure gradients set up by differential heating from in-situ absorption of EUV radiation drive the thermospheric circulation, which is also steered by the Coriolis effect. Note that the EUV flux and associated thermospheric heating vary with season and solar cycle [*Forbes et al.*, 2008]. Thus, the thermospheric circulation is expected to change over these timescales in response, as suggested by modeling studies [e.g. *Bougher et al.*, 2015c; *González-Galindo et al.*, 2009].

It has become increasingly apparent that winds play an important role in the thermosphere. Both modeling and observational studies of the Martian upper atmosphere have suggested an intricate system of feedbacks between dynamical, energetic, and chemical processes [*Bougher et al.*,

2017a]. For instance, while solar EUV heating in the thermosphere is believed to be offset primarily by cooling from thermal conduction (above $\sim$130 km), to a lesser degree, horizontal advection and adiabatic cooling (due to upwelling associated with divergence of horizontal flow) can also contribute [*Bougher et al.*, 1999]. The global scale circulation also impacts atmospheric composition in the upper atmosphere. For example, N and O atoms produced on the dayside are transported to the nightside by the general circulation where they combine into NO and produce observed nightglow emissions [e.g. *Bertaux et al.*, 2005; *Stiepen et al.*, 2017]. The influence of the global circulation on thermospheric composition can also be inferred from observations of a helium bulge on the nightside of Mars [*Elrod et al.*, 2017]. Helium is enhanced in this region due to the global circulation pattern which gives rise to large-scale convergence of horizontal winds and vertical downwelling, bringing Helium down from altitudes where diffusive separation causes it to be relatively more abundant [*Liu et al.*, 2014; *Keating and Prior*, 1968].

These, among other observations and modeling results strongly suggest that the dynamics of the upper atmosphere are complex and that thermospheric winds are strongly interconnected with other atmospheric processes and parameters. Thus, understanding wind patterns and their temporal variability in the Martian upper atmosphere is key to understanding the physical processes occurring in the thermosphere and their interactions. Data-model comparisons are an important method of improving this understanding.

To address this need, during the extended MAVEN mission, a new technique was developed which gave the NGIMS instrument the capability to measure horizontal neutral winds along and perpendicular to the spacecraft track. Notably, these are the first in-situ, direct measurements of thermospheric winds at Mars [*Benna et al.*, 2019]. By comparing this unique dataset to model simulations, physical processes that significantly contribute to driving the thermospheric winds and their variability can begin to be better identified as well as their relative importance under different conditions.

The rest of this paper will discuss the results of data-model comparisons using NGIMS wind observations and M-GITM simulations. In Section 2.4, the NGIMS wind observational technique and the M-GITM model will be described and the methodology behind the comparison will be outlined. In Section 2.5, the results of the comparison will be shown, and in Section 2.6, the implications of those results concerning the role of solar forcing and other physical processes in driving the winds will be discussed. Finally, Section 2.7 will summarize the main conclusions of this analysis.

2.4 Method

2.4.1 NGIMS Neutral Wind Observations

The NGIMS instrument is a quadrupole mass spectrometer originally designed to characterize the composition of the upper atmosphere and ionosphere of Mars [*Mahaffy et al.*, 2015a; *Benna et al.*, 2015]. The instrument collects its measurements by sampling neutral and ion species through two inlets and then utilizes a quadrupole mass filter. Further details of the NGIMS instrument and normal operations can be found in *Mahaffy et al.* [2015b].

In 2016, following two years of operations, a new observational technique was developed that enabled the NGIMS instrument to take regular measurements of horizontal neutral winds. During this mode, the normal data collection of NGIMS is paused to allow for wind observations to be conducted. The new wind measurement mode relies on the ability of the MAVEN spacecraft to rapidly and continuously vary the boresight pointing by nodding the articulated payload platform (APP) on which NGIMS is mounted back and forth by 8° off the spacecraft ram direction. Wind velocities were extracted from the observed modulations of neutral and ion fluxes as the instrument pointing direction changed. The data reduction procedure is detailed in [*Benna et al.*, 2019].

The resulting wind measurements were retrieved along an altitude range of around 140 - 240 km. Measurements were separated by the 30 seconds it takes for the instrument boresight to complete a full motion cycle. Reconstructed along- and across-track wind magnitudes have a random uncertainty typical of 20 m/s and 6 m/s, respectively. These uncertainties are mainly due to inherent errors in the reconstructed ephemeris of the spacecraft and the direction of the instrument boresight, in the energy resolution of the instrument's mass filter, and in counting statistics. Counting errors follow a Poisson distribution, errors from the quantization of analyzer steps follow a uniform distribution, and errors in reconstructed instrument pointing follow a normal distribution. Furthermore, if the wind fluctuates on timescales shorter than the 30 seconds it takes to nod the APP, this also adds to the overall uncertainty in the measurements. During the wind measurement retrieval process, the modulation seen by NGIMS during the 30 seconds it takes the APP to complete a motion cycle is compared to the expected modulation if constant winds are assumed. Poor fits to the expected modulation over 30 seconds would indicate uncertainties are greater than the values stated above [*Benna et al.*, 2019]. However, in all of the data points examined in this study, negligible variability was seen on the scale of seconds. This indicates no appreciable additional uncertainty was added on due to poor quality observations. The dataset of zonal and meridional wind measurements is a NGIMS Level 3 data product. Version 3, release 1 data was used (v03_r01).

Most wind measurements were collected in monthly campaigns. During a typical two to three day campaign, NGIMS conducted a set of consecutive 5-10 orbits of neutral wind observations over the same local time, latitude, and altitude region (but different longitudes). For the purpose

of comparing to the M-GITM model in this study, these 5-10 consecutive orbits were averaged to produce a campaign-average profile. This is a basic average of all velocity data points at a given latitude, local time, and altitude location over the time period of the campaign. Since very small differences exist in a sampling location in latitude, local time, and altitude from orbit to orbit due to the way in which the timing of periapsis is determined, NGIMS data was interpolated to the exact same locations before averaging. Note that for the profiles, averages were only calculated for the altitudes within the segment of the spacecraft's track which were sampled in all the orbits of a campaign. Campaign averaging is effectively also a longitudinal average, as the MAVEN periapsis traverses the planet in longitude once about every five orbits [*Jakosky et al.*, 2015], which is the typical length of a wind campaign. Thus, averaged over a campaign, any potential longitudinal variability in the winds should largely be smoothed out.

To examine the orbit-to-orbit variability potentially smoothed out by the averaging, the standard deviation of the measured velocities along the spacecraft's track was also calculated. The standard deviation of the zonal and meridional components over a campaign was found first, then this was used to find profiles of the zonal and meridional flow corresponding to 1-σ variability about the mean. These were then transformed to speed and direction and used to find a corresponding standard deviation in speed and direction.

While standard deviation can show the amount of variability in wind speed versus that of direction, another calculated statistical quantity called the coefficient of variation takes into account the coupled relationship between the two. The coefficient of variation provides a dimensionless scalar measure of the orbit-to-orbit variability of the winds related to both variability in direction and magnitude. The multivariate version of the coefficient of variation was determined from zonal and meridional components of the wind observations using the formulation from *Albert and Zhang* [2010]:

$$CV = \left[\mu^{\mathrm{T}}\Sigma\mu/(\mu^{\mathrm{T}}\mu)^2\right]^{1/2} \tag{2.1}$$

where μ is the mean and Σ is the variance-covariance matrix of the zonal and meridional components. Higher coefficients of variation can correspond to higher variability in either direction or speed, or variability in both. A minimum coefficient of variation value of zero indicates there is no orbit-to-orbit variability, while the higher the value, the more variability is present.

2.4.2 M-GITM Simulations

The general circulation model used in this study is the Mars Global Ionosphere-Thermosphere Model (M-GITM). M-GITM is a finite difference 3-D spherical model developed to address the physics of the entire Mars atmosphere from the surface to $\sim$250 km. Specifically, M-GITM was

designed to accurately represent the observed thermosphere-ionosphere structure and allow investigation of the coupling of the thermosphere-ionosphere to the lower atmosphere and exosphere [see *Bougher et al.*, 2015c]. The M-GITM framework is built from the terrestrial GITM framework [*Ridley et al.*, 2006] with Mars-specific fundamental physical parameters, ion-neutral chemistry, and radiative processes. M-GITM uses an altitude based vertical coordinate, allowing for a relaxation of the assumption of hydrostatic equilibrium. As a result, while horizontal neutral winds are solved in bulk, the momentum equation is solved separately in the vertical direction for each major species [*Bougher et al.*, 2015c]. M-GITM was run with a 5° resolution in latitude and longitude and a constant 2.5 km vertical resolution.

For the Mars lower atmosphere (0 – 80 km), M-GITM includes radiative processes and a basic dust distribution. For these altitudes, a correlated-k radiation code adapted from the NASA Ames Mars General Circulation Model (MGCM) [*Haberle et al.*, 2003] is used. This provides M-GITM with solar heating, variable aerosol heating, and CO_2 15 μm cooling for the region of the atmosphere in local thermodynamic equilibrium (LTE). A fast formulation of surface temperatures adapted from MGCM and based on Mars empirical temperatures is also included. Additionally, a basic dust scheme was included which uses a globally uniform and seasonally averaged visible dust opacity of τ = 0.5. For vertical extent of the dust, a Conrath parameterization scheme is used in which the dust is well mixed below a particular altitude and decays exponentially above [*Conrath*, 1975].

For the upper atmosphere ($\sim$80 – 250 km), M-GITM includes a formulation for non-local thermodynamic equilibrium (NLTE) CO_2 15 μm cooling, appropriate EUV and IR heating rates, and ion-neutral chemistry [*Bougher et al.*, 2015c]. Along with the 15 μm CO_2 cooling code, a correction for NLTE near-IR heating rates near the $\sim$80 – 120 km region of the upper atmosphere was included. The EUV-UV heating routines utilized in M-GITM are appropriate for a CO_2 atmosphere, using the relevant set of cross-sections and yields. This includes those specified for in-situ heating by EUV-UV, dissociation, and ionization rates over altitudes from $\sim$80 – 250 km [*Bougher et al.*, 2015c]. Additionally, over thirty key ion-neutral chemical reactions and associated rates [*Fox and Sung*, 2001] are used by M-GITM. Photochemical equilibrium is assumed for solving for the ionosphere in M-GITM. It should be noted that for the M-GITM simulations here, topography, the effects of the Martian crustal magnetic fields, and ion-neutral drag have not been implemented within the code.

Comparisons have been conducted between M-GITM simulations and MAVEN measurements over the first two years of the spacecraft's science mission. This includes comparisons for the first six Deep Dip campaigns (in which periapsis is lowered to $\sim$125 km) [*Bougher et al.*, 2015b; *Zurek et al.*, 2017] and dayside science orbits [*Bougher et al.*, 2017b]. These and other NGIMS/M-GITM comparisons have revealed M-GITM captures the basic dayside density variations in key species

as well as temperatures at low solar zenith angles, where solar forcing would be expected to be the dominant mechanism controlling thermospheric structure. Yet other comparisons, such as those with mass densities derived from MAVEN accelerometer measurements in *Zurek et al.* [2017], have shown that data-model comparisons are poor from midnight through the dawn terminator.

Notably, two recent upgrades have been included in the M-GITM code to improve data-model comparisons. First, a more realistic CO_2 NLTE 15 μm cooling scheme used in *González-Galindo et al.* [2013] and *Medvedev et al.* [2015] has been implemented in M-GITM to accurately capture the feedback of atomic O densities and large diurnal temperature variations on the cooling rates. Similar to what was observed by *González-Galindo et al.* [2013] with the inclusion of this code into the LMD MGCM (Laboratoire de Météorologie Dynamique Mars GCM) [*Angelats i Coll et al.*, 2005], by adding this new scheme into M-GITM, temperatures near the mesopause are cooler (see also *McDunn et al.* [2010]), which is in better agreement with the stellar occultation observations from the Spectroscopy for Investigation of Characteristics of the Atmosphere of Mars (SPICAM) instrument on Mars Express seen in *Forget et al.* [2009]. While this had little impact on the dayside thermospheric temperatures, it did decrease temperatures on the nightside even up to thermospheric altitudes. Overall, this scheme is a more accurate representation of the cooling process, particularly in the mesosphere and lower thermosphere regions.

The second upgrade incorporates the capability in M-GITM to make use of output from the FISM-M (Flare Irradiance Spectral Model - Mars) empirical model. FISM-M uses the solar EUV fluxes measured at Mars by the MAVEN EUVM (Extreme Ultraviolet Monitor) instrument to yield daily averaged full solar spectra from $\sim$0 – 190 nm in 10 nm bin intervals [*Thiemann et al.*, 2017]. The wavelength bins used by M-GITM were populated with these daily averaged datasets. This provides M-GITM with solar EUV fluxes corresponding to MAVEN-specific orbit measurements, allowing for a more accurate representation of solar forcing during each wind campaign. The FISM-M datasets used here were the Level 3 EUV daily products v10_r01 (for the first two campaigns) and v11_r04 (for the last three campaigns).

This upgraded M-GITM was run for the duration of the time periods corresponding to five NGIMS wind campaigns. With the newly incorporated FISM-M output, simulations of each different campaign have solar fluxes and seasonal conditions that, in as direct a manner as currently possible, correspond to those that occurred during each campaign. From these M-GITM simulations, winds were extracted along the same track flown by the MAVEN spacecraft (in latitude, altitude, and local time) using the spacecraft's trajectory information for each orbit in the campaign. These model flythroughs allow for a more direct comparison of M-GITM output to the in-situ NGIMS wind observations. Additionally, while extracting the flythroughs from any given orbit, the areocentric coordinate system natively used by M-GITM was converted to an areodetic coordinate system used by NGIMS, which slightly changes the way in which altitude is determined

based on whether the planet is considered spherical or an oblate spheroid, respectively, in these coordinate systems (for more information on the coordinate system used by MAVEN, see *Seidelmann et al.* [1/2002]). Finally, these M-GITM flythroughs were averaged over the entire campaign (still differentiating between inbound and outbound segments of the orbit), in the same way as the averaging was done with the NGIMS wind profiles, to create a campaign-averaged profile. In this process, to facilitate campaign averaging, M-GITM flythroughs were also interpolated to the same points in latitude, local time, and altitude as was done for the NGIMS profiles. Differences in the averaged simulated and observed velocity profiles were then calculated.

Note that averaging M-GITM flythroughs over the length of the campaign is primarily done to match the process used for the NGIMS data, and not because there is large intrinsic orbit-to-orbit variability produced by M-GITM. However, in the NGIMS data, as will be shown in later sections, the orbit-to-orbit variability can be very large. Averaging the NGIMS data over every orbit in a campaign, then, is done so that an average flow in that location might be identified, compared to the model, and examined for any trends over longer time periods.

2.5 Results

The first analysis of observations from NGIMS wind campaigns was presented by *Benna et al.* [2019]. In the current study, five NGIMS neutral wind campaigns were selected for further analysis in comparison with the upgraded M-GITM simulations described in Section 2.4.2. These specific campaigns - September 2016, January 2017, May 2017, December 2017, and February 2018 - were chosen so that campaigns spanning a range of latitudes, local times, and seasons would be represented in this analysis. Geophysical conditions for these select campaigns are included in Table 2.1.

In general, these data-model comparisons show that NGIMS neutral wind measurements in some cases are similar to M-GITM simulated winds, but in others do not match in speed, direction, or both. Campaign averaged speeds from NGIMS and the corresponding MGITM simulations are displayed in Table 2.2 and campaign averaged directions can be found in Table 2.3.

2.5.1 September 2016 Campaign

The September 2016 campaign was the first NGIMS wind campaign consisting of five consecutive orbits of neutral wind measurements over the course of two days. This campaign occurred over the southern mid-latitudes on the dayside, near the evening terminator, and near perihelion (see Table 2.1). Campaign averaged profiles are included in Figure 2.1, which show the direction and speed for both NGIMS observed winds (in blue) and M-GITM simulated winds (in red) as well as

Table 2.1: Geophysical characteristics of the five selected NGIMS wind campaigns

Orbits	Campaign Dates	Ls (deg) [a]	Local Time (hr)	Latitude (deg)
3861 – 3865	September 22–23, 2016	227 – 229	18.1 – 19.6	26°S – 60°S
4437 – 4446	January 11–13, 2017	297 – 299	23.4 – 1.2	38°S – 66°S
5170 – 5179	May 30 – June 1, 2017	12 – 13	9.7 – 11.5	30°N – 61°N
6198 – 6202	December 7–8, 2017	97 – 98	8.8 – 9.5	3°S – 32°S
6532 – 6541	February 7–9, 2018	126 – 127	0.0 – 3.5	73°S – 50°S

[a] Solar longitude

Table 2.2: Campaign averaged speeds (m/s)

	NGIMS			M-GITM		
Campaign	Average [a]	Range [b]	1-σ [c]	Average [a]	Range [b]	1-σ [c]
September 2016	317	262 – 357	55	161	103 – 200	12
January 2017	56	32 – 79	39	263	237 – 293	3
May 2017	117	61 – 149	39	154	136 – 177	2
December 2017	202	178 – 230	26	157	145 – 171	2
February 2018	221	200 – 247	80	129	116 – 146	2

[a] This average is both the campaign average and the average over all altitudes.
[b] The range of speeds seen in the campaign averaged altitude profile.
[c] The standard deviation of speed averaged over all altitudes.

Table 2.3: Campaign averaged direction (degrees from North)

	NGIMS			M-GITM		
Campaign	Average [a]	Range [b]	1-σ [c]	Average [a]	Range [b]	1-σ [c]
September 2016	17	-7 – 27	5	27	14 – 42	1
January 2017	188	161 – 230	67	289	281 – 300	4
May 2017	137	97 – 164	37	320	308 – 329	3
December 2017	298	275 – 328	21	240	220 – 257	1
February 2018	2	-19 – 27	27	-34	-39 – -28	3

[a] This average is both the campaign average and the average over all altitudes.
[b] The range of directions seen in the campaign averaged altitude profile.
[c] The standard deviation of direction averaged over all altitudes.

Table 2.4: Coefficient of Variation values for the selected campaigns

Campaign	Range	Average
September 2016	0.08 – 0.31	0.17
January 2017	0.72 – 1.92	1.26
May 2017	0.32 – 1.33	0.80
December 2017	0.08 – 0.73	0.28
February 2018	0.37 – 1.07	0.52

profiles that show the difference between the two (in purple). NGIMS observed high speeds during this campaign, on average over 300 m/s (see Table 2.2), which did not deviate much in direction throughout the entire altitude range. The September 2016 campaign saw a prevailing direction primarily to the north-northeast (or NNE, in the standard abbreviated directional notation, which will be used from this point forward), also seen in Figure 2.2, which shows velocity vectors from NGIMS observations along the spacecraft's track in latitude and local time.

As seen by the gray vectors plotted in Figure 2.2, measurements from each orbit are all largely consistent with each other. This can be demonstrated quantitatively by the coefficient of variation (described in Section 2.4.1), which is included in Table 2.4 for all campaigns and represented by the color of the campaign averaged vectors in Figure 2.2. Coefficient of variation values uniformly below 0.31 (compared to a maximum value of 1.92 seen over all selected campaigns) indicate very little orbit-to-orbit variability was observed in the September campaign.

Notably, the directions of the NGIMS observed winds and the M-GITM simulated winds are very similar. This can be seen in the profiles in Figure 2.1 and in comparing the colored averaged NGIMS and black averaged M-GITM vectors in Figure 2.2. Data and model wind directions are within 25° of each other throughout the altitude profile, and less than five degrees apart at periapsis. Both the observed and simulated wind headings also turn slightly more to the northwest or north, respectively, along the spacecraft track (approaching later local times and lower latitudes). Yet, with a simulated speed at about 160 m/s (averaged over the campaign and over all altitudes), M-GITM seems to be underpredicting the observed speed by over 150 m/s.

2.5.2 January 2017 Campaign

The January 2017 campaign lasted three days and consisted of ten consecutive orbits of neutral wind measurements. This campaign took place at a similar season and latitudes as the September 2016 campaign (see Table 2.1). Unlike the September 2016 campaign, the January 2017 campaign occurred at local midnight. As seen in the profiles in Figure 2.3, this campaign has much lower wind speeds than in the September 2016 case, with a campaign and profile average of $\sim$60 m/s. In contrast, M-GITM simulations are producing average horizontal wind speeds of $\sim$260 m/s. In addition to this $\sim$200 m/s difference in speed, the NGIMS averaged direction is over 90° separated from the M-GITM flythrough direction, with averaged NGIMS observed winds directed generally to the S to SW and M-GITM simulated winds to the NW.

However, this difference in direction and speed is impacted strongly by the large orbit-to-orbit variability in the NGIMS measurements seen in Figure 2.4. The coefficient of variation for this campaign ranges from 0.72 to 1.92 - values much greater than in the September 2016 campaign. Not only does the direction (and to a lesser extent, speed) vary widely between each orbit, but also

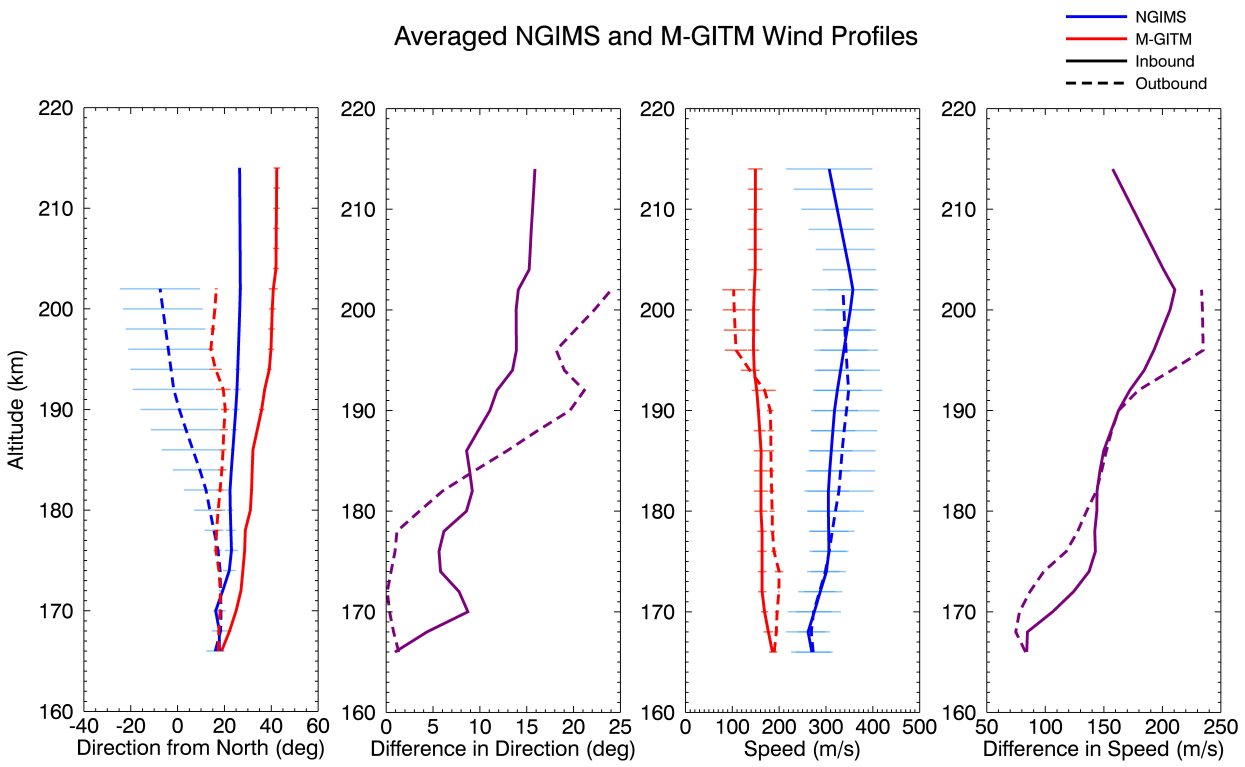

Figure 2.1: Averaged NGIMS (blue) and M-GITM (red) altitude profiles of wind speed and direction for the September 2016 campaign. The purple profiles show the differences in speed and direction between NGIMS and M-GITM campaign averages. The solid lines show the inbound segment of the orbit while the dashed lines indicate the outbound segment. Horizontal lines show one standard deviation of orbit-to-orbit variability over the campaign. Note that direction is plotted in degrees from North (in a clockwise sense).

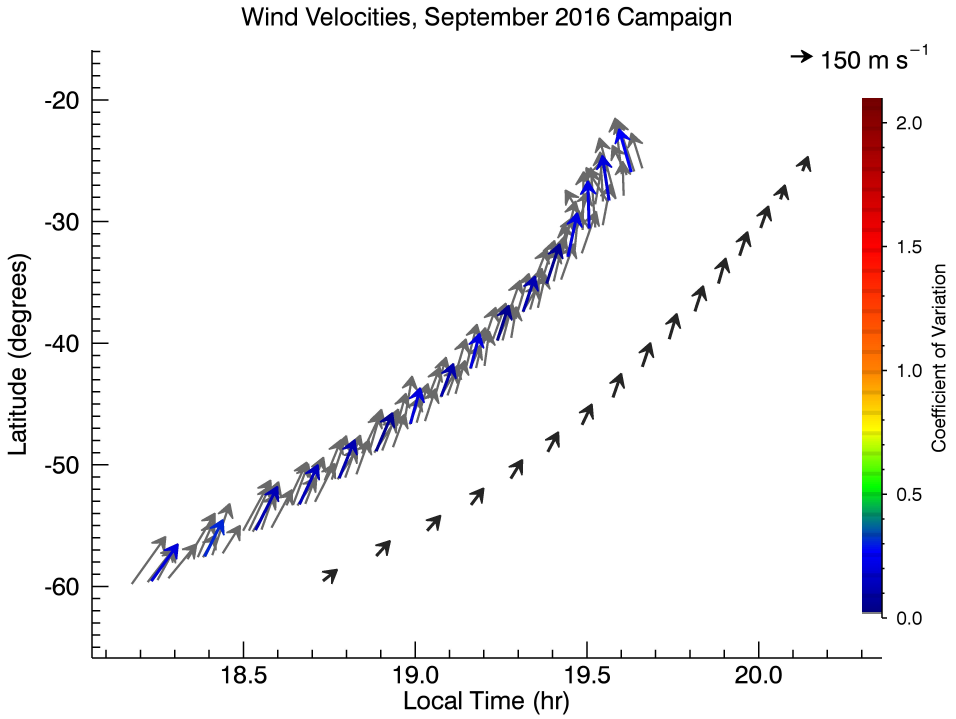

Figure 2.2: Wind vectors from the September 2016 NGIMS observational campaign in latitude and local time. Gray vectors show all observations from each individual orbit of the campaign while the colored vectors represent the campaign averaged velocities. The colors of the campaign averaged vectors represent the calculated coefficient of variation along the track, with higher values indicating more orbit-to-orbit variability. Note that these plots from all campaigns use the same color scale for the coefficient of variation. The black vectors show the averaged M-GITM simulated velocities. The M-GITM vectors have been set to one half hour later in local time than the NGIMS observations for readability on these plots. Individual orbits of M-GITM flythroughs are not shown since the vectors stack on top of each other due to minimal orbit-to-orbit variability simulated by the model.

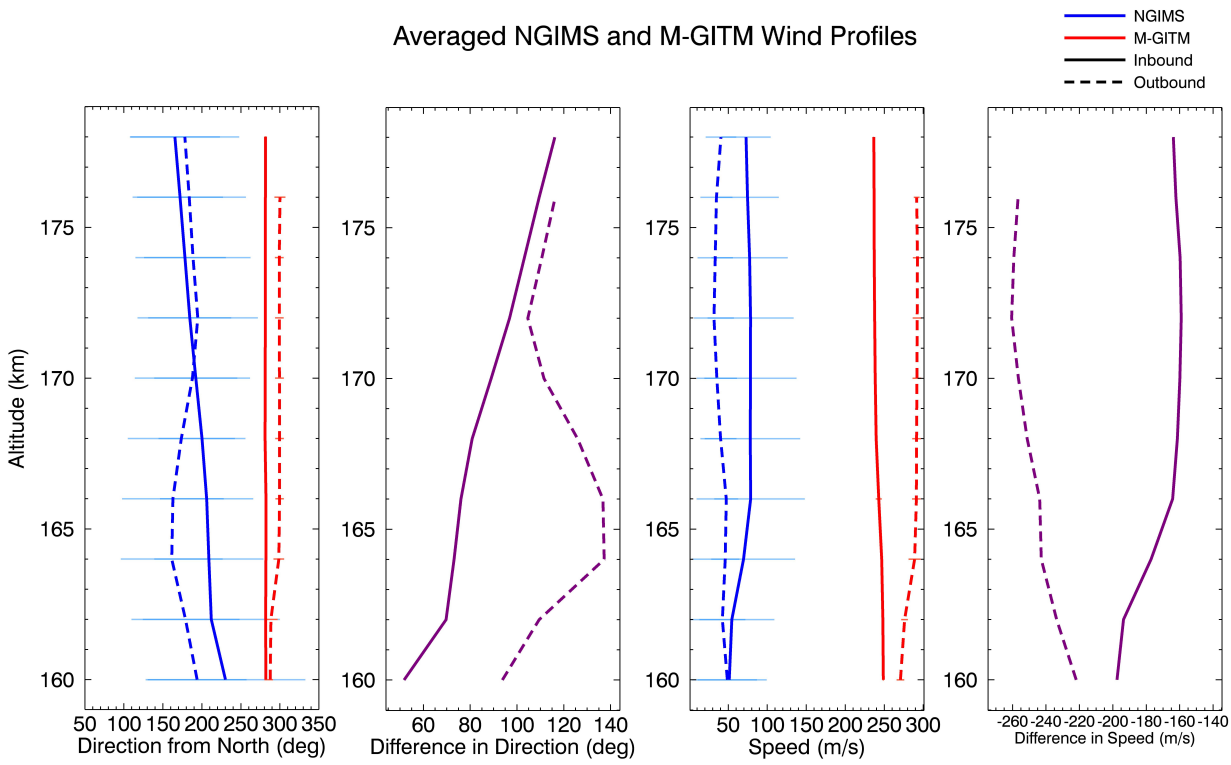

Figure 2.3: Averaged altitude profiles of wind speed and direction from the January 2017 campaign and corresponding model flythrough, with 1-σ orbit-to-orbit variability. Plots are in the same format as those in Figure 2.1.

between each sampling point (represented in Figure 2.4 by individual gray vectors). Both overall lower speeds and an average of vectors with very different directions contributes to the low average speeds. The lack of any persistent wind direction also perhaps implies the average direction is less meaningful in this campaign. This high orbit-to-orbit variability is not only extremely different than the consistency observed in the September 2016 campaign, but is also an extreme case among all of the NGIMS wind campaigns.

2.5.3 May 2017 Campaign

The May 2017 campaign occurred shortly after northern hemisphere spring equinox in the northern mid-latitudes. These ten consecutive orbits sampled the dayside, right before local noon. On average, over the campaign and all altitudes, this campaign observed wind speeds $\sim$120 m/s and directions toward the E to SSE, as seen in Table 2.2 and Figure 2.4 respectively. In this campaign, wind speeds increase away from spacecraft periapsis on the outbound leg (at higher altitudes, lower latitudes, and closer to noon local time). The wind direction also shifts from eastward to

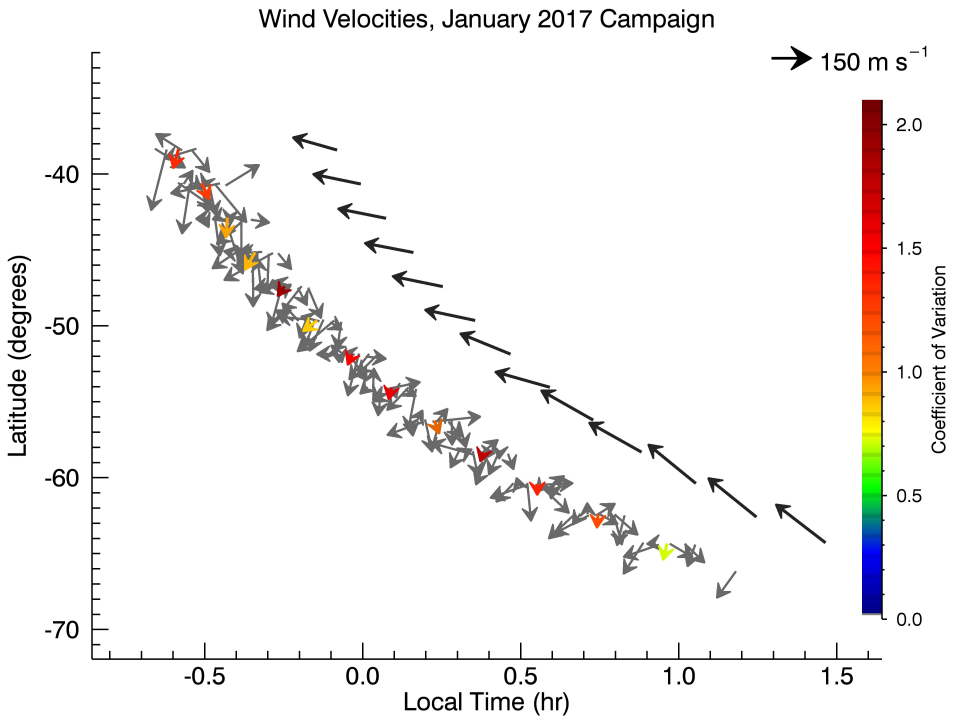

Figure 2.4: Averaged (colored) and individual (gray) wind velocity vectors from the January 2017 campaign. Black vectors show averaged simulated wind velocities from M-GITM, shifted from the NGIMS observations by half an hour in local time. The plot is in the same format as that in Figure 2.2.

southeastward along the track. Though separating the effects of altitude, latitude, and time is difficult due to the nature of the spacecraft's track, based on the altitude profiles in Figure 2.3, this shift in heading does not seem to be as much a function of altitude, but rather one of latitude or local time.

Looking at the coefficient of variation values in Figure 2.4, this campaign had less orbit-to-orbit variability than the January 2017 campaign, but more than the September 2016 campaign. Coefficient of variation values are greatest (approaching 1.3) near periapsis. The lower average wind speeds at periapsis altitudes are a result of both overall lower speeds in this section of the orbit as well as increased directional variability, somewhat similar to what was seen throughout the January 2017 campaign.

Significantly in this campaign, and clearly seen by the profiles showing direction in Figure 2.3, NGIMS observed wind directions and M-GITM simulated flythrough directions are nearly 180° apart throughout much of the sampled track. This difference in direction between simulations and observations is smallest in the inbound leg of the orbit (higher latitudes and earlier local times) where averaged NGIMS winds have a greater zonal component, traveling nearly to the east. Unlike the direction, the difference in simulated and observed speeds is relatively small, only ∼40 m/s on average, and in particular, for the outbound leg of the orbit, reaches 0 m/s difference.

2.5.4 December 2017 Campaign

The December 2017 campaign occurred during the aphelion season over the southern hemisphere, low-latitude, late-morning dayside. During this campaign, the averaged magnitude of the winds reached 200 m/s while the direction was primarily to the WNW. As seen in Figure 2.8, very little turning of the averaged observed winds occurs except at lower latitudes and later local times, where a slightly stronger northward component is introduced. Additionally, the averaged speeds for this campaign are faster near periapsis.

Relatively small orbit-to-orbit variability is seen in this campaign, as implied by the lower values of the coefficient of variation in Figure 2.8 (0.28 on average). Only a couple of the orbits out of the five in the campaign provided most of that variation, while the remaining orbits were largely consistent with each other.

In this campaign, comparing with the corresponding M-GITM flythrough, the direction of the simulated winds is less than 90° apart (Figure 2.7). Both M-GITM and NGIMS show winds primarily directed westward, though the observed winds have a minor northward component, while the simulated winds instead have a southward component in their heading. In addition, averaged over the campaign and profile at 157 m/s, M-GITM predicts slower speeds than observed with NGIMS by ∼45 m/s.

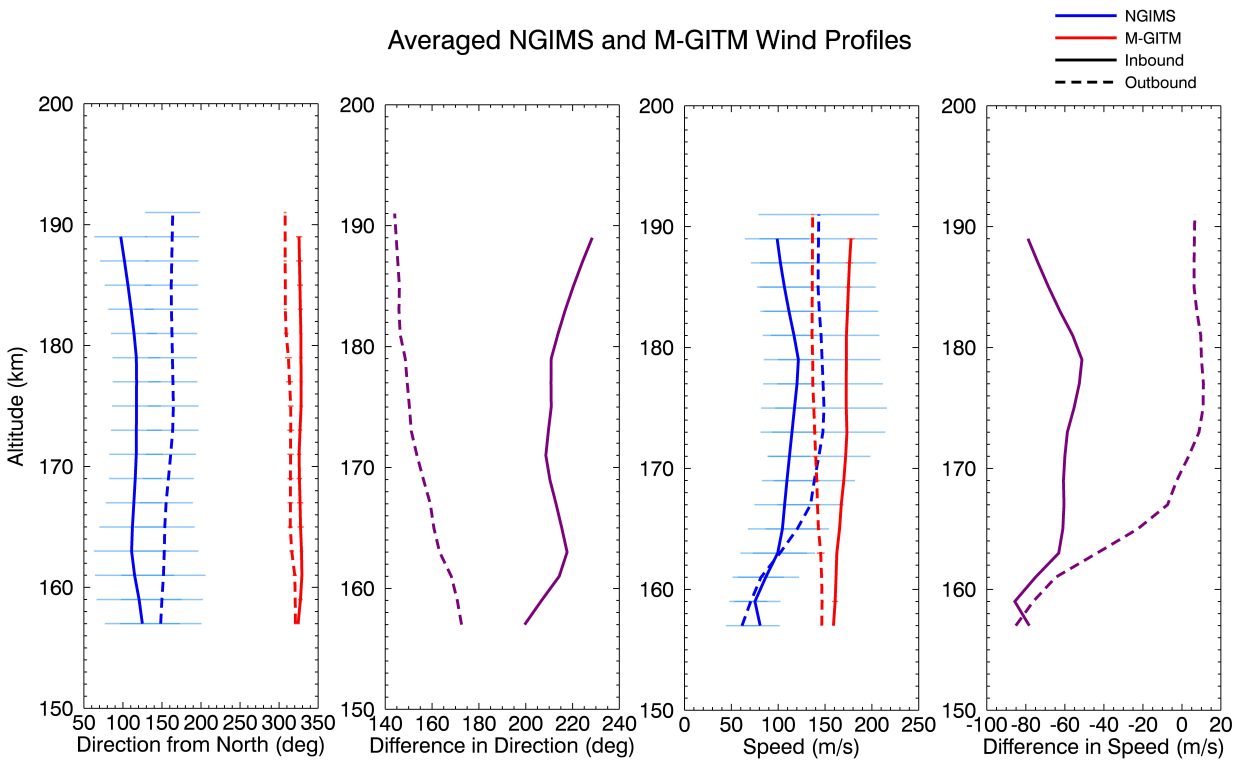

Figure 2.5: Averaged altitude profiles of wind speed and direction from the May 2017 campaign and corresponding model flythrough, with 1-σ orbit-to-orbit variability. Plots are in the same format as those in Figure 2.1.

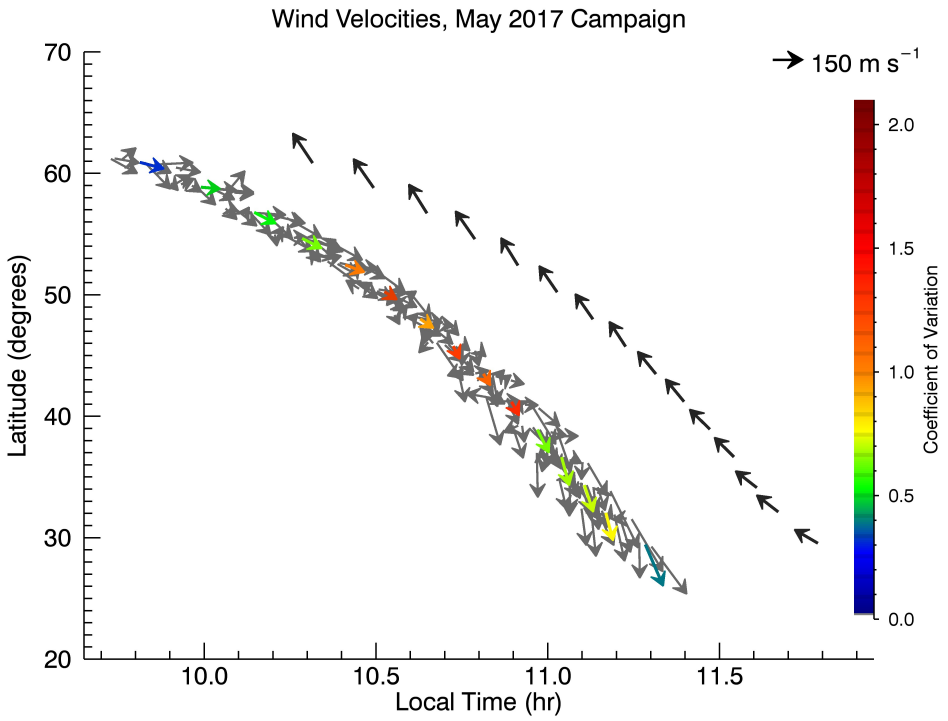

Figure 2.6: Averaged (colored) and individual (gray) wind velocity vectors from the May 2017 campaign. Black vectors show averaged simulated wind velocities from M-GITM, shifted from the NGIMS observations by half an hour in local time. The plot is in the same format as that in Figure 2.2.

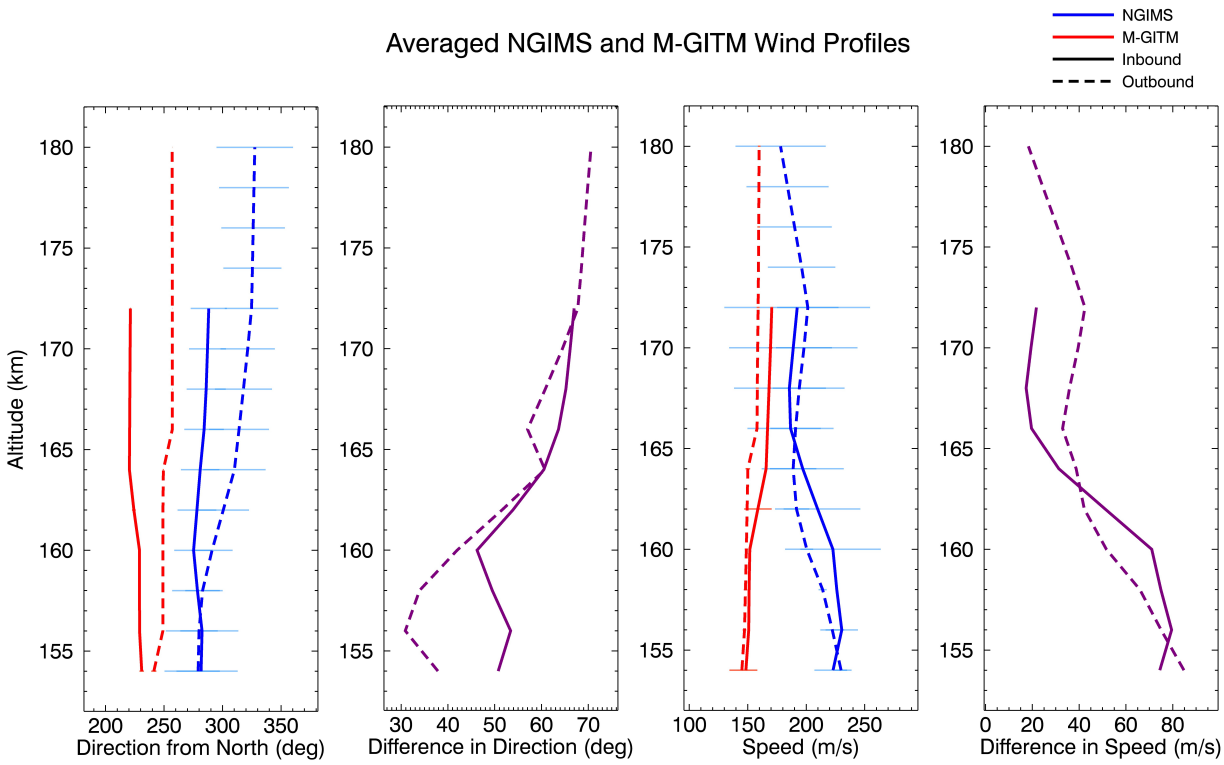

Figure 2.7: Averaged altitude profiles of wind speed and direction from the December 2017 campaign and corresponding model flythrough, with 1-σ orbit-to-orbit variability. Plots are in the same format as those in Figure 2.1.

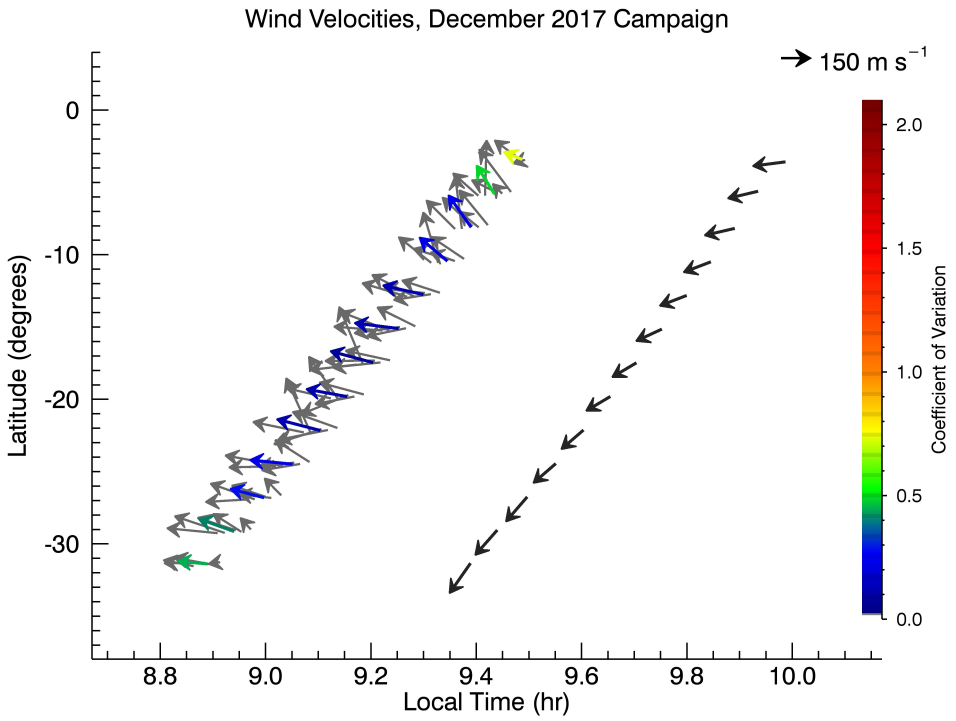

Figure 2.8: Averaged (colored) and individual (gray) wind velocity vectors from the December 2017 campaign. Black vectors show averaged simulated wind velocities from M-GITM, shifted from the NGIMS observations by half an hour in local time. The plot is in the same format as that in Figure 2.2.

2.5.5 February 2018 Campaign

Similar to the January 2017 campaign, the February 2018 campaign consisted of ten consecutive orbits taking observations near local midnight at southern mid-latitudes. The February 2018 campaign, however, occurred late in the aphelion season. In this campaign, averaged winds were slightly faster than the December 2017 campaign, at 221 m/s. As seen in Figure 2.10, the averaged winds in the February 2018 campaign do shift (from a NNE to a NNW heading) as the sampling progresses to lower latitudes and later local times.

There was a moderate amount of orbit-to-orbit variability observed in this campaign (as seen in Figure 2.10), though more strongly present in magnitude than direction. However, this case still had more orbit-to-orbit consistency in the flow than the January 2017 campaign, as seen by an average coefficient of variation of 0.52.

Notably, the difference in direction between observed and simulated winds in this campaign is relatively small, on average about 35° (see Figure 2.9). Both observed and simulated averaged speeds show a strong northward component. Headings match most closely at the lower latitudes and later local times of the outbound leg of the orbit, where both simulated and observed speeds are directed NW. Unlike the averaged direction, M-GITM does not well replicate the average speed. With a flythrough average of $\sim$130 m/s, M-GITM underpredicts speed by nearly 100 m/s.

2.6 Discussion

2.6.1 Analysis of Selected NGIMS Wind Campaigns and M-GITM Comparisons

These NGIMS campaigns include a range of cases from those in which M-GITM can, to a large extent, replicate observed wind velocities to those in which M-GITM is not capturing observed winds at all. In Section 2.5, it was seen that for the September 2016 campaign, M-GITM very closely replicated direction (which on average differed by 25° at most), but was underpredicting average speed by $\sim$150 m/s. Similarly, in the February 2018 campaign, simulated and observed directions are reasonably close, while M-GITM suggests an average speed almost 100 m/s less than what was observed. The May 2017 campaign, on the other hand, shows M-GITM producing averaged speeds only $\sim$40 m/s different from those observed by NGIMS. The averaged direction in this case, however, was roughly 180° opposing. The December 2017 campaign showed a general agreement in the direction of the main component of the velocities, and had a $\sim$45 m/s difference in averaged speed. The most disparate of these cases was the January 2017 campaign, in which M-GITM overpredicted speeds by more than 200 m/s on average and did not match the average

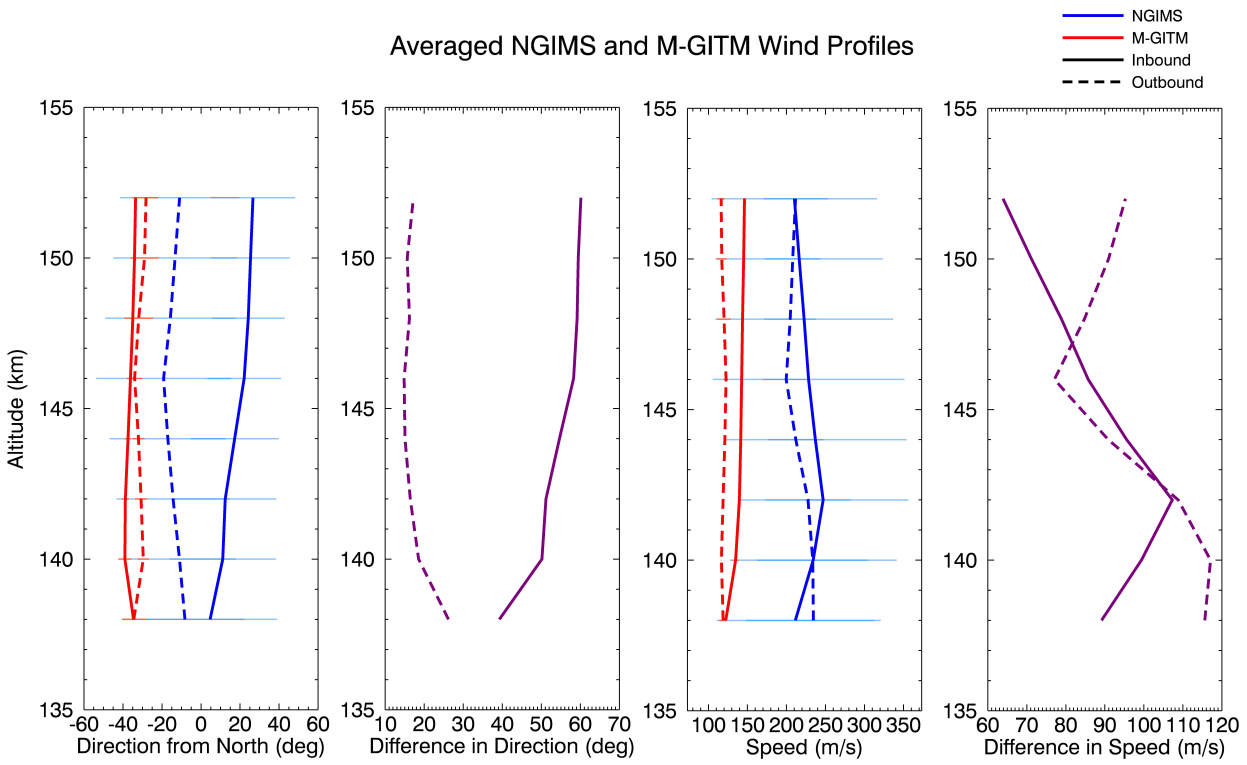

Figure 2.9: Averaged altitude profiles of wind speed and direction from the February 2018 campaign and corresponding model flythrough, with 1-σ orbit-to-orbit variability. Plots are in the same format as those in Figure 2.1.

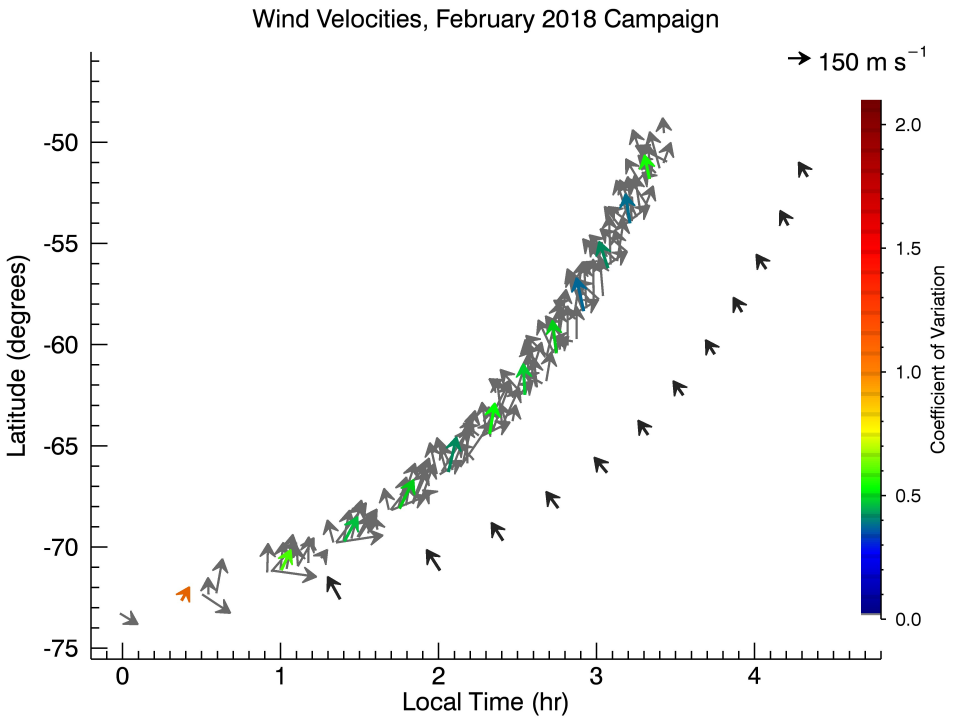

Figure 2.10: Averaged (colored) and individual (gray) wind velocity vectors from the February 2018 campaign. Black vectors show averaged simulated wind velocities from M-GITM, shifted from the NGIMS observations by an hour in local time. The plot is in the same format as that in Figure 2.2.

direction either. Thus, there are cases where observed and simulated speeds are similar but directions are not, those where direction is similar, but speed is not, and one where neither is replicated by the model.

Significantly, the M-GITM model is currently primarily driven by solar forcing at thermospheric altitudes [*Bougher et al.*, 2015c; *Bougher et al.*, 2017b]. No other processes included in the model have as large of an impact in driving thermospheric behavior as EUV heating. Inclusion of physics in M-GITM that accurately represent the effects of typical in-situ solar forcing at these altitudes (see Section 2.4.2) was particularly emphasized in developing the model due to the importance of EUV heating in the thermosphere (see Section 2.3). (Note that by typical or normal solar forcing, we mean the impact of background solar conditions on the atmosphere without any possible effects from large transient phenomena such as solar flares.) Due to the emphasized capabilities of the model in regard to normal solar forcing, this implies that a likely interpretation for cases of data-model agreement is that differential heating resulting from absorption of EUV radiation is the process most strongly responsible for driving the observed thermospheric winds.

Figures 2.11, 2.12, and 2.13 show temperatures and horizontal winds at a constant altitude (170 km) over latitude and local time from M-GITM simulations corresponding to September 2016, May 2017, and December 2017. These cases in turn correspond to near perihelion, near equinox, and near aphelion conditions, respectively. The effects of solar forcing in M-GITM can be seen as, in general across all seasons, the model suggests a horizontal circulation in which the winds flow away from the subsolar point and converge on the nightside. The first analysis of all available NGIMS wind campaigns presented by *Benna et al.* [2019] also described a general dayside to nightside flow that was observed in many of the campaigns.

In the September 2016 campaign, the significant directional agreement between simulated and observed winds suggests that during this time period, differential solar heating is likely the primary mechanism driving the thermospheric winds. Recall that this campaign occurred near the evening terminator on the dayside near perihelion. During the perihelion season, solar forcing in the thermosphere would be expected to be stronger due to the increase in solar flux received when Mars is closer to the Sun, resulting in a warmer summer and a more intense diurnal cycle [*González-Galindo et al.*, 2009]. In Figure 2.11, M-GITM produces a fairly high-speed circulation in the mid-southern latitudes near the evening terminator where the September 2016 campaign took place. This flow pattern produced by M-GITM is likely representative of actual conditions near the time and in the general vicinity of this MAVEN campaign as indicated by the substantial agreement of the model flythrough with the observed direction.

Likewise, the agreement in average direction for the February 2018 campaign implies this is probably another case where normal solar forcing is strongly driving the winds at this time and location. Looking at Figure 2.13 (though it is from the December 2017 simulation, it occurs in

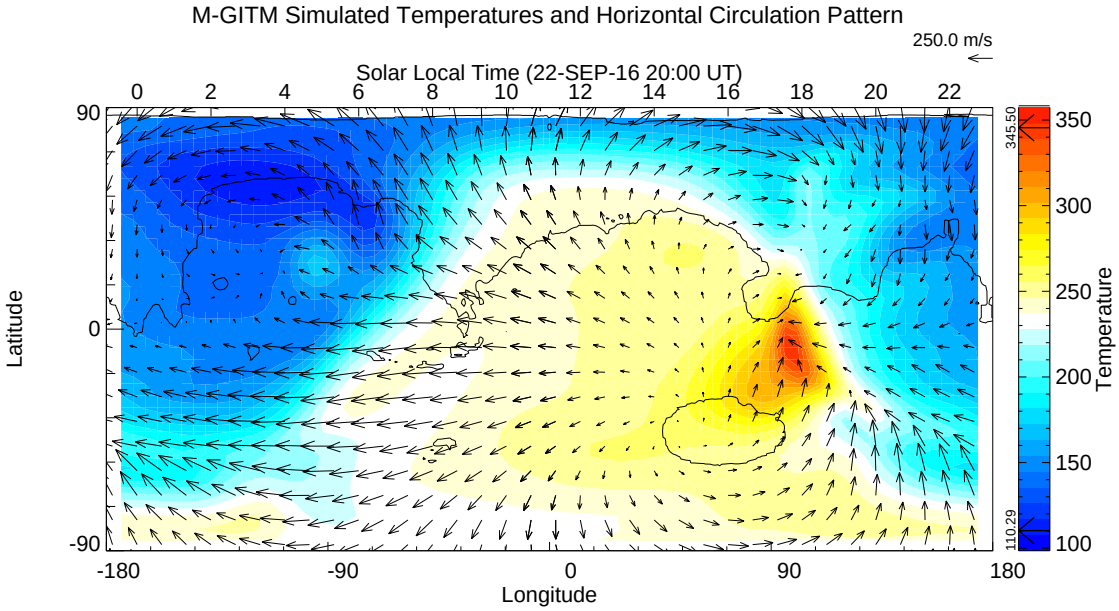

Figure 2.11: M-GITM simulation of September 22, 2016, showing temperatures (K) and wind velocity vectors at 170 km.

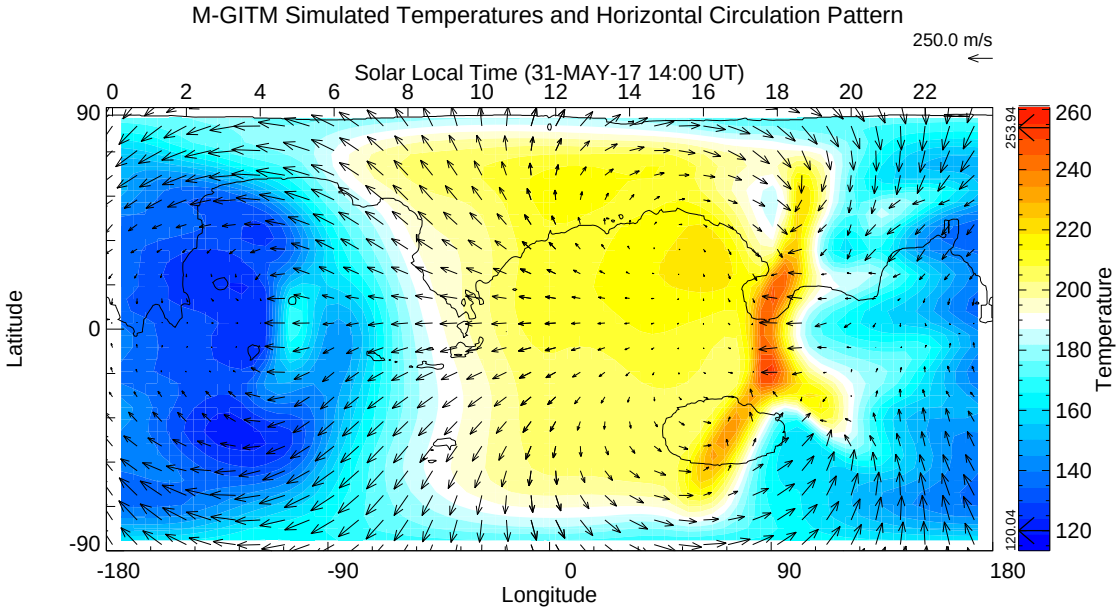

Figure 2.12: M-GITM simulation of May 31, 2017, showing temperatures (K) and wind velocity vectors at 170 km.

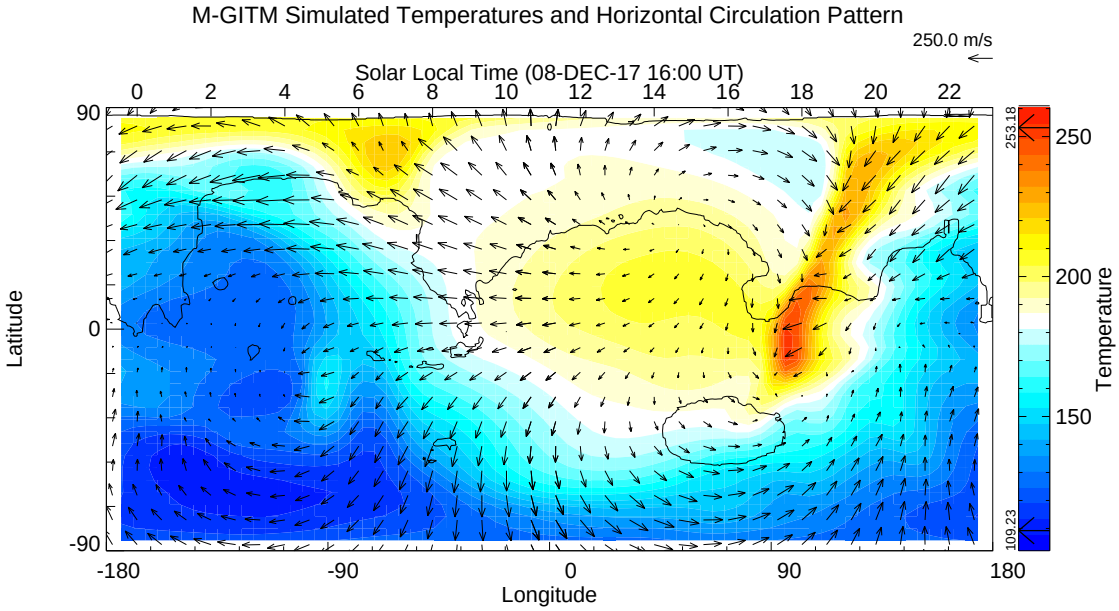

Figure 2.13: M-GITM simulation of December 8, 2017, showing temperatures (K) and wind velocity vectors at 170 km.

the same season as the February 2018 campaign and thus, the plot is not discernably different), M-GITM suggests that at these high-southern latitudes on the nightside, there is a strong northward flow coming over the south pole from the dayside. Again, the strong directional agreement between simulations and observations suggests the winds at this time and location are following the circulation pattern produced by M-GITM, established by differential heating. Solar forcing appears to be largely driving the winds for this campaign even during the aphelion season, when Mars is at a greater distance to the Sun. Even in the December campaign, winds seem to generally follow the expected circulation pattern in that location, so similar to the winds simulated by M-GITM, are likely driven primarily by normal solar forcing (Figure 2.13).

Yet even these three cases where data-model agreement in wind direction seems to indicate the importance of the role of solar forcing, the model is not replicating the magnitude of the winds. This suggests that while solar forcing might play the most important role during these campaigns, other processes are still modifying the winds, and particularly in these campaigns, their speeds.

It should be noted that temperatures in the Martian upper atmosphere are believed to vary with the solar cycle [e.g. *Forbes et al.*, 2008; *Bougher et al.*, 2017a] and modeling studies have suggested the solar cycle should impact thermospheric winds as well [e.g. *Bougher et al.*, 2009, 2015c]. However, all five of these campaigns occurred during near solar minimum conditions. Thus, the change in solar flux and any corresponding heating due to the eleven-year solar cycle is not likely driving the thermospheric winds in these cases.

In contrast to the above three cases, the January and May 2017 campaigns show significant directional disagreement when compared to the M-GITM simulated winds. The disparity observed in the data-model comparisons for these campaigns suggests that not only is normal solar forcing not the primary mechanism acting on the winds, but the processes modifying them are those that M-GITM is lacking or handles poorly.

The January 2017 campaign stands out as the worst match to its corresponding M-GITM flythrough in both wind direction and speed. From Figure 2.11 (using the September 2016 perihelion plot as a close proxy), M-GITM predicts a very high-speed flow in this vicinity due to a circulation from the subsolar region across the south pole to the nightside. This does not at all represent the velocities observed by NGIMS. With NGIMS campaign average speeds of near 35 – 80 m/s at 170 km (and on average 56 m/s throughout the profile), some mechanism is significantly slowing down and modifying the wind direction from the flow expected from the predominately solar-driven M-GITM simulations. This mechanism could be related to the extreme variability in the winds during this campaign. Implications of this variability and data-model comparisons will be discussed further in Section 2.6.3.

As mentioned in Section 2.4.1, during the wind measurement retrieval process, any modulation during the 30 seconds it takes for the APP to nod once is compared to the expected modulation if

constant winds are assumed. This comparison provides a measure of variability of the wind on a scale of a few seconds. During the January 2017 campaign, while the winds exhibited very large variability on the scale of hours (perceptible in the orbit-to-orbit comparison), they did not show appreciable variability on the scale of seconds. This increases confidence in the quality of these observations while additionally providing a time scale restraint for identifying processes that could be producing this variability.

In the May 2017 campaign, wind headings are observed that are on average $\sim$180° apart from the winds expected in M-GITM. While some variability is present in this campaign, it is not present to the extent observed in the January 2017 campaign. Most, though not all, orbits show a prevailing direction to the E to SE. Examining Figure 2.12, it can be seen that M-GITM, in this location (mid-northern latitudes on the dayside prior to local noon), produces a meridional flow that is directed northward as a part of a transpolar flow from the subsolar point to the nightside and a zonal flow that is westward, again from subsolar point to nightside. The reverse direction in the flow seen in the NGIMS observations with only a moderate amount of orbit-to-orbit variability suggests there is a completely different circulation pattern set up at the specific time and location of this campaign. It is possible another physical process not included in the model is dominating and reversing the expected flow driven by normal solar forcing and predicted by M-GITM.

2.6.2 Local Time and Seasonal Effects

A few campaigns occur at similar local times, latitudes, or seasons. This overlap makes it possible to try to examine the influences of different geophysical conditions. For example, both the January 2017 and the September 2016 campaigns occurred near perihelion so had very similar solar declination angles and also tracked over near the same mid-southern latitudes. However, while the September 2016 campaign was on the dayside near the evening terminator, the January 2017 campaign occurred at local midnight.

Since the January 2017 campaign differs from the September 2016 campaign in local time, but is similar in other geophysical conditions, it might seem that the physical processes the model isn't representing well in the January 2017 campaign are dependent on local time and act more strongly on the nightside of Mars where that campaign occurs. A similar phenomenon with nightside M-GITM simulations has been noted in a study by *Zurek et al.* [2017]. In this study, densities derived from the accelerometer on MAVEN closely matched simulated densities on the dayside but did not well replicate the accelerometer calculations on the nightside (especially the midnight to dawn sector where the orbit-to-orbit variability was significant). This might suggest M-GITM is missing fundamental physics on the nightside of the planet which play a large role in altering the upper atmospheric flow.

The February 2018 campaign might also be compared to the January 2017 campaign since both occurred at mid-southern latitudes at or slightly after local midnight. The February 2018 campaign occurred near aphelion while the January 2017 campaign occurred near perihelion. It is possible that some of the observed differences in the flow patterns of these two campaigns are due in part to seasonal effects. However, like the September/January comparison above, the February 2018 campaign rather closely matches the expected direction from M-GITM while the January 2017 campaign is again very different. This brings into question whether a local time or seasonal dependency is primarily creating the differences seen in the September/January cases, or if this is just showing the unique nature of the January 2017 campaign. Thus, no clear seasonal or local time trend can be determined with just these few campaigns.

2.6.3 Variability

As discussed in Section 2.5.2, extremely high orbit-to-orbit variability was observed in the January 2017 campaign. Since no preferential direction is observed but only variability on very short time scales, it is not particularly surprising that M-GITM is producing such a different direction than seen with NGIMS. M-GITM would not be expected to replicate extremely short timescale variability since within the physics included in the model, the shortest time scale fluctuations come from the FISM-M fluxes, but even these are interpolated daily averages. The physical process (or processes) acting on the winds in this campaign to create this level of variability on short time scales is not one included in M-GITM.

The lack of significant orbit-to-orbit variability generated in M-GITM simulations can be seen in the average standard deviations of speed and direction for the M-GITM flythroughs in Tables 2.2 and 2.3. For these campaigns, a 1-σ around 3–4° for direction and 2–3 m/s for speed is typical for M-GITM. These standard deviations are several factors smaller than the 1-σ values calculated for speed and direction for the NGIMS wind observations. One exception is the higher standard deviation of speed seen in the September 2016 M-GITM flythrough, at 12 m/s averaged over the profile. This larger standard deviation is due to the small changes in local time of the spacecraft's track each orbit combined with the proximity of the campaign to the evening terminator, which is one region where the model does generate more variability due to changes in flow surrounding a zone of converging winds.

Campaign averaged NGIMS velocity profiles were computed in this study in order to make the in-situ NGIMS wind observations more comparable to what is essentially a climate model (with the notable exception of the use of FISM-M daily fluxes). Through this averaging of at least five consecutive orbits, some of the high-frequency variability due to changing weather and potential variability due to longitudinal effects should be averaged out. However, in some cases,

particularly the January 2017 NGIMS campaign, the variability is persistent, even over a period of 10 orbits (two to three Earth days). This suggests that over several orbits, localized processes or those occurring on shorter time scales can dominate the expected solar forcing driven circulation pattern. Particularly in the January 2017 case, it also seems that potential trends due to seasonal, local time, and latitude effects are being overwhelmed by another sort of forcing that is specifically occurring during this campaign. Since this extreme variability is not seen in any of the other selected campaigns, it could be that these processes driving the neutral thermospheric winds and their variability in the January 2017 campaign are extremely specific to that combination of local time, latitude, season, or other geophysical parameters.

In general, it is found that there is a relationship between variability and how well the NGIMS wind observations agree with M-GITM simulated winds. Looking at Table 2.4, the NGIMS campaigns with the highest average coefficient of variation, January 2017 and May 2017, are those where M-GITM is not capturing any part of the averaged observed direction, and for the January 2017 case, this is also true for the average speeds. The two campaigns with the smallest average coefficient of variation, September 2016 and December 2017, have an extremely close match in direction, and a general agreement in the heading of the main component, respectively, compared to the corresponding model simulations. Again, this miss-match between simulations and observations in these cases with high variability is to some extent expected as M-GITM lacks many of the high-frequency time dependent processes that might allow it to simulate this level of change over shorter time scales and only has spatial scales allowed by its resolution. However, it also implies that normal solar forcing may have a less dominant role in driving the thermospheric winds when this level of variability is observed. Instead, other processes may have gained relevance and altered the expected flow, perhaps by introducing turbulent components.

2.6.4 Averaged Speed and Data-Model Comparison

Finally, one trend that does seem to stand out in determining the degree of similarity between thermospheric wind headings in M-GITM simulations and observations might be the averaged speed (averaged over the campaign and all altitudes). The faster the averaged speed observed by NGIMS over the campaign, the less difference between simulated and observed wind headings is seen. The September 2016 campaign has the highest averaged wind speeds of this set of campaigns, and also on average, the least difference in heading between simulated and observed winds. The January 2017 campaign, which has high orbit-to-orbit variability, also has on average very low speeds. The next slowest average campaign was the May 2017 case, in which there was a near 180° difference between NGIMS observed winds and M-GITM flythroughs. Of the five campaigns here, it is only those where the average speed is at least 200 m/s where the difference in direction

is less than 90°.

This could again indicate the relative importance of the role of solar forcing in those campaigns. When the thermospheric winds are more strongly and steadily controlled by differential solar heating in the thermosphere compared to other forcing mechanisms, they might be more likely to follow the same circulation pattern suggested by the primarily solar driven M-GITM and experience less orbit-to-orbit variability.

However, the averaged NGIMS speed is not as strong of a predictor for similarity in wind magnitude as it is for heading. For instance, the September 2017 campaign has the fastest averaged speed observed by NGIMS, but M-GITM suggests winds over 150 m/s slower, while the January 2017 campaign has the slowest averaged speed and M-GITM overpredicts speeds by over 200 m/s.

2.6.5 Physical Processes Not Represented in M-GITM

In their comparisons of densities derived from the MAVEN accelerometer and those predicted by M-GITM, *Zurek et al.* [2017] mentioned that where M-GITM could not well replicate observed densities, one physical process that might be acting relatively more strongly was gravity waves. Although the effects of gravity waves are not currently included in M-GITM, internal gravity waves are expected to be ubiquitous in the atmospheres of stably stratified planets, including Mars [*Yiğit et al.*, 2015]. Several observational studies have identified the effects of gravity waves in the Martian thermosphere. Measurements from MGS and Mars Odyssey aerobraking around 100-150 km showed highly variable gravity wave amplitudes, with density perturbations up to 50% of the background [*Fritts et al.*, 2006]. More recent studies from *Yiğit et al.* [2015] and *England et al.* [2017] using observations from the NGIMS instrument on MAVEN have also observed and begun to characterize the thermospheric gravity waves up to $\sim$220 km.

In addition, modeling studies such as *Medvedev and Yiğit* [2012] have shown that gravity waves should have significant dynamical and thermal effects in the lower thermosphere through large gravity wave momentum deposition. Some GCM simulations have suggested the gravity wave drag in the thermosphere is so large that it would be expected to modify the wind distribution dramatically [*Medvedev et al.*, 2011a, b]. Gravity waves could also have an appreciable thermal effect in the thermosphere, both from heating of the flow due to conversion of mechanical energy to heat and from heating/cooling due to divergence of the sensible heat flux [*Medvedev and Yiğit*, 2012].

Thus, if the effects of gravity waves were included in the M-GITM model, the simulated thermospheric temperature structure would be expected to change, accompanied by modifications of the circulation pattern. This could possibly help the model to better replicate the NGIMS wind observations in some campaigns, particularly those in which it has been found that typical solar

forcing is likely not the only process responsible for significantly driving thermospheric winds. However, it is likely that gravity waves are not the only physical process that M-GITM is missing or not well representing which could be modifying the winds during these campaigns.

It is also possible that some of the orbit-to-orbit or shorter time scale variability seen in some of the campaigns is a result of the effects of gravity waves. However, adding a gravity wave parameterization scheme to M-GITM will not add variability in the simulations from individual waves since these schemes are statistical averages of gravity wave effects that impact the background winds. Models such as that used in *Kuroda et al.* [2015] can resolve gravity waves and so might be able to be used to determine if this orbit-to-orbit variability is from the effects of gravity waves being triggered at different seasons or locations.

Though M-GITM does account for dust in the Martian atmosphere in these simulations, it does so with a relatively simple scheme that assumes a time averaged and horizontally uniform dust load (see Section 2.4.2). This would mean M-GITM is likely underpredicting the influence of dust during the dust storm season (centered around perihelion), during which regional dust storms can notably increase the dust optical depths observed in the atmosphere [e.g. *Smith*, 2009]. Other studies have found that dust lofted into the atmosphere by large regional dust storms significantly impacts the radiative transfer in the atmosphere, in turn affecting heating (and thus likely the atmospheric circulation) in the lower-middle atmosphere, even far away from the center of the storm [e.g. *Heavens et al.*, 2011b; *Kass et al.*, 2016]. Since the upper atmosphere is coupled to the lower atmosphere [e.g. *Bougher et al.*, 2017a], these large dust storms could also have an impact on upper atmospheric circulation, especially through the alteration of wave propagation.

Two NGIMS wind campaigns examined here which occur in the perihelion dust storm season are the September 2016 and January 2017 cases. Of these two, the effects of increased dust would be most important during the September 2016 campaign, which occurred during the decay of a larger regional dust storm (see Mars Year 33 at http://www-mars.lmd.jussieu.fr/mars/dust_climatology/index.html on the Mars Climate Database). While the September 2016 campaign had a very close match in simulated and observed wind direction, the magnitude of the winds was significantly different. It is possible that the increased dust during this time period is modifying the winds beyond what M-GITM suggests for a yearly-averaged dust load. Incorporating a time dependent dust parameterization scheme based on the dust load observed during each specific campaign would better reflect reality and might improve model simulations.

In addition to influences from the lower atmosphere, such as gravity waves and dust storms, large solar or ionospheric events could also impact the neutral thermospheric winds. These solar events (which we differentiate from normal solar forcing) could include coronal mass ejections and flares, which impact the ionosphere and the neutral thermosphere [e.g. *Fang et al.*, 2013;

Elrod et al., 2018; *Jain et al.*, 2018]. However, no major solar events were seen during the time periods around any of these campaigns (see the MAVEN science event list on the Planetary Data System, files maven_events_2013-12-01-00-00-00_2016-11-15-00-00-00 and maven_events_2016-11-15-00-00-00_2017-02-15-00-00-00).

2.7 Conclusions

Thermospheric winds at Mars are examined through comparisons of NGIMS neutral wind observational campaigns and corresponding upgraded M-GITM simulations. M-GITM simulations were produced for five NGIMS wind campaigns which occurred over several different latitudes, local times, and seasons. Model flythroughs were extracted along the same trajectory flown by MAVEN during each orbit, and the averaged NGIMS and M-GITM altitude profiles of speed and direction were compared.

Simulations for the September 2016 and February 2018 campaigns provide the best overall agreement with the velocities observed by NGIMS, though they much more closely match the observed direction than speed, which M-GITM underpredicts by about 100 to 150 m/s. The December 2017 campaign measurements match the corresponding simulation moderately well in both speed and direction. On the other hand, the January 2017 and May 2017 campaigns have large disparities between the observed and simulated wind velocities. For the May campaign, M-GITM produced wind directions that were nearly 180° from those observed, suggesting that an entirely different circulation pattern may have formed in this vicinity than the one expected by M-GITM. The poor correspondence between data observations and model simulations in the January 2017 campaign seems to stem from the presence of extremely high orbit-to-orbit variability (as well as variability from sampling point to sampling point within an orbit). In this case, M-GITM predicts speeds over 200 m/s faster than those actually observed.

Since M-GITM is primarily driven by solar forcing at thermospheric altitudes in the form of EUV heating, these data-model comparisons can be used to help interpret the extent of the role of solar EUV heating in driving thermospheric winds during different campaigns. As a result, a likely interpretation of data-model agreement is that solar forcing in the form of differential heating from absorption of EUV radiation at these altitudes is primarily driving thermospheric winds at these times. Data-model disagreements suggest that processes which are not well represented or completely absent from the model may gain relevance and alter the expected circulation patterns, perhaps by introducing variability in the flow.

Notably, the one parameter over these five campaigns which served as a good indicator of how well the model would replicate that particular campaign was the campaign and profile averaged observed speed. The campaigns with greater averaged observed speeds also had the least averaged

difference in heading between observed and simulated winds. NGIMS campaigns with higher averaged wind speeds also tended to have less orbit-to-orbit variability, as seen by smaller values of the coefficient of variation. In these cases, normal solar forcing may be driving the winds steadily and strongly enough to overcome other processes that may induce more variability in the wind.

Though some of these campaigns covered similar latitudes, seasons, and local times, no clear trends across these were identified. This is likely partially due to the small sample size of campaigns analyzed here. Trends could also be obscured by the unique nature of the extreme orbit-to-orbit variability in the January 2017 campaign. It is possible the processes acting in January 2017 to create this extreme variability are masking any response to normal solar forcing or trends that might be observed across season or local time. Looking at all available NGIMS campaigns that occurred in the perihelion season, near midnight local time, or at middle to high latitudes might help reveal if the behavior in the winds seen in the January 2017 campaign is related to a specific combination of geophysical conditions, or if it is due to something else entirely. In addition, a more comprehensive look at all available NGIMS wind observations in comparison to model simulations might highlight specific regions where the model routinely agrees or disagrees with the measurements, which could help identify important physical processes acting in those regions.

These data-model comparisons serve as one of the first analyses of this dataset and demonstrate both the potential benefits and challenges of comparing the new NGIMS wind observations to model simulations. These comparisons will also serve as a baseline for future analysis as new or improved physics is added to M-GITM. Gravity waves are one type of physical process not currently included in M-GITM; however, they are believed to play a significant role in the Martian thermosphere, with both large dynamical and thermal impacts [e.g. *Yiğit et al.*, 2015; *Medvedev and Yiğit*, 2012]. Thus, incorporating a gravity wave parameterization scheme into M-GITM may adjust both the magnitude and the headings of the simulated winds, similarly to what was seen in *Medvedev et al.* [2011b] and *Medvedev and Yiğit* [2012]. Examining data-model comparisons after the addition of a gravity wave scheme could help constrain the conditions or locations in which gravity waves gain relevance in driving the observed winds.

Comparisons between the NGIMS neutral wind dataset and a revised M-GITM model with new physics should aid in identifying the physical processes which play a significant role in driving thermospheric wind speeds and directions during these campaigns. Additional data-model comparisons and interpretation using the NGIMS wind observations and M-GITM or other Mars GCMs will be necessary, and offers a unique opportunity to improve our understanding of the behavior of the thermospheric winds at Mars and the processes responsible for driving them.

2.8 Acknowledgments

Funding support for this research was provided by the MAVEN project, Grant NNH10CC04C (S.W.Bougher). This work was also supported by NASA Headquarters under the NASA Earth and Space Science Fellowship Program - Grant 80NSSC18K1238 (K.J. Roeten). Funding for F. González-Galindo and M. Á. López-Valverde was provided by the Spanish National Research Council under intramural project CSIC 201450E022. NGIMS datasets used in this paper are available on the Planetary Data System (http://pds-atmospheres.nmsu.edu/data_and_services/atmospheres_data/MAVEN/ngims.html) as well as EUV datasets (https://pds-ppi.igpp.ucla.edu/search/view/?f=yes&id=pds://PPI/maven.euv.modelled). Datacubes containing M-GITM simulations used in this paper can be found on the University of Michigan Deep Blue repository at http://doi.org/10.7302/85qt-e980.

CHAPTER 3

Impacts of Gravity Waves in the Martian Thermosphere: The Mars Global Ionosphere-Thermosphere Model Coupled with a Whole Atmosphere Gravity Wave Scheme

The content in this chapter has been submitted for publication under the same title, by K. J. Roeten, S. W. Bougher, E. Yiğit, A. S. Medvedev, M. Benna, and M. K. Elrod. *Roeten et al.* [2022b] is presented here with modified formatting.

3.1 Abstract

Gravity waves are a key mechanism that facilitates coupling between the lower and upper atmosphere of Mars. In order to better understand the mean, large-scale impacts of gravity waves on the thermosphere, a modern whole atmosphere, nonlinear gravity wave parameterization scheme has been incorporated into a three-dimensional ground-to-exosphere Mars general circulation model, the Mars Global Ionosphere-Thermosphere Model (M-GITM). M-GITM simulations utilizing the gravity wave parameterization indicate that significant gravity wave momentum is deposited in the thermosphere, especially within the altitude range of 90-170 km. This impacts the winds in the thermosphere; in particular, M-GITM simulations show a decrease in speed of the wind maximum in the summer hemisphere by over a factor of two. Gravity wave effects also impact the temperatures above 120 km in the model, producing a cooler simulated thermosphere at most latitudes. M-GITM results were also compared to upper atmospheric temperature and wind datasets from the MAVEN (Mars Atmosphere and Volatile Evolution) spacecraft. Some aspects of wind data-model comparisons improved once the gravity wave scheme was added to M-GITM; furthermore, a cooler temperature profile produced by these new M-GITM simulations for the MAVEN Deep Dip 2 observational campaign resulted in a closer data-model comparison, particularly above 180

km. Overall, these modeling results show that gravity waves play an important role for the energy and momentum budget of the Martian thermosphere.

3.2 Plain Language Summary

Atmospheric gravity waves are an important physical process in the upper atmosphere of Mars. To better understand the average effects of gravity waves on the temperatures and winds above 100 km, a modern numerical scheme designed to represent the relevant physics has been added to a 3-D general circulation model, M-GITM (Mars Global Ionosphere-Thermosphere Model), which extends from the surface to about 250 km. Gravity wave effects can modify the mean flow; results from these M-GITM simulations show that in the upper atmosphere, the wind maximum in the summer hemisphere decreases in speed by over a factor of two. Additionally, above 120 km, the model now produces a cooler upper atmosphere, on average. The new M-GITM results were also compared to upper atmospheric temperature and wind datasets from the MAVEN (Mars Atmosphere and Volatile Evolution) spacecraft. Though the response is complex, certain aspects of wind data-model comparisons improved once the gravity wave scheme was added to M-GITM. For a special MAVEN observational campaign, the decrease in simulated dayside temperatures notably improved comparisons to corresponding data. Overall, these results show that gravity waves have a significant impact on the upper atmosphere of Mars.

3.3 Introduction

Atmospheric gravity (or buoyancy) waves (GWs) are present in all stably stratified planetary atmospheres at all altitudes during all seasons with varying degree of intensity [*Ando et al.*, 2015; *Forbes et al.*, 2016; *Yiğit and Medvedev*, 2019]. Due to their ability to transport energy and momentum upward, GWs are a key mechanism that drives vertical coupling between the lower and upper atmosphere [*Yiğit and Medvedev*, 2015]. The divergence of the GW momentum flux due to wave dissipation and/or breaking produces a body force that can accelerate or decelerate the mean flow at higher altitudes. Thus, understanding atmospheric coupling processes requires accurate quantification of the propagation and dissipation of gravity waves.

Recent missions to Mars have greatly improved our understanding of the planet's upper atmosphere; however, meaningful interpretations of the observed atmospheric variability and explanations of the underlying physical mechanisms can be achieved to a greater degree if observations are supported by theoretical modeling efforts. Although many physical and chemical processes responsible for the observed behavior of the upper atmosphere have been studied for decades [e.g., *Bougher et al.*, 1990, 1993; *Bougher et al.*, 2006], the impact of internal GWs on the Martian

thermosphere has been explored to a lesser extent. This paper aims to provide comprehensive three-dimensional simulations of the winds and temperature of the Martian upper atmosphere, accounting for and quantifying subgrid-scale GW effects.

Development of Mars general circulation models (GCMs) extending from the ground to the exobase provides a unique opportunity to investigate vertical coupling processes that link the entire atmosphere [*Bougher et al.*, 2015c; *González-Galindo et al.*, 2015]. Through utilization of parameterization schemes, Mars GCMs can account for the missing effects of unresolved GWs from the troposphere to the thermosphere, similarly to what is done in GCMs of the terrestrial atmosphere [*Yiğit et al.*, 2009]. Recent Mars GCM studies have used such schemes to study GW propagation into the thermosphere up to ∼160 km [e.g., *Medvedev et al.*, 2013, 2016; *Yiğit et al.*, 2018]. The first evidence that GWs which originate in the Martian troposphere can penetrate to the upper thermosphere was obtained in simulations with a linearized one-dimensional wave model [*Parish et al.*, 2009]. Later idealized numerical studies have supported this finding and further indicated that the associated GW drag is strong and sufficient for significant reduction, and even reversal, of the mean zonal jets in the mesosphere and lower thermosphere (MLT) region (100-130 km) [*Medvedev et al.*, 2011a]. This was demonstrated in the three-dimensional Mars GCM simulations of *Medvedev et al.* [2011b], which interactively included a non-orographic, whole atmosphere, spectral gravity wave parameterization [*Yiğit et al.*, 2008]. In addition to the strong dynamical forcing from GW momentum deposition, further Mars GCM studies have shown that GWs significantly cool the lower thermosphere [*Medvedev and Yiğit*, 2012], facilitate CO_2 ice cloud formation [*Yiğit et al.*, 2018], and modulate the circulation and temperature during global dust storms, thus changing the timing and intensity of the water transport into the upper atmosphere [*Shaposhnikov et al.*, 2022].

While previous Mars GCM studies which included subgrid-scale GWs focused on altitudes below ∼160 km, recent observations have provided further evidence that the upper atmosphere, even above these altitudes, is continuously populated by GWs of various spatiotemporal scales [e.g., *Yiğit et al.*, 2021]. GW-induced density perturbations in the Martian upper atmosphere have been identified from accelerometer-derived datasets from Mars Global Surveyor, Mars Odyssey, Mars Reconnaissance Orbiter, and ExoMars Trace Gas Orbiter [e.g. *Fritts et al.*, 2006; *Creasey et al.*, 2006; *Tolson et al.*, 2007; *Vals et al.*, 2019; *Jesch et al.*, 2019]. For example, *Creasey et al.* [2006] identified GWs with horizontal wavelengths of 100-300 km; these density perturbations associated with GWs also showed evidence of seasonal change. Additionally, GW momentum fluxes estimated from *Fritts et al.* [2006] were much larger than those seen at comparable densities at Earth, suggesting GWs would have considerable impact on large-scale mean velocities and their variability at Mars. The more recent MAVEN (Mars Atmosphere and Volatile Evolution) / NGIMS (Neutral Gas and Ion Mass Spectrometer) density dataset has also allowed for additional character-

ization of GW signatures throughout the thermosphere [e.g. *Yiğit et al.*, 2015; *England et al.*, 2017; *Terada et al.*, 2017; *Siddle et al.*, 2019]. The perturbations of density associated with GWs have been observed at the lowest altitudes of MAVEN's trajectory ($\sim$125 km) [*Siddle et al.*, 2019] and up to $\sim$250 km [*Yiğit et al.*, 2015]. *Yiğit et al.* [2015] found that in the upper thermosphere, density perturbations associated with GWs had amplitudes typically between 20-40% of the background density, with notable variability across local time, altitude, and latitude. At thermospheric altitudes, *Terada et al.* [2017] found that these wave structures have horizontal wavelengths between $\sim$100 and 500 km, while the amplitudes of these perturbations depend on the ambient temperature. *England et al.* [2017] similarly identified monthly-mean typical wavelengths of tens to hundreds of kilometers, in addition to determining that these GWs could generate heating/cooling rates of up to several hundreds of Kelvin per sol, in qualitative agreement with the predictions of *Medvedev and Yiğit* [2012] using a Martian GCM. A couple of different analyses of MAVEN/NGIMS densities showed that GW activity doubled during the 2018 Mars global dust storm [*Leelavathi et al.*, 2020; *Yiğit et al.*, 2021b].

Although analyses such as these suggest GWs are a regularly occurring phenomenon in the Martian upper atmosphere, the question of how to best represent GW effects in Mars GCMs is an active area of study and a still developing aspect of many Mars GCMs. Not all Mars GCMs currently include GW parameterizations, and many that do include them do not extend to the exobase. A recent review of GW effects in planetary atmospheres and approaches to their parameterization is given in the paper of *Medvedev and Yiğit* [2019].

The Mars Global Ionosphere-Thermosphere Model (M-GITM) is a ground to exobase 3-D Mars GCM that specializes in accurately representing the chemistry and physics relevant in the upper atmosphere. Previously, this model lacked a parameterization scheme for subgrid-scale GWs with non-zero phase speeds. While M-GITM has been able to reproduce many characteristics of the thermosphere reasonably well [e.g. *Bougher et al.*, 2015c; *Bougher et al.*, 2017b], and agrees qualitatively with other models, there were notable differences in the zonal and meridional wind structure in the MLT region when compared to other Mars GCMs which utilize GW schemes. Furthermore, when M-GITM simulations were compared to MAVEN/NGIMS neutral thermospheric wind measurements, in certain cases, large differences were found between the observations and the model simulations, likely pointing to impacts on the thermospheric winds from some physical phenomenon lacking in the model [*Roeten et al.*, 2019]. Since GWs have significant thermal and dynamical impacts on the mean state of the upper atmosphere [*Yiğit and Medvedev*, 2009; *Medvedev et al.*, 2013], a GW parameterization scheme has been added into M-GITM to better understand the effects these subgrid-GWs have on the winds and temperature structure at thermospheric altitudes.

The rest of this paper is organized as follows: The numerical tools used - M-GITM and the

GW parameterization scheme - are described in Section 3.4. Discussion of results from M-GITM simulations from two different seasons, solstice and equinox, are presented in Section 3.5. A series of sensitivity tests are discussed in Section 3.6, followed by two examples of comparisons between new M-GITM simulations and NGIMS datasets in Section 3.7. Conclusions and a summary of the findings can be found in Section 3.8.

3.4 Numerical Tools

3.4.1 The Mars Global Ionosphere-Thermosphere Model

M-GITM (Mars Global Ionosphere-Thermosphere Model) is a three-dimensional numerical model combining the original terrestrial GITM framework [*Ridley et al.*, 2006] with Mars fundamental physical parameters, ion-neutral chemistry, and key radiative processes. While the primary aim of this model is to compute the basic observed features of the thermal, compositional, and dynamical structure of the Mars upper atmosphere, M-GITM is a whole atmosphere general circulation model and extends from the ground to $\sim$250 km [*Bougher et al.*, 2015c]. For the Mars lower atmosphere (below 100 km) physical parameterizations (e.g. solar heating, aerosol heating, CO_2 15-μm cooling) are taken from the NASA Ames Mars General Circulation Model (MGCM) code [*Haberle et al.*, 1999]. A basic Conrath scheme [*Conrath*, 1975] is employed for the dust vertical distribution, while using a globally-averaged and seasonally-averaged optical depth value (see *Bougher et al.* [2015c]). For the Mars upper atmosphere (above $\sim$100 km), physical processes and formulations for EUV-UV heating, dissociation, ionization, CO_2 15-μm cooling, and ion-neutral chemistry are taken from the Mars Thermosphere General Circulation Model [*Bougher et al.*, 1999, 2000]. Simulated M-GITM prognostic fields include neutral densities (e.g. CO_2, Ar, O_2, CO, N_2, O, N, He), ion densities (e.g. O_2^+, CO_2^+, O^+, N_2^+, NO^+), 3-component neutral winds (zonal, meridional and vertical), and neutral temperatures. Electron temperatures are empirically prescribed from MAVEN observations [*Ergun et al.*, 2015]. Ion temperatures are based upon a Viking 1-2 empirical formulation from *Rohrbaugh et al.* [1979]. M-GITM is run on a 5x5° regular horizontal latitude-longitude grid, with 2.5 km vertical resolution in altitude.

Recent updates to the M-GITM code, as seen in *Roeten et al.* [2019], include a fast non-local thermodynamic equilibrium (NLTE) CO_2 15-μm cooling scheme, adapted from *González-Galindo et al.* [2013]. Its primary application is above $\sim$80 km where NLTE conditions prevail. Here, M-GITM simulated atomic O atoms collide with CO_2 molecules self-consistently, ultimately resulting in enhanced CO_2 cooling rates. Additionally, solar EUV-UV fluxes are now obtained from the Flare Irradiance Spectral Model - Mars (FISM-M) empirical model (outputs on a daily cadence), a product generated from the MAVEN Extreme Ultraviolet Monitor (EUVM) measured solar fluxes

[*Thiemann et al.*, 2017]. Finally, the EUV neutral heating efficiency in the thermosphere has been increased from 18% (the previous standard used in M-GITM) to 20% to better reflect recent findings from *Gu et al.* [2020].

A suite of M-GITM simulations have been compared with various MAVEN measurements obtained during its first three Mars years of operations. This includes measured densities and derived temperatures sampled during Deep Dip campaigns [e.g., *Bougher et al.*, 2015b, c; *Zurek et al.*, 2017] as well as dayside science orbits [e.g., *Bougher et al.*, 2017b]. Furthermore, a small set of MAVEN neutral thermospheric wind observations were compared with M-GITM velocities [*Roeten et al.*, 2019]. Simulations have also been conducted to compare to measurements obtained during the 2018 global dust storm [e.g., *Elrod et al.*, 2020; *Jain et al.*, 2020] and during solar flare events [e.g., *Fang et al.*, 2019]. Overall, MAVEN NGIMS, IUVS (Imaging Ultraviolet Spectrograph), and accelerometer measurements have been used extensively to validate the M-GITM code.

For this study, M-GITM simulations were run for 15 days, following a 20-day spin-up period to reach steady state conditions as the timeframe of interest is approached. These 15-day simulations have been averaged over all days, retaining local time and latitude information. Simulated fields have also been zonally averaged over all longitudes. Resulting zonally and temporally averaged fields will be described in this analysis.

3.4.2 The Whole Atmosphere Gravity Wave Scheme

Coarse-grid GCMs require appropriate GW parameterizations in order to account for the effects of subgrid-scale waves. The whole atmosphere nonlinear GW parameterization used in this study was initially developed for terrestrial GCMs and is fully described in the work by *Yiğit et al.* [2008]. Here we provide a concise characterization of the scheme, its implementation into the M-GITM model, and its application in previous terrestrial and Martian studies.

The parameterization calculates a vertical evolution of GWs from their sources in the lower atmosphere to the upper thermosphere. For this, first an appropriate distribution of GW activity must be specified globally at a source level in the troposphere. The wave activity is quantified in terms of the horizontal momentum fluxes $\overline{u'w'}$ as a function of horizontal phase speeds. An empirical Gaussian distribution of the momentum fluxes is assumed. Then, the vertical evolution of the horizontal momentum flux of a harmonic i with the phase speed c_i is given by

$$\overline{u'w'}_i(z) = \overline{u'w'}_i(z_0)\frac{\rho(z_0)}{\rho(z)}\,\tau_i(z) \tag{3.1}$$

where u' and w' are the horizontal and vertical components of the wind perturbations, $\overline{u'w'}_i(z_0)$ is the momentum flux of the harmonic i at the launch (or source) level z_0, $\rho(z_0)$ is the background mass density at the source, and τ_i is the transmissivity of the given wave, which controls the upward propagation of a given wave harmonic. If there are no wave breaking and dissipation, harmonics propagate conservatively, and $\tau_i = 1$. Then, the wave flux grows exponentially with height as the background density exponentially decays with height. Otherwise, $\tau_i < 1$, which means that the exponential growth of the wave flux is counteracted by wave breaking and/or dissipation. The transmissivity includes information on wave damping,

$$\tau_i(z) = \exp\left[-\int_{z_0}^{z} \beta_{tot}^{i}(z')\, dz' \right] \tag{3.2}$$

where the total vertical damping rate β_{tot}^{i} of a wave harmonic is a superposition of the damping due to molecular viscosity and nonlinear processes causing breaking/saturation [*Medvedev and Klaassen*, 2000]:

$$\beta_{tot}^{i} = \beta_{mol}^{i} + \beta_{non}^{i} \tag{3.3}$$

Other dissipative processes such as wave damping due to ion friction β_{ion} and eddies β_{eddy} can be included, as is done for Earth [e.g. *Yiğit et al.*, 2009; *Medvedev et al.*, 2017]. However, the former is small due to a lack of a strong global magnetic field on Mars and the latter is less constrained. Therefore, they have been excluded in this work. The β_{mol} and β_{non} terms are calculated using the same formulation as found in *Yiğit et al.* [2008] and *Medvedev et al.* [2011b]; see these for more detail.

The source of GW wave activity that needs to be specified in the lower atmosphere, from which upward computations are made by the GCM, is defined as a Gaussian spectrum in the form of:

$$\overline{u'w'}_i(z_0) = \mathrm{sgn}\big(c_i - \overline{u}_0\big)\overline{u'w'}_{max} \exp\Big[-\big(c_i - \overline{u}_0\big)^2 / c_w^2 \Big] \tag{3.4}$$

This function which describes the GW spectrum has also been used in the application of this scheme in previous Mars modeling studies [*Medvedev et al.*, 2011b; *Medvedev and Yiğit*, 2012; *Medvedev et al.*, 2013], where its justification has been discussed. An example of the source spectrum for select values of the mean wind at the source level can be seen in Figure 3.1. In this calculation for the momentum flux at the source level, the spectra of phase speeds, c_i, are described by the maximum phase speed and the number of harmonics used. Here 30 harmonics are used, with horizontal phase speeds from -80 to 80 m/s. The half-width of the spectrum at half-maximum, c_w, was set at 35 m/s. The mean wind at source level, $\overline{u}_0$, is a value the parameterization scheme takes

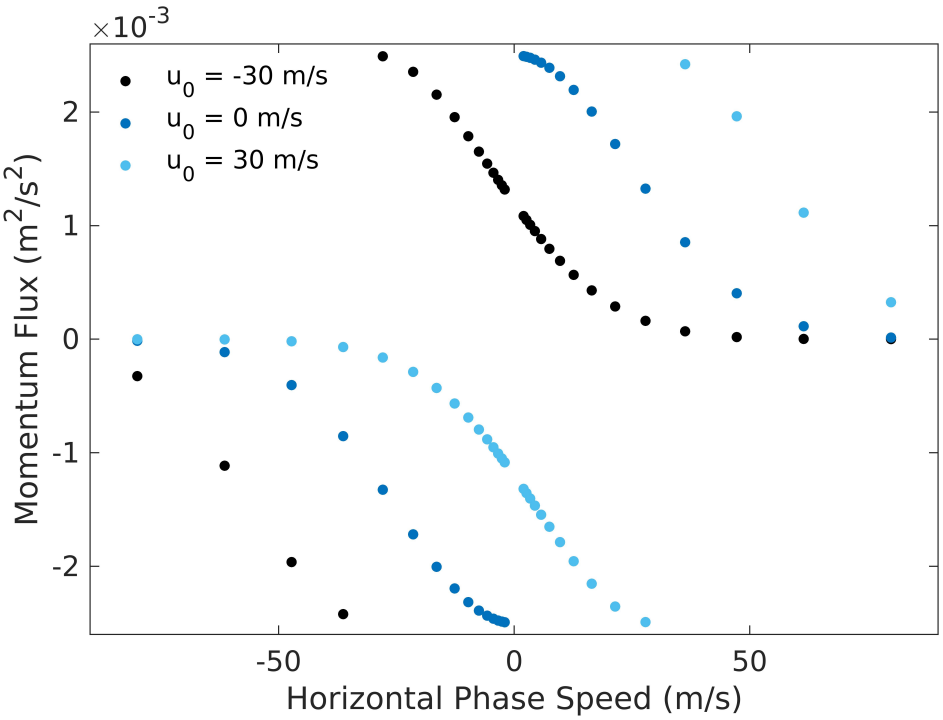

Figure 3.1: Examples of the type of GW momentum flux spectra at the source level used by the model. Different colors mark the fluxes for specific harmonics in three examples of potential source level winds, $u_0 = -30$, $u_0 = 0$, and $u_0 = 30$ m/s.

directly from M-GITM, but is typical of zero to tens of meters per second. The value of the maximum GW momentum flux at source level used is $\overline{u'w'}_{max}$=0.0025 m^2/s^2. This quantity has been commonly employed in previous Mars modeling studies using this GW scheme [e.g. *Medvedev et al.*, 2011b; *Medvedev and Yiğit*, 2012; *Medvedev et al.*, 2013, 2015; *Shaposhnikov et al.*, 2019] and was recently estimated from occultation measurements with the ACS (Atmospheric Chemistry Suite) instrument onboard TGO (Trace Gas Orbiter) [*Starichenko et al.*, 2021].

Somewhat better constrained is the horizontal wavelength of GWs in the Martian atmosphere, with estimates based on available observations ranging from tens of kilometers to hundreds of kilometers [e.g. *Creasey et al.*, 2006; *Fritts et al.*, 2006; *Siddle et al.*, 2019] (see Section 3.3). In this GW scheme, a single representative wavelength for the most dominant subgrid-scale GWs is used, which facilitates computational efficiency, as is typically done in subgrid-scale GW studies. A horizontal wavelength of 300 km was utilized here, which is within the range of observationally estimated values.

Finally, the altitude of the source flux of GW momentum has been set at 8.75 km (roughly equivalent to the 260 Pa level employed by *Medvedev et al.* [2011b] for this purpose). An altitude where weather processes are active, at or above the estimated average height of the convective boundary layer [*Hinson et al.*, 2008] were the key considerations for the source level. This was

done in order to reasonably represent the background winds near altitudes where non-orographic GWs may be launched. From this source level, the GW calculation is allowed to continue up to the top of the model, at 300 km.

In addition to the first use of this specific GW scheme in a Mars GCM [*Medvedev et al.*, 2011b; *Medvedev and Yiğit*, 2012], it has been applied in an increasing number of Mars modeling studies, including on topics of Mars global dust storm effects on the upper atmosphere [*Medvedev et al.*, 2013], as well as a comparison of thermal GW effects with CO_2 radiative cooling [*Medvedev et al.*, 2015] and water transport to the upper atmosphere [*Shaposhnikov et al.*, 2022]. The most recent terrestrial application of the scheme has studied the influence of latitude-dependent GW sources on the vertical coupling between the lower and upper atmosphere, using the Coupled Middle Atmosphere Thermosphere-2 GCM [*Yiğit et al.*, 2021a]. The scheme has been validated using other Earth GCMs as well [*Miyoshi and Yiğit*, 2019; *Lilienthal et al.*, 2020] and is a standard module of the Max Planck Institute Martian General Circulation Model.

3.5 Impacts of Gravity Waves in M-GITM Simulations

MGCM simulations are presented in this section for solstice ($L_s = 270°$) and equinox ($L_s = 180°$) conditions to study the impacts of GW effects in the upper atmosphere.

3.5.1 M-GITM Results from Solstice

The simulated zonal and meridional winds and the associated zonal and meridional gravity wave drag are presented in Figure 3.2 for $L_s = 270°$, southern hemisphere summer solstice. Simulation results both with and without the GW scheme are shown in order to demonstrate the effects of GWs on the circulation, especially in the thermosphere. The region of the greatest GW momentum deposition (i.e., GW drag) calculated by the whole atmosphere scheme occurs from ∼90-170 km, on average. During the southern hemisphere summer solstice, the peak mean GW drag magnitude is found at high latitudes in the southern hemisphere, where the absolute values reach 700 m/s/sol for the zonal drag and 920 m/s/sol for the meridional drag. The mean zonal GW drag is primarily directed eastward, except for a region at higher latitudes in the northern hemisphere, ∼40-70°N. The mean meridional GW drag is primarily southward, except for some low-magnitude northward drag at high latitudes in the northern hemisphere.

Notably, while the GWs dissipate over a broad range of altitudes in the upper atmosphere, the mean GW drag (for both the zonal and meridional components) calculated by M-GITM features a double maximum in altitude. The lower, narrower-in-altitude drag maximum is centered around 100 km and has an extent of only about 10 km. The other drag maximum occurs over a broader

range of altitudes, from about 120-160 km. GWs break and/or saturate at different locations in the whole atmosphere system depending on wave characteristics such as phase speed as well as on the characteristics of the background atmosphere. It is likely that the lower altitude population seen in Figure 3.2 is produced by nonlinear breaking/saturation, while the one at higher altitudes is due to exponentially increasing molecular diffusion and thermal conduction.

While there is a limited number of other modeling studies that both include a non-orographic GW scheme and extend through the thermosphere, these M-GITM calculations of GW drag in the thermosphere can, in part, be compared to those from *Medvedev et al.* [2011b], whose MGCM extended up to ∼130 km. The magnitude of temporally and zonally averaged GW drag of hundreds of meters per second per sol, up to 700 m/s/sol for the zonal GW drag, found by *Medvedev et al.* [2011b] within the altitude range of approximately 100-130 km from their $L_s = 270^\circ$ solstice simulation is comparable to that calculated by M-GITM. For zonal GW drag, while model simulations from both of these studies produce eastward drag in the southern summer hemisphere and westward drag in the northern winter hemisphere at middle-high latitudes within this altitude range, M-GITM produces larger GW drag in the southern hemisphere while the *Medvedev et al.* [2011b] study produces greater magnitudes in the northern hemisphere. This could be related to the slower eastward winds in the northern hemisphere produced by M-GITM than those that are seen in the solstice simulations from *Medvedev et al.* [2011b].

Figure 3.2 also shows that the GW drag calculated by M-GITM in the thermosphere primarily acts against the predominant zonal wind, resulting in a slower mean flow. This is most noticeable starting at approximately the same altitude range over which the GW drag magnitude is the greatest. For the zonal wind (in the top row of Figure 3.2) it can be seen that without including the effects of GWs, the model produces high-speed winds throughout the upper portion of the model domain, which are on average westward. Once the GW scheme is included, this splits into a notably slower upper thermospheric wind maximum and a middle atmospheric jet around 50 km, with the region between (∼100-150 km) now having average velocities of 20-40 m/s. From ∼100 km to the top of the model, with the addition of the GW scheme, mean westward speeds have decreased by up to ∼150 m/s and a better defined eastward flow appears in the northern hemisphere. This weakening of the zonal wind speed and closing off of the upper extent the middle atmospheric jet is a characteristic feature of the mesosphere and the lower thermosphere region on Earth and Mars due to GW momentum deposition and has also been seen in other studies [e.g., *Medvedev et al.*, 2011b; *Kuroda et al.*, 2016; *Watanabe and Miyahara*, 2009; *Miyoshi and Yiğit*, 2019; *Yiğit et al.*, 2021a].

For the meridional winds, the GW drag also primarily acts against the mean flow in the upper atmosphere. This results in near-zero average velocities near the same altitude range where the maximum GW drag is deposited, or even reversals in the average flow direction at middle-to-high

latitudes in both hemispheres. The decrease in velocity between the M-GITM simulations without and with GW effects can reach ∼40 m/s. This difference is not as large as was seen for the mean zonal winds, which might be expected since the mean meridional wind speeds in the initial no-GW simulation are much weaker than the zonal speeds. In addition to the large decrease in wind speed in the MLT region, the mean flow at most latitudes in the thermosphere is found to decrease in magnitude once the GW scheme is added, similar to the mean zonal wind.

The impacts of adding the GW scheme to M-GITM also appear in the zonally averaged temperature structure presented in Figure 3.3. The mean temperatures simulated in the thermosphere above ∼120 km are significantly cooler with the effects of GWs included, by up to 50 K. The greatest difference is seen at high latitudes in the northern winter hemisphere and at middle to high latitudes in the southern summer hemisphere. This is similar to what was found in *Medvedev and Yiğit* [2012], wherein after adding a GW parameterization scheme to a MGCM, resulted in temperatures at middle-to-high latitudes in the thermosphere (up to ∼150 km, the top of the model) cooling by up to 45 K compared to their simulation without GW effects. In addition to the changes in the thermosphere, as seen in Figure 3.2 in the middle atmosphere in the southern summer hemisphere, from about 50-100 km, the GW scheme produces somewhat warmer averaged temperatures in M-GITM than in the case without GW effects, by up to 20 K at the higher latitudes. This difference, however, is not as large in magnitude as is the temperature difference produced in the thermosphere.

The changes in temperature in the middle and upper atmosphere can have contributions both from changes in the large-scale dynamics that result in modified advection and adiabatic heating/cooling, as well as irreversible wave heating and heating/cooling due to divergence of wave flux, the latter two of which are accounted for within the GW scheme. These latter two, when combined, show the net GW heating or cooling calculated directly by the GW scheme. For the solstice, the mean rate of net GW heating in the thermosphere approaches ∼400 K/sol at high latitudes, particularly in the southern hemisphere. This is somewhat greater than the ∼200 K/sol from the solstice simulations of *Medvedev and Yiğit* [2012], though within the same order of magnitude.

3.5.2 M-GITM Results from Equinox

During the $L_s = 180^\circ$ equinox (southern hemisphere vernal equinox), after adding the GW scheme to M-GITM, a similar response can be seen in the upper atmosphere as occurred in the solstice simulation, though slightly subdued in comparison due to the slower mean winds this time of year. The general effect of the different season can also be observed in a more symmetrical distribution of wind velocities and corresponding GW drag with latitude in the equinox case.

The averaged GW drag calculated by M-GITM for the $L_s = 180^\circ$ equinox can be seen in the

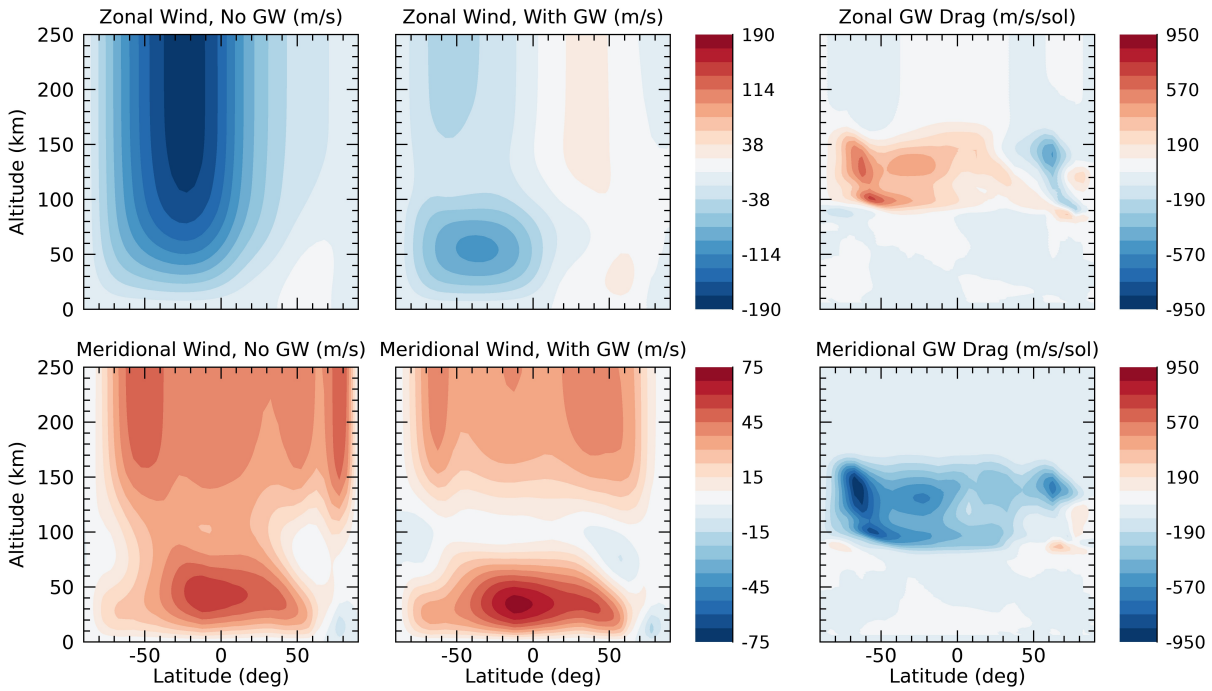

Figure 3.2: Zonally averaged zonal (top row) and meridional (bottom row) wind and GW drag from M-GITM, each also averaged over 15 days starting at $L_s = 270°$ (southern hemisphere summer solstice). The left column of plots shows the simulated wind velocity components when the effects of GWs are not included in M-GITM, while the middle column is the same but for when the effects of GW are included. The right column shows the averaged zonal and meridional GW drag.

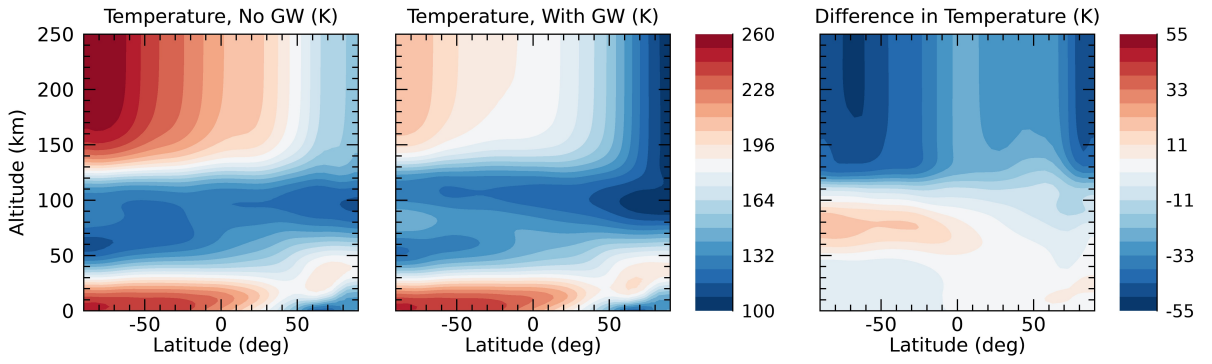

Figure 3.3: Zonally averaged temperature, also averaged over 15 days starting at $L_s = 270°$. The left column of plots shows the simulated temperatures when the effects of GWs are not included in M-GITM, while the middle column is the same but for when the effects of GWs are included. The right column shows the difference between the two (GW case - no GW case).

two panels in the right column of Figure 3.4. For the zonal GW drag, the greatest mean magnitudes are in a narrow band from ∼90-110 km, with the largest values of nearly 900 m/s/sol found at high latitudes. Regions of significant GW drag at higher altitudes, from ∼120-180 km, can also be seen, especially at higher latitudes. At these altitudes, eastward zonal drag extends throughout the low and middle latitudes; at higher latitudes, the averaged zonal GW drag is westward. The greatest mean meridional GW drag (up to 735 m/s/sol) is seen at high latitudes. Again, a double maximum feature in altitude can be seen, with a narrow band of GW drag around 90-110 km, and a broader drag maximum from ∼120-160 km. Like the mean zonal GW drag at high latitudes, the two maxima of mean meridional drag at these two different altitude ranges switch sign, though unlike the high latitude zonal GW drag, different hemispheres exhibit opposing senses of that sign.

Comparing the magnitude of zonal GW drag calculated by M-GITM between ∼100-130 km to that found in simulations from *Medvedev et al.* [2011b] for the $L_s = 180^\circ$ equinox, it can be seen that while both simulations have mean GW drag with orders of magnitude of hundreds of meters per second per sol, M-GITM values can be larger by a factor of two. Also, while *Medvedev et al.* [2011b] find meridional GW drag to be about three times weaker than the zonal GW drag in their MGCM, the difference between M-GITM zonal and meridional GW drag magnitudes is much less notable.

The left two columns of Figure 3.4 show the average zonal and meridional winds from the M-GITM equinox simulations, without and with subgrid GW effects included. When the GW scheme is added to M-GITM, the average zonal wind magnitude has a maximum of 40 m/s, with the largest averaged speeds found in the middle atmosphere rather than the thermosphere. Like for the solstice, the overall effect of GWs is to produce much slower mean winds throughout the thermosphere compared to the case when GW effects are not included, decreasing by as much as 100 m/s at these altitudes. The greatest impact is seen at middle-to-high latitudes above 100 km, where the inclusion of the GW drag results in a reversal of the flow from westward to light eastward winds, on average.

The addition of the GW scheme produces more complex changes in the mean meridional velocities. Most notably, starting around 120 km, the mean meridional velocities undergo a reversal in direction with the addition of subgrid-scale GWs. Above the altitude level that this reversal initially takes place, mean meridional speeds have increased in magnitude in the upper thermosphere slightly, but now have the opposite direction to that found in the case without the GW scheme.

Similar to the solstice simulation, adding the GW scheme to M-GITM in the equinox simulation again results in a much cooler thermosphere (above ∼90 km) on average compared to the run without GW effects, as seen in Figure 3.5. While the thermosphere appears cooler at all latitudes, the greatest difference (by up to ∼50 K, on average) between these two cases is found at high latitudes. Unlike in the solstice case, the addition of the GW scheme does not result in notably warmer

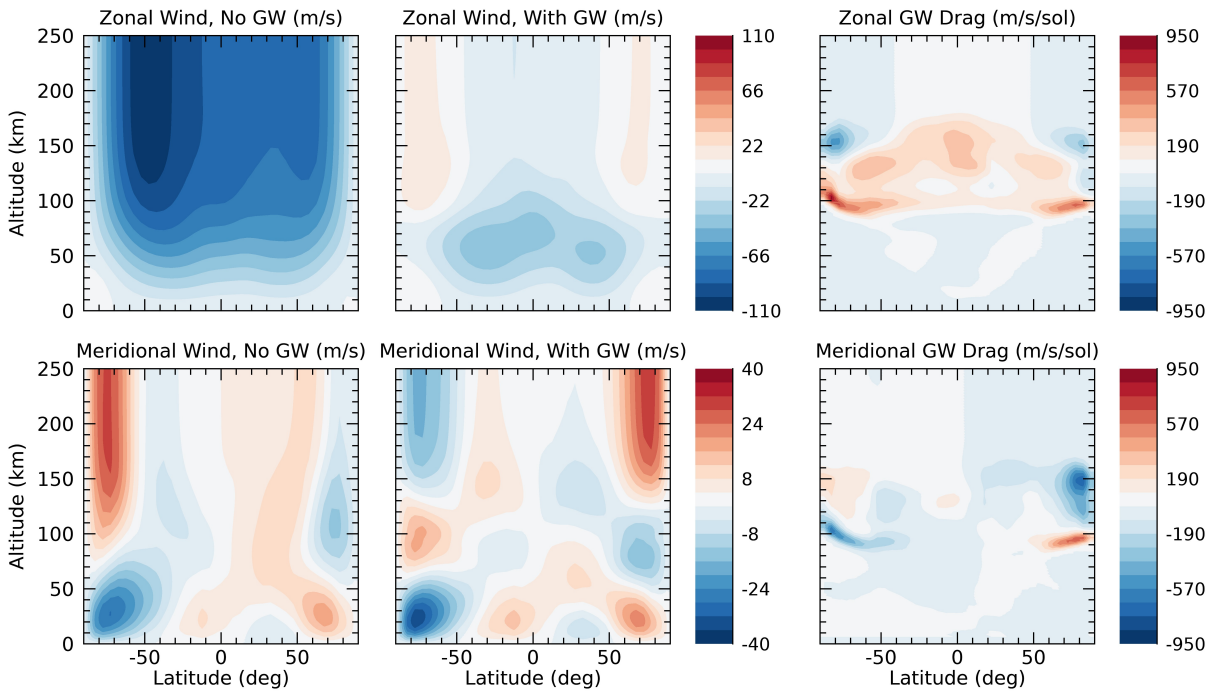

Figure 3.4: Same as Figure 3.2, but for the $L_s = 180°$ equinox (southern hemisphere vernal equinox).

temperatures in the middle atmosphere, instead remaining close to the same values between both simulations.

3.6 Sensitivity Tests

All atmospheric parameterizations include certain empirical (or tunable) parameters that act to quantify different aspects of the unresolved phenomena. In order to ascertain the sensitivity of M-GITM to the tunable parameters within the GW scheme, a series of tests were done. These tests were conducted with the characteristic horizontal wavelength, source flux magnitude, the maximum phase speed, spectrum half-width, number of harmonics, source height, and maximum height of allowed wave propagation. Here, the results from a subset of the simulations from the northern winter solstice ($L_s = 270°$) are described, namely, sensitivity tests with the horizontal wavelength and the maximum source flux. Adjustments to these two parameters produced some of the most significant changes in the model output compared to the other tunable parameters. All of these tests were performed with the same M-GITM set-up as described in Section 3.4.1, with the only differences being the change in the value of the selected parameter. Similar to the results shown in previous sections, the M-GITM results shown here are 15-day mean, zonally averaged

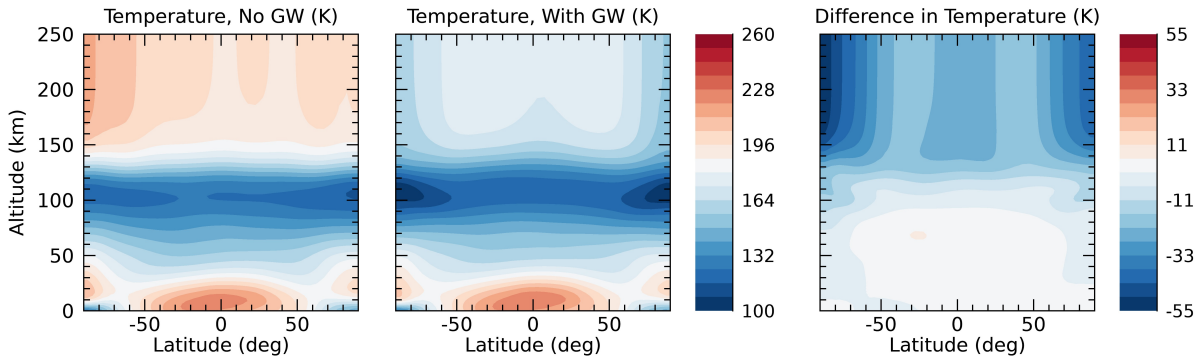

Figure 3.5: Same as Figure 3.3, but for the $L_s = 180°$ equinox.

fields. Plots of M-GITM results with these variations in maximum source flux and horizontal wavelength are included in Figures 3.6 and 3.7, respectively.

As described in Section 3.4.2, the source flux included in the GW scheme is based on a Gaussian distribution, which is allowed to be shifted by the background winds at the source level z_0, with the maximum source flux $\overline{u'w'}_{max}$ value as a tunable parameter based on previous estimates of GW source strength on Mars [*Medvedev et al.*, 2011a]. For the sensitivity tests, the baseline value of the maximum source flux, 0.0025 m^2/s^2, has been decreased to 10% of the baseline value (0.00025 m^2/s^2) and increased by a factor of two from the baseline (0.005 m^2/s^2). While this parameter is currently poorly constrained due to a scarcity of available observations, this range is one that has also been employed by other Mars GCMs that have implemented this GW scheme [e.g., *Medvedev et al.*, 2013, 2015; *Yiğit et al.*, 2018].

The horizontal wavelength of gravity waves is somewhat better constrained by available observations at Mars, particularly with new MAVEN data. At thermospheric altitudes, analyses of perturbations in NGIMS density observations (assuming along-track variation is horizontal), was found to be 200-400 km by *Terada et al.* [2017] and 100-300 km by *Siddle et al.* [2019]. A similar range for horizontal wavelength was identified by *Creasey et al.* [2006] of 100-300 km from Mars Global Surveyor accelerometer data. For our sensitivity tests with M-GITM, the horizontal wavelength was decreased from 300 to 200 km, a value within the ranges previously suggested by data analysis.

In these M-GITM simulations, the effects of changing the maximum source flux shifts the altitudes of the most significant GW momentum deposition (see Figure 3.6). For the case in which the maximum source flux is increased by a factor of two, the lower edge of the region of maximum GW drag (both zonal and meridional) is found at ∼90 km in the summer hemisphere (∼80 km in the winter hemisphere) while for the case with maximum source flux at 10% of baseline value,

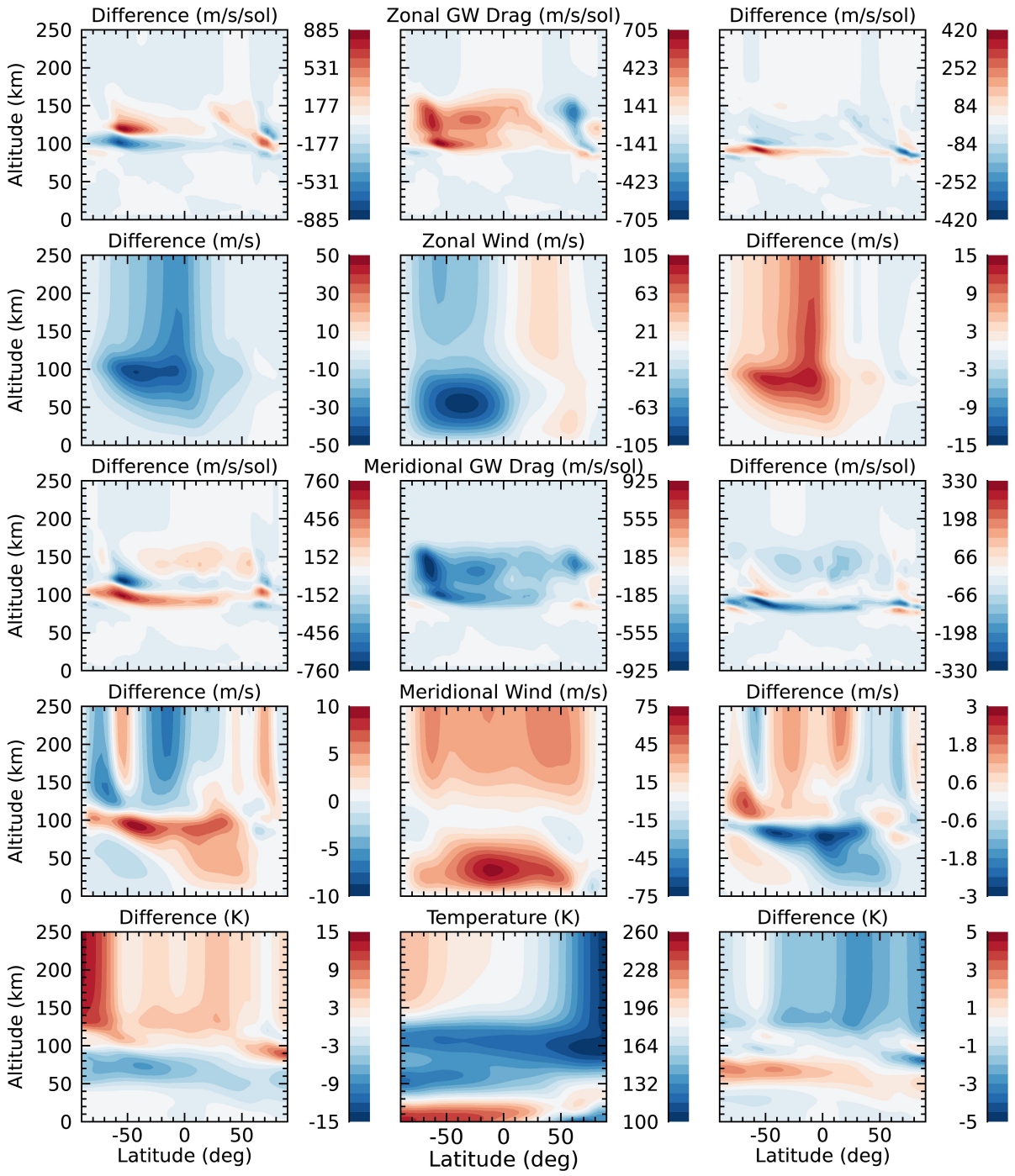

Figure 3.6: M-GITM results showing model response to adjusting the maximum flux of the source GW spectrum. The left column shows the differences between the baseline case and the case with the maximum source flux at 10% of the baseline value (0.00025 m^2/s^2), the middle column shows the baseline case (0.0025 m^2/s^2), and the right column shows the differences between the baseline case and the factor of two increase from the baseline value (0.005 m^2/s^2). Rows show, from top to bottom, zonal GW drag, zonal wind, meridional GW drag, meridional wind, and temperature. All plots show 15-day time averaged and zonal mean fields.

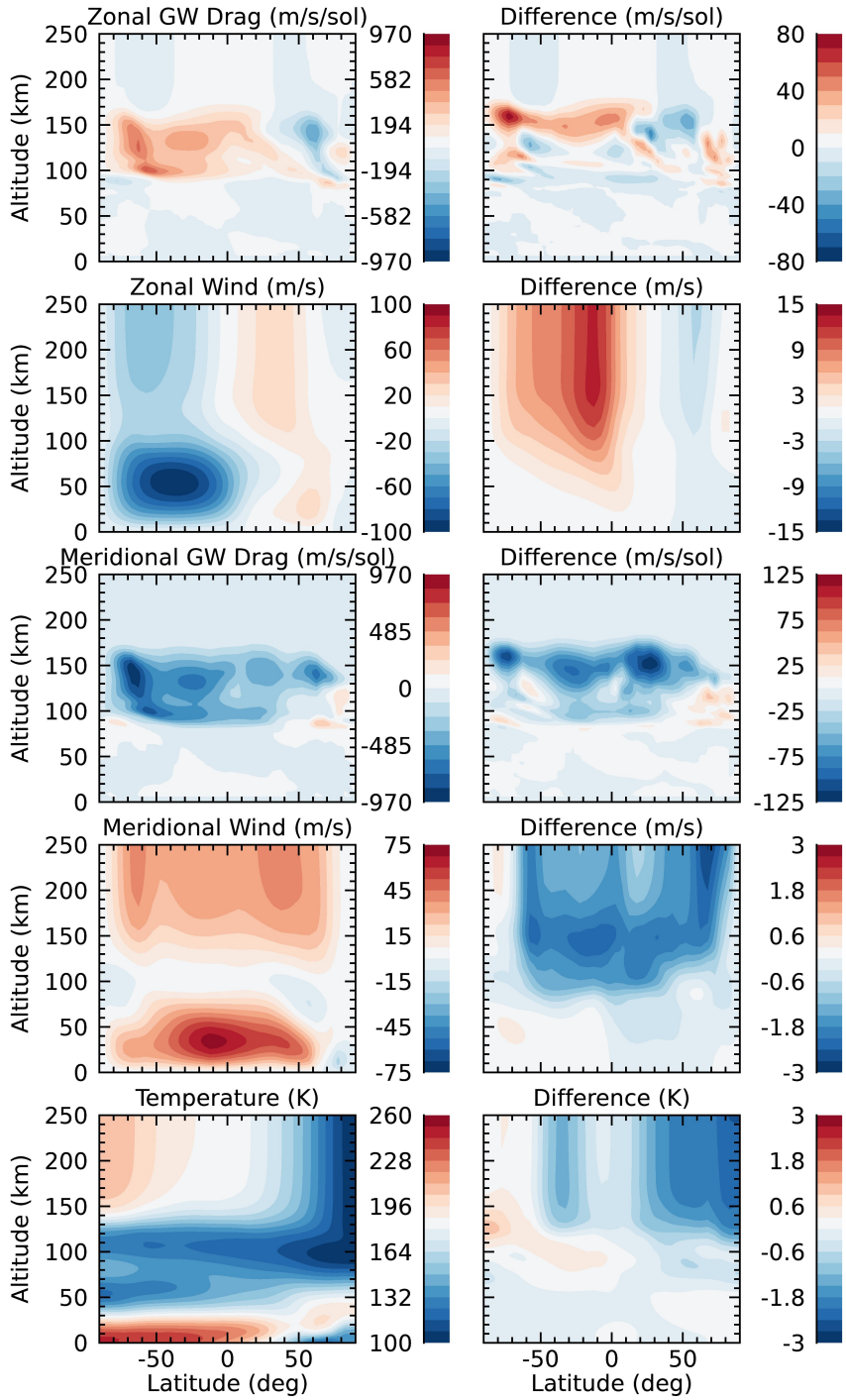

Figure 3.7: M-GITM results showing model response to adjusting the horizontal wavelength used in the GW scheme. The left column shows the case where the horizontal wavelength has been decreased to 200 km and the right column shows the differences between the baseline value (300 km) and the case with a horizontal wavelength of 200 km. Rows show, from top to bottom, zonal GW drag, zonal wind, meridional GW drag, meridional wind, and temperature. All plots show 15-day time averaged and zonal mean fields.

the lower edge of this region has shifted to ∼110 km in the summer hemisphere (∼100 km in the winter hemisphere). In the 10% of baseline value case, the altitude of the lower maxima shifted to high enough altitudes that the two distinct altitude bands with GW drag maxima have seemingly merged into one. This produces a greater maximum GW drag magnitude than in either the baseline case or the case with the factor of two increase in maximum source flux. Hence, with a greater maximum source flux, significant wave breaking and/or saturation occurs at slightly lower altitudes. To a lesser degree, the edge of the GW drag maxima at higher altitudes also shifts upward in altitude as the maximum source flux increases, but only by ∼5 km or less in these cases. Overall, the combination of these effects demonstrates that as maximum source flux increases, waves of different phase speeds break and/or saturate across a slightly wider range of altitudes in the upper atmosphere.

Figure 3.6 also indicates that as the maximum source flux increases, mean westward wind velocities in the summer hemisphere decrease in magnitude. A greater change in the mean zonal wind velocities is found between from the 10% of baseline value case and the baseline case than from the baseline case to the case with the factor of two increase in maximum source flux. These differences are on the order of several tens of meters per second and 10 m s^{-1}, respectively. Mean meridional velocities show differences from the baseline case up to 10 m/s. In the thermosphere as the maximum source flux increases, the mean northward meridional speed decreases in the higher latitudes while increasing at low latitudes.

The zonal mean temperatures become cooler at most latitudes above ∼120 km as the source flux increases, except for a region of the northern hemisphere middle latitudes ($\sim 55 - 65°$) in the case in which the maximum source flux increases by a factor of two, which warms by several degrees. From the case with 10% of the baseline source flux to the baseline case, the greatest averaged temperature difference is nearly 15 K lower in the southern hemisphere at high latitudes and above 120 km. There is also a region of warming from 40-90 km, particularly in the summer hemisphere. Examining the differences between the baseline and two times increase in source flux shows a slightly different pattern above 120 km. While most of the thermosphere cools in comparison to the baseline case (except for southern mid-latitudes), the greatest change is lower temperatures in the northern middle to high latitudes, though with only a few degrees Kelvin of difference.

Results from the sensitivity test in which horizontal wavelength was decreased from the baseline value of 300 km down to 200 km are shown in Figure 3.7. For the zonal and meridional GW drag, the changes occur primarily in the upper altitude part of the area of maximum drag (∼140-170 km), while the lower extent of this region (∼90-140 km) experiences relatively little change from the baseline case. On average, an increase in magnitude on the order of several tens of meters per second per sol for zonal GW drag and up to 100 m/s/sol for meridional GW drag is found in the

higher altitude region and across most latitudes, except for higher latitudes in the northern winter hemisphere. Unlike the source flux sensitivity tests, essentially no shifting of the altitude range of the region of most significant GW drag occurs.

Additionally, in these M-GITM simulations, as the horizontal wavelength decreases, the magnitude of the westward mean zonal wind speeds in the thermosphere decreases by up to $\sim$10 m/s on average. Unlike the tests with varying source flux, which results in notable changes in the middle and upper atmosphere in the summer hemisphere, these simulations primarily show changes in the mean zonal winds above $\sim$90 km in the summer hemisphere. The differences in meridional winds are smaller on average, with changes on the order of a few meters per second above $\sim$90 km. The changes in the meridional wind velocities consist predominantly of a decrease in the northward winds across all latitudes.

The zonally averaged temperatures respond slightly differently to the changed horizontal wavelength than they do to changing the maximum source flux as well. Averaged difference in temperature is on the order of a few degrees Kelvin throughout the domain. Similar to increasing the source flux, decreasing the horizontal wavelength also results generally in a cooler thermosphere, with greatest changes seen at high latitudes in the northern winter hemisphere. However, in the southern summer hemisphere, slightly warmer averaged temperatures are found at latitudes above $\sim 50^{\circ}$ above 100 km as well as at latitudes down to $\sim 0^{\circ}$ at altitudes of $\sim$80-120 km.

Overall, the relatively small differences in M-GITM simulations using either 200 km or 300 km for the horizontal wavelength indicate that the scheme is robust with respect to the expected values for this parameter. Somewhat larger changes are observed when the source flux magnitude is changed, particularly when it was adjusted by an order of magnitude. However, the changes in the simulated fields generated when the scheme itself is added to M-GITM are still larger in magnitude than in these sensitivity tests (i.e. Figures 3.2 and 3.3). If evidence were found in future data analysis that suggested the source flux was significantly different under certain atmospheric conditions than what was used here, under these new constraints, the altitude range where the most significant GW drag is deposited could shift further. As demonstrated in these tests, this would impact both the simulated mean wind speeds in the upper atmosphere as well as the temperature structure.

3.7 Data-Model Comparisons with MAVEN/NGIMS and M-GITM

In order to further study the impacts of the GW scheme in M-GITM, as well as to examine how well these new M-GITM simulations replicate observed thermospheric conditions, select data-model

comparisons have been conducted. Two in-situ datasets from the NGIMS instrument onboard the MAVEN spacecraft were used in comparison with simulated thermospheric fields from M-GITM. NGIMS is a quadrupole mass spectrometer designed to characterize the neutral and ion composition of the upper atmosphere of Mars. It has a vertical resolution of 5 km and target accuracy of $<$25% for most species, with observations generally taken from $\sim$150 km altitude through the exobase [*Mahaffy et al.*, 2015b, a].

3.7.1 M-GITM Comparisons with NGIMS Derived DD2 Temperatures

The first dataset used is the Level 2, Version 8, Revision 1 (V08R01) data product which consists of fully calibrated single species abundances [*Mahaffy et al.*, 2015a]. These NGIMS densities were then converted into temperatures using the method described in *Bougher et al.* [2017b]. A similar method is also used in *Stone et al.* [2018] and *Snowden et al.* [2013] to calculate temperature profiles. In this method, the hydrostatic equation is vertically integrated (assuming the vertical density profile is in hydrostatic equilibrium) using NGIMS Argon density profiles to find the local partial pressure. Profiles tend to converge below a certain altitude range regardless of the of upper boundary conditions used, as long as it is within a realistic range. This altitude range was identified to be generally between 200-220 km for perihelion conditions and 190-200 km for aphelion conditions [*Bougher et al.*, 2017b]. As such, temperature profiles for this study are only analyzed below these altitude ranges for the appropriate season. Furthermore, since the spacecraft's trajectory has a larger horizontal component near periapsis, and the hydrostatic method for deriving temperatures assumes a vertical integration, roughly a scale height at the bottom of the profile has been left out of the analysis. Finally, temperature profiles are calculated from the local partial pressure and Ar densities using the ideal gas law. Ar densities are used since the gas is immune to buffering by interactions with the instrument walls, unlike other reactive species [*Mahaffy et al.*, 2015a]. In order to remain consistent with previous studies that have derived temperature profiles from NGIMS data [e.g., *Bougher et al.*, 2017b; *Stone et al.*, 2018], only the inbound segment of Ar observations are used in this analysis.

Early in the MAVEN mission, the spacecraft completed several week-long campaigns to lower the nominal science orbit periapsis altitude from $\sim$150 km down to $\sim$125 km [*Jakosky et al.*, 2015]. One of those campaigns, called Deep Dip 2 (DD2) is used in this analysis to compare to the updated M-GITM simulations. DD2 spans MAVEN orbits 1059-1086, over the southern low-latitudes (22°S to 11°S) during the late southern hemisphere summer ($L_s \sim 330°$), near noon (11-12 LT). Density profiles from these orbits have been averaged to produce a single campaign-averaged profile. This averaging is done over longitude and time (i.e. orbit), preserving latitude and altitude information along the track. Latitude and local time only precess slightly between

sampling points at similar altitudes in consecutive orbits.

M-GITM simulations to compare to the DD2 campaign were run for the same time period the campaign took place, utilizing the appropriate FISM-M solar fluxes [*Thiemann et al.*, 2017] derived from EUVM observations during the campaign. Note that the values of the GW parameters used within the DD2 M-GITM simulations are the same as those used in the $L_s = 270^\circ$ baseline GW case described in Section 3.5.1. From these simulations, for each orbit in DD2, temperature and density profiles were extracted along the same trajectory flown by MAVEN in latitude, local time, and altitude. These M-GITM 'flythroughs' correspond to each MAVEN orbit during the campaign. A conversion between the aerocentric coordinate system native to the model and the aerodetic coordinate system used by NGIMS was also implemented in this process. The resulting M-GITM flythroughs allow for a more direct comparison between output from the model and in-situ NGIMS data. Inbound segments of M-GITM DD2 flythroughs were then averaged together in the same manner as was done for the calculated NGIMS density profiles to produce a campaign averaged profile.

Figure 3.8 shows the averaged NGIMS temperature profile from DD2 and two averaged M-GITM profiles, one which takes into account the effects of subgrid GWs, and one which does not. The original M-GITM profile, which does not utilize the GW parameterization scheme, is nearly 20 K warmer than the NGIMS DD2 profile at the top of this altitude range (near the exobase) and up to nearly 30 K warmer at 180 km and below. Once the GW scheme is added to the model, the temperature profile becomes $\sim$15 K cooler near 220 km to $\sim$10 K cooler by 150 km. This results in M-GITM reproducing the observed temperatures from 200-220 km. Though the differences between simulated and observed temperatures are greater below these altitudes, adding the GW scheme does still notably improve the comparison. At the altitudes of $\sim$140-190 km for DD2, the mis-match between data and model may be due to low atomic O abundances simulated in the model with respect to NGIMS measured values [*Bougher et al.*, 2017a]. Future work will require a sensitivity analysis to address the impact of variable eddy coefficients upon atomic O and the resulting dayside temperatures in M-GITM for DD2 conditions.

3.7.2 M-GITM Comparisons with NGIMS Wind Campaigns

In addition to the nominal density dataset, NGIMS has been able to provide in-situ measurements of neutral thermospheric wind velocities. These wind observations provide a way to more directly test the dynamics and circulation produced by M-GITM, though on a somewhat limited case-by-case basis. Two of these wind measurement campaigns were utilized in this analysis for data-model comparison.

The NGIMS neutral wind dataset has been generated through a novel observational technique

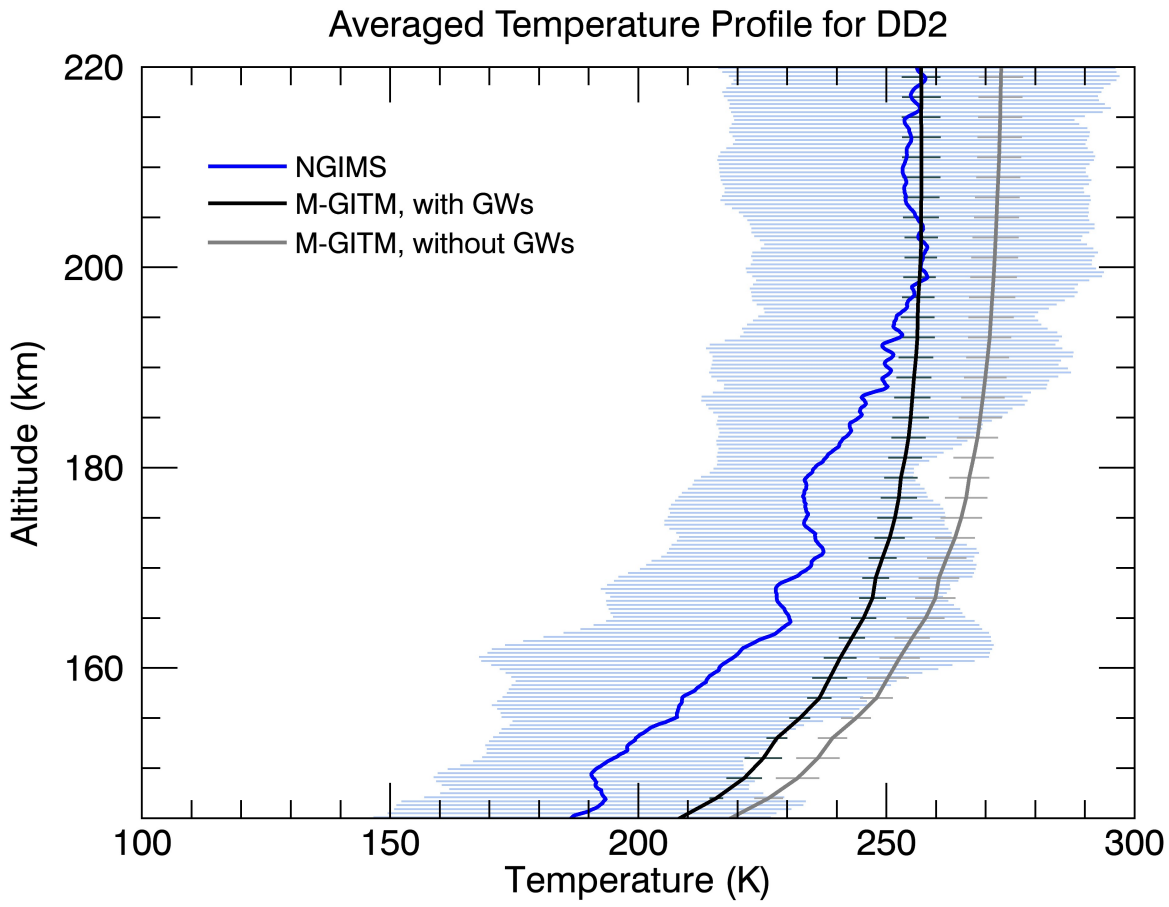

Figure 3.8: Averaged NGIMS and M-GITM temperature profiles for the NGIMS Deep Dip 2 (DD2) campaign. The blue profile shows the temperature profile derived from NGIMS Argon densities. The black and gray profiles are extracted from M-GITM simulations for the same DD2 time period and trajectory flown by MAVEN/NGIMS, with the black profile showing results for the case with the effects of subgrid GWs included, and the gray profile showing results for the case without the effects of subgrid GWs. The horizontal bars along the profiles indicate one standard deviation of orbit-to-orbit variability.

Table 3.1: Characteristics of NGIMS Wind Campaigns used in Data-Model Comparisons

Date	Orbits	Local Time (hr)	Latitude (deg)	L_s (deg)[a]
11 – 13 January 2017	4437 – 4446	23 – 1	38°S – 66°S	297
30 May – 1 June 2017	5170 – 5179	10 – 11	30°N – 61°N	12

[a]Approximate solar longitude

whereby the boresight of the NGIMS instrument onboard MAVEN is rapidly and continuously varied though the instrument platform nodding $\pm 8^{\circ}$ off the ram direction. Wind velocities are then determined from the observed modulations of neutral and ion fluxes as the instrument pointing direction is changed. A detailed explanation of how NGIMS carries out this measurement can be found in the work by *Benna et al.* [2019]. The thermospheric wind is sampled every $\sim$30 s along an altitude range of $\sim$140 up to 220 km. Along- and across-track wind magnitudes have an uncertainty typical of 20 and 6 m/s, respectively. Uncertainties are dominantly due to errors in the reconstructed spacecraft ephemeris and the instrument boresight direction, the energy resolution of NGIMS's mass filter, and in counting statistics [*Benna et al.*, 2019]. In order for the horizontal winds to be determined, it is assumed that vertical winds are negligible and that horizontal winds do not change on time scales shorter than the 30 s it takes for the instrument boresight direction to complete a full motion cycle. Since nominally, the Martian atmosphere is in hydrostatic equilibrium, vertical velocities might be expected to remain small if not driven by extreme solar events like flares [*Bougher et al.*, 2015c]. In addition, *Benna et al.* [2019] found good fits between observations over the 30 s sampling period to the expected modulation in fluxes if constant winds over this time was assumed, indicting no appreciable uncertainty is added due to $<$30 s wind variations. Zonal and meridional neutral wind measurements from the NGIMS Level 3, Version 3, Release 1 (V03R01) dataset were used in this study.

NGIMS wind measurements are generally conducted in campaigns occurring monthly, each with 5-10 consecutive orbits of wind observations taken along MAVEN's track through the thermosphere (passing through the same latitudes, local times, and altitudes, but different longitudes throughout a single campaign). Two examples of these wind observational campaigns, the January 2017 and May 2017 campaigns, are presented with corresponding M-GITM simulations. Specific characteristics of these campaigns can be found in Table 3.1. For each campaign, measurements in each orbit are averaged together over time and longitude to produce a single profile along MAVEN's trajectory in latitude, local time, and altitude, in a similar manner done with the NGIMS campaign-averaged temperature and density profiles in the previous section.

The M-GITM simulations run for both these wind campaigns utilize the same GW parameters as used in the $L_s = 270^{\circ}$ baseline case from Section 3.5.1, with the only differences being the dates, orbital parameters, and solar flux. Model wind flythroughs were done in the same manner as

was done for temperature flythroughs for DD2, extracting M-GITM output along the same latitude, local time, and altitude track traversed by MAVEN each orbit during the campaign. These were then likewise averaged (keeping the inbound and the outbound segments of each orbit separate) to produce a campaign-averaged profile that tracks over latitude, local time, and altitude.

The January 2017 campaign took place near perihelion, at midnight local time, and southern middle-to-low latitudes (see Table 3.1) and is shown in Figure 3.9. Prior to adding the GW parameterization scheme to M-GITM, the simulated speed along the averaged profile was in the range of 200-300 m/s faster than the averaged speeds observed by NGIMS, with an equally poor match in averaged direction along the profile. This has also been noted in an earlier data-model analysis of this campaign from *Roeten et al.* [2019]. By accounting for subgrid-scale GWs, the average speed profile slows by over 100 m/s, reducing differences between the observed and modeled speeds to less than 100 m/s on the outbound segment of the NGIMS trajectory and from 0-50 m/s on the inbound segment. This is a significantly improved match to the NGIMS campaign-averaged speed when compared to the thermospheric wind speed predicted by M-GITM when subgrid GWs were not accounted for, and suggests that GW effects are a significant factor in producing the observed mean flow speeds in this latitude-LT sector for this campaign.

Additionally, with the inclusion of the GW scheme, the simulated averaged wind direction for this campaign also shifts, now having less strong of a westward component while retaining the northward component. However, this change does not notably reduce differences in direction between mean observations and model flythroughs. This might, in part, be due to the significant orbit-to-orbit and sampling-point-to-sampling-point variability observed during this campaign, reported by *Roeten et al.* [2019]. The high amount of variability makes the interpretation of the average direction difficult. Furthermore, this level of small-scale variability, whether it be temporal or spatial variability (or both) cannot be replicated by M-GITM. Though observations suggest GWs produce significant variability in the thermosphere [e.g., *Yiğit et al.*, 2015], M-GITM cannot produce these individual perturbations; rather, the GW scheme introduced in M-GITM was designed to account for quantities averaged over the wave phases, in particular the momentum flux. While the significant directional variability in this case will make the average direction difficult for M-GITM to reproduce regardless of the addition of the GW parameterization scheme, the notable improvement in the mean speed for this campaign once the GW scheme is added suggests that M-GITM is better capturing a key atmospheric process.

The May 2017 campaign occurred near northern hemisphere vernal equinox, on the dayside, and at northern middle latitudes (see Table 3.1). In the M-GITM run without the GW scheme, as shown in Figure 3.10, the outbound segment of the profile at higher altitudes is a reasonable match to averaged speeds observed by the outbound segment of averaged NGIMS data, though the inbound segment is 50-100 m/s faster than observed. Once the GW scheme is added, average

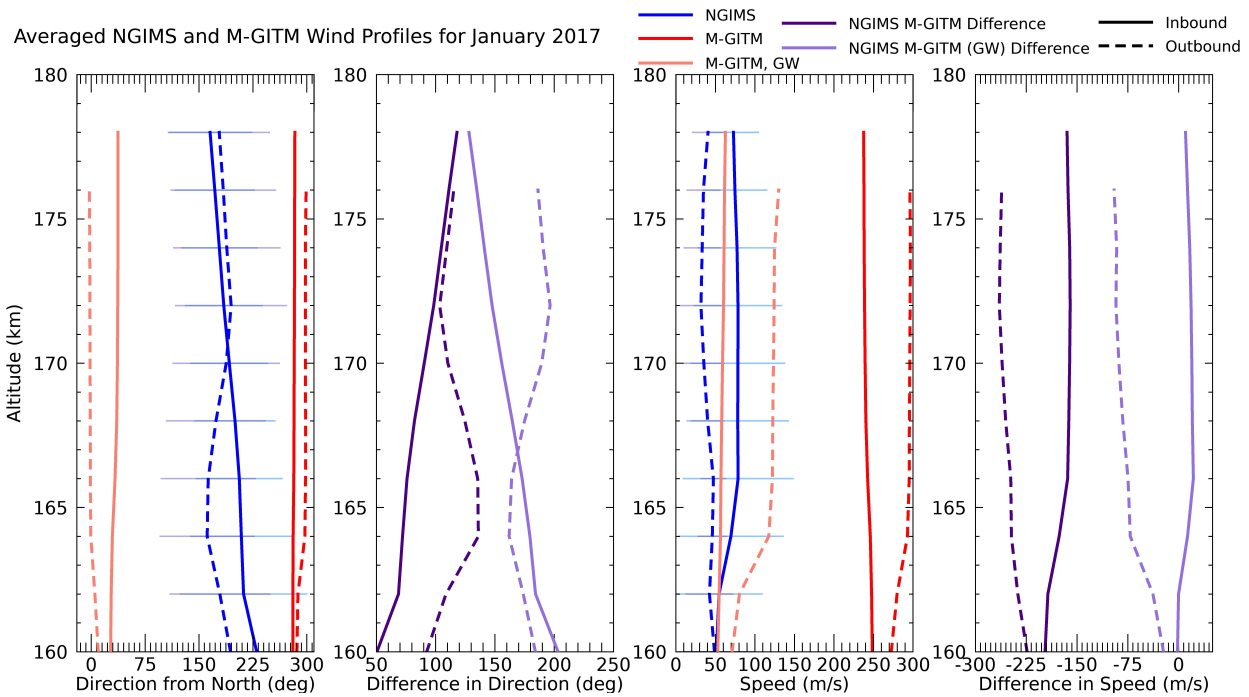

Figure 3.9: Averaged NGIMS and M-GITM wind profiles for the January 2017 campaign. The first plot shows wind direction (with 0° indicating winds blowing to the north), the second shows difference in direction between the NGIMS observations and model flythroughs, the third shows the wind speed, and the fourth shows the difference in speed between the NGIMS observations and model flythroughs. Blue profiles are NGIMS averages, with horizontal bars showing one standard deviation of orbit-to-orbit variability. Red colors show averaged M-GITM flythroughs, with darker red indicating the M-GITM simulation without the GW parameterization and lighter red indicating the simulation which utilized the GW parameterization. Solid lines show the inbound segment of the trajectory, while dashed lines show the outbound segment.

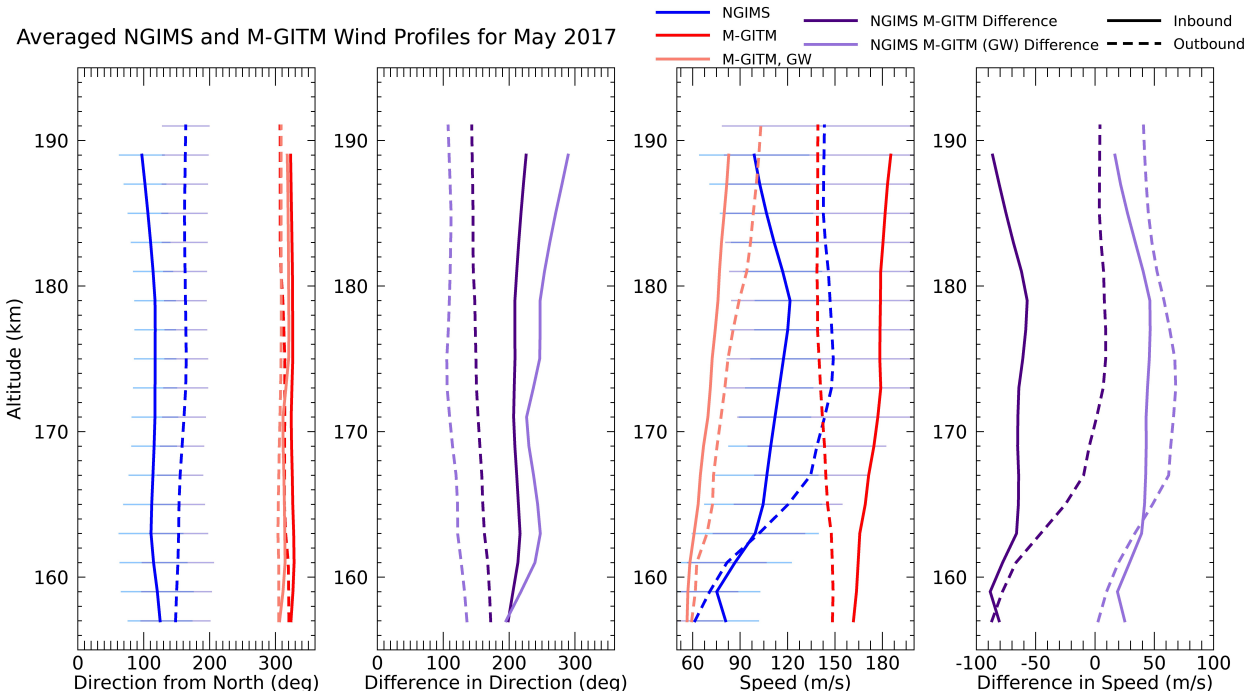

Figure 3.10: Averaged NGIMS and M-GITM wind profiles for the May 2017 campaign. These plots are set up in the same manner as was described in Figure 3.9.

simulated speeds decrease by nearly 100 m/s along the profile. This results in a closer match to the observed speeds at the lowest altitudes, but little to no improvement elsewhere. The averaged direction of the simulated velocities shifts negligibly, by less than ten degrees along the profile with the addition of the GW scheme. Notably, the original match between the data and model for the average direction was also poor, being nearly 180° degrees opposed to the direction the model suggests at this local time and latitude sector. The addition of the GW scheme does not discernibly modify this behavior. This might indicate that there are still aspects of the dynamics and circulation in the thermosphere which may be poorly understood and missing from models like M-GITM. Further modeling studies are needed to determine what may be driving this unexpected flow direction.

3.8 Summary and Conclusions

Gravity waves (GWs) are a key mechanism that facilitates coupling between the lower and upper atmosphere. In order to study the influence of small-scale gravity waves in the Martian thermosphere, a nonlinear whole atmosphere GW parameterization scheme [*Yiğit et al.*, 2008] has been incorporated into the Mars Global Ionosphere-Thermosphere Model (M-GITM) [*Bougher et al.*, 2015c] for the first time. Both the GW parameterization scheme and M-GITM are specifically

designed to be able to account for physics appropriate for the thermosphere, a region of the atmosphere many other Mars GCMs only partially cover or do not include at all.

Once the parameterized GW momentum deposition and thermal effects are added to the model, zonally and temporally averaged GW drag magnitudes of several hundreds of meters per second per sol are calculated in the thermosphere, particularly within the altitude region spanning 90-170 km. Within this altitude range, GW drag is typically found in two distinct maxima, one in a narrower band of altitudes centered around 90-100 km, and a broader maximum from ∼150-170 km.

M-GITM simulations which included the GW scheme were done for both the southern hemisphere summer solstice ($L_s = 270°$) and southern hemisphere vernal equinox ($L_s = 180°$) seasons. Somewhat larger mean GW drag magnitudes were found in the solstice season as well as a different latitudinal distribution of GW drag due to the changes in background winds with season.

In these M-GITM simulations, momentum deposited by the parameterized sub-grid GWs primarily acts to slow the winds in the upper atmosphere, and particularly in the region from ∼100-150 km, where this decrease in simulated speed effectively acts to close off the jets in the middle atmosphere, which has also seen in other studies [e.g. *Medvedev et al.*, 2011b; *Yiğit et al.*, 2018]. Throughout the thermosphere (at different latitudes depending on the season), simulated mean zonal winds decrease appreciably (by up to several tens of meters per second) compared to the M-GITM simulation without the GW parameterization scheme. The mean meridional wind response tends to be more complex, and can undergo reversals in direction starting at ∼100 km, particularly during the equinox.

The net thermal effects of the sub-grid GWs in M-GITM lead to a cooler thermosphere at most latitudes than would be otherwise above ∼120 km in simulations of both seasons. Changes in the temperature structure in the model are a result of a combination of the contributions from the GW heating/cooling terms calculated by the GW scheme itself as well as a result of the changes to the background winds in the model, which in turn modifies temperature advection and adiabatic heating. Additionally, the middle atmosphere (∼50-90 km) becomes slightly warmer at the solstice with the addition of the GW scheme to M-GITM.

A series of sensitivity tests was completed wherein certain adjustable parameters within the GW scheme were systematically varied. While results from this testing confirms that the GW scheme is robust within the model, some notable variations can occur in mean upper atmospheric winds and temperature with large changes in the horizontal wavelength and the maximum momentum flux at the source level. When horizontal wavelength is decreased by 100 km, there is an increase in the mean magnitude of momentum deposited at higher altitudes, near ∼140-170 km. As the maximum momentum flux at the source level increases, sub-grid GWs tend to deposit momentum at slightly lower altitudes (a change of ∼10 km when the maximum source flux is doubled).

Two types of comparisons were also shown between M-GITM simulations and thermospheric

observations from MAVEN/NGIMS. Comparing a temperature profile from Deep Dip 2, one of NGIMS special observational campaigns, to M-GITM flythroughs, it is found that the addition of the GW parameterization cools down M-GITM's original profile by 10-15 K, bringing it closer to the observed temperatures, particularly above $\sim$180 km. At these higher altitudes, approaching the exobase, the M-GITM temperature profile now matches the temperature profile derived from NGIMS densities. Comparing examples of NGIMS wind campaigns to the new M-GITM simulation produces mixed results. Again, the net effect of slowing down wind velocities is observed, which in one case improves the data-model comparison, and in the other does not. Thus, while improvements are found in some aspects of data-model comparisons, there are others where still-large differences suggest other physical processes not included in M-GITM may play an important role in driving the observed behavior of the thermospheric winds in certain situations.

Data-model comparisons such as these illustrate that while adding a parameterized GW scheme to M-GITM has made model output more realistic under some conditions, work still needs to be done to better understand the influence of small-scale GW effects at specific local times and latitudes. In general, it is challenging to validate modeled gravity wave activity with respect to observations, since there are a number of different gravity wave retrieval techniques and they can yield different results depending on how the background fields are determined [*Sakib and Yiğit*, 2022]. One of the challenges that remains in using a GW parameterization scheme is that the source GW spectrum is still not well known at Mars, but is likely more complex than the Gaussian used here and may be time-varying. Recent analyses of Mars Climate Sounder observations have been done to better understand and characterize the GWs observed in the lower atmosphere, including orographic and non-orographic contributions [e.g. *Heavens et al.*, 2020, 2022]. Analyses such as those, especially in combination with results from high-resolution GCM simulations [e.g. *Kuroda et al.*, 2016] might be able to be applied in the future to better refine the source flux formulation used in GW parameterization schemes. The scheme used in this analysis is specifically for non-orographic waves; however zero phase-speed waves can be included provided that their momentum fluxes are known. Nevertheless, orographic gravity waves are unlikely to affect the conclusions of the presented simulations, since they are much more susceptible to dissipation and saturate at lower altitudes in the atmosphere. Finally, while GW effects are seen to vary in the thermosphere in our results according to season, smaller-scale temporal variability in GW behavior and properties from the source level through the upper atmosphere could occur as a result of large-scale dust storm impacts [e.g. *Yiğit et al.*, 2021b; *Kuroda et al.*, 2020].

Despite the challenges present in including the effects of subgrid GWs into a GCM such as M-GITM, this study demonstrates that these small-scale waves have an appreciable impact on the mean upper atmospheric state, as seen by significant GW momentum deposition at thermospheric altitudes, along with corresponding changes to the neutral velocities and temperature structure in

the thermosphere. Since this coupling of the lower and upper atmosphere is important to address at Mars, and small-scale GW effects contribute significantly to this coupling, the inclusion of subgrid GW effects in GCMs should become a standard practice in future modeling applications.

3.9 Acknowledgments and Data Availability Statement

This work was supported by NASA Headquarters under the NASA Earth and Space Science Fellowship Program - Grant 80NSSC18K1238. Funding was also provided by the MAVEN project, Grant NNH10CC04C. Additionally, the material is based upon work supported by NASA under award number 80GSFC21M0002. The MAVEN/NGIMS densities and neutral wind datasets used in this study are available on the Planetary Data System (http://pds-atmospheres.nmsu.edu/data_and_services/atmospheres_data/MAVEN/ngims.html). The wind measurements are an NGIMS Level 3, Version 3, Release 1 data product and the neutral densities are an NGIMS Level 2, Version 8, Revision 1 data product. In addition, solar fluxes used in M-GITM simulations are from the MAVEN/EUVM FISM-M empirical model and are a Level 3, Version 14, Revision 3 data product on the Planetary Data System (https://doi.org/10.17189/1517691). M-GITM output from simulations used in this study can be found at the University of Michigan Deep Blue repository (doi.org/10.7302/7hab-2340).

CHAPTER 4

MAVEN/NGIMS Wind Observations in the Martian Thermosphere During the 2018 Planet Encircling Dust Event

The content in this chapter was originally published in 2022 in *Icarus*, under the same title, by K. J. Roeten, S. W. Bougher, M. Benna, and M. K. Elrod. *Roeten et al.* [2022a] is presented here with modified formatting.

4.1 Abstract

During the 2018 planet encircling dust event (PEDE) at Mars, the Mars Atmosphere and Volatile Evolution (MAVEN) spacecraft's Neutral Gas and Ion Mass Spectrometer (NGIMS) was able to take a series of neutral wind observations in the thermosphere at around 150–220 km altitude. These MAVEN observations are the first in-situ measurements of thermospheric wind velocities during a Mars global dust storm. From these measurements, it was found that the observed averaged horizontal thermospheric wind speeds peaked to nearly 200 m/s during the onset of the dust storm before decreasing to about 140 m/s near the peak of the storm. The maximum averaged wind speed observed during the dust storm is not significantly greater than averaged wind speeds at other times, but does represent a local maximum that coincides with the timing of the dust storm. Additionally, throughout the mature and early decay stage of the PEDE, NGIMS wind observations show increased short-scale variability that distinguishes this time period from most other observational periods.

4.2 Plain Language Summary

Starting in June 2018, a large dust storm at Mars grew to encircle the entire planet, and then slowly decayed over several months. This planet encircling dust event (PEDE) was observed by the Mars

Atmosphere and Volatile Evolution (MAVEN) spacecraft, which is currently in orbit around Mars. During the time period over the course of the PEDE, MAVEN was able to take observations of winds in the upper atmosphere of Mars. This is the first time upper atmospheric winds have been directly measured at Mars during a planet encircling dust storm. Averaged wind speeds were found to increase slightly during the start of the dust storm, up to around 200 m/s. In addition, starting at the peak of the PEDE and lasting through the early decay of the storm, the upper atmospheric winds were observed to become highly variable.

4.3 Introduction

Starting in early June 2018, a planet encircling dust event (PEDE) at Mars spread across the planet. Observations from multiple spacecraft have revealed significant changes throughout the entire Martian atmosphere at this time associated with the global-scale dust storm. In particular, this event has provided opportunity for new insight on the impacts of planet encircling dust storms on the upper atmosphere of Mars.

The onset of the storm that would develop into the PEDE began around 30 May 2018 (Ls=184.4), as seen by Mars Reconnaissance Orbiter (MRO)/Mars Color Imager [*Cantor and Malin*, 2018]. The Mars Climate Sounder (MCS) had detected evidence of the storm's influence in the zonal mean 50 Pa temperatures ($\sim$25 km) by 3 June (Ls=186.7) [*Kass et al.*, 2020], and the first evidence of an impact by the storm on the upper atmosphere was seen around 8 June (Ls=189.2) by the Mars Atmosphere and Volatile Evolution (MAVEN) mission [*Elrod et al.*, 2020]. By 17 June (Ls=194.9), the storm became planet encircling. The PEDE peaked around 7-10 July (Ls=207-208), as determined by zonally averaged temperatures observed by MRO/MCS in the middle atmosphere [*Kass et al.*, 2020]. This corresponds to a period where the dust was widespread and optical depth nearly uniformly high. The PEDE remained in a mature stage for nearly a month, until 18 July (Ls=213.3), after which the PEDE began to enter into an early decay stage during which middle atmospheric temperatures and dust column opacities started to decrease. The decay of the storm and return to seasonal conditions occurred gradually, lasting through mid-September or longer [*Kass et al.*, 2020]. More details on the development and evolution of the PEDE over time are provided in *Kass et al.* [2020] and *Sánchez-Lavega et al.* [2019], among others.

As the dust storm was becoming large scale, changes in upper atmospheric densities and temperatures were seen. Observations from the MAVEN/NGIMS (Neutral Gas and Ion Mass Spectrometer) instrument indicated increased thermospheric CO_2 densities at the peak of the storm at 170 km, though not all species measured by NGIMS followed this trend [*Elrod et al.*, 2020]. Similarly, an analysis of both NGIMS and Mars Orbiter Mission (MOM)/Mars Exospheric Neutral Composition Analyzer (MENCA) observations found neutral densities in the 150-220 km altitude range

increased by a factor of 2-3 [*Venkateswara Rao et al.*, 2020]. The effects of atmospheric expansion during the 2018 PEDE were also identified in MAVEN/IUVS (Imaging Ultraviolet Spectrograph) observations of an increase in the altitude of the absorption layer of the Lyman-alpha emission by CO_2 near the peak of the storm [*Chaufray et al.*, 2020] as well as through observations of the increased altitude of oxygen dayglow emission peak starting as the dust storm was becoming large-scale [*Gkouvelis et al.*, 2020]. In addition, an analysis of IUVS data suggested that thermospheric warming occurred during the PEDE, with an increase of $\sim$20 K during late afternoon after the onset of the PEDE [*Jain et al.*, 2020]. Furthermore, in the thermosphere, density perturbations driven by gravity waves seen in the NGIMS data were also observed to increase during the peak of the PEDE [*Yiğit et al.*, 2021b].

With changing background atmospheric conditions in the Martian thermosphere in response to the 2018 PEDE, it might also be expected that thermospheric winds would be impacted as well. Direct observations of winds in the upper atmosphere of Mars have not been possible for previous global dust storms. One of the few measurements of upper atmospheric winds available prior to 2016, zonal wind speeds derived from Mars Global Surveyor (MGS) accelerometer and rate data were reported for a regional dust storm in 1997 and found to increase by $\sim$200 m/s above the average value prior to the storm [*Baird et al.*, 2007].

Starting in 2016, the MAVEN spacecraft has provided the unique and novel ability to measure neutral thermospheric horizontal velocities in-situ using the NGIMS instrument [*Benna et al.*, 2019]. While some knowledge of the Martian global circulation pattern and its variability has been able to be inferred through observations from other orbiting spacecraft such as through temperature observations of the middle and lower atmosphere [e.g. *Heavens et al.*, 2011b] as well as from nightglow observations in the middle to upper atmosphere [e.g. *Schneider et al.*, 2020], MAVEN/NGIMS observations are the first in-situ thermospheric wind velocity measurements [*Benna et al.*, 2019]. The MAVEN/NGIMS thermospheric wind observations thus provide a new way to examine the potential impacts of the 2018 PEDE in the Martian upper atmosphere. In this analysis, the MAVEN thermospheric wind measurements taken during the 2018 PEDE are examined in terms of campaign-averaged wind speed and orbit-to-orbit variability and how these evolve over the duration of the storm.

4.4 Method

The wind velocities in the upper atmosphere of Mars are measured in-situ by the NGIMS instrument onboard MAVEN. NGIMS is a quadrupole mass spectrometer with the primary purpose of characterizing the neutral and ion composition of the Martian upper atmosphere [*Mahaffy et al.*, 2015b, a]. However, a new technique was developed in 2016 which allows the instrument to be

used to measure horizontal wind velocities at the location of the spacecraft as it passes through the thermosphere during the periapsis segment of its orbit [*Benna et al.*, 2019].

Key to this technique is that NGIMS sits on an articulated payload platform (APP) on the spacecraft, which allows the instrument's boresight direction to be adjusted. During wind measurements, the APP is rapidly nodded off of ram direction by $\pm$ 8° in the local horizontal plane. Cross-track and along-track wind velocities are then determined through the modulations in the observed CO_2 abundance using knowledge of the spacecraft trajectory and pointing information. The measurement technique is described in detail in *Benna et al.* [2019]. With this method, along-track and cross-track wind velocities can be observed along MAVEN's trajectory over altitudes of $\sim$140 up to $\sim$230 km with a measurement frequency of 0.03 Hz (about 30 s) [*Benna et al.*, 2019]. These along-track and cross-track velocities are then transformed to a Mars-fixed reference frame from the NGIMS-fixed reference frame such that velocities can be expressed in terms of a zonal and meridional component. This dataset of neutral thermospheric zonal and meridional wind velocities is a NGIMS Level 3, v03r01 data product.

The decomposition of the wind velocity into cross- and along-track components assumes the upper atmosphere is in hydrostatic equilibrium, such that the vertical component of the neutral wind velocity can be neglected [*Benna et al.*, 2019]. For nominal driving conditions, this assumption is considered appropriate for the Mars thermosphere [*Bougher et al.*, 2015c]. Typical uncertainty is 6 m/s for the cross-track wind velocity and 20 m/s for the along-track velocity. Uncertainty is largely due to inherent errors in the reconstructed ephemeris of the spacecraft and APP pointing, the energy resolution of NGIMS's mass filter, and counting statistics. Uncertainties in the reconstructed speed of the spacecraft are on the order of magnitude of cm/s and are negligible compared to other sources of uncertainty [*Benna et al.*, 2019]. Additional uncertainty could occur if the wind changes on time scales shorter than the $\sim$30 s it takes for the APP to complete one motion cycle. However, when the modulation in the data seen by NGIMS was compared to the expected response of the data when constant winds over the 30 s interval are assumed, good fits to the expected modulation were regularly seen, indicating that no appreciable additional uncertainty was added due to wind variability over the scale of seconds [*Roeten et al.*, 2019].

Wind observations are done in campaigns occurring roughly once every month; however, during the 2018 PEDE, more observational periods were added in order to capture any potential changes in the winds during the storm. The wind observational campaigns that occurred around this time period are listed in Table 4.1. Most observational campaign periods span two to three days, with five to ten consecutive orbits of wind measurements. Each of these orbits in a campaign traverses approximately the same region in local time and latitude, but precesses over different longitudes [*Benna et al.*, 2019].

In this work, campaign average wind speeds are reported. Campaign averages are simply the

Table 4.1: NGIMS Wind Campaigns Occurring Near the PEDE

Date (in 2018)	Orbits	Alt (km)[a]	LT (hr)[b]	Lat (deg)[c]	Ls (deg)[d]	Avg Speed (m/s)[e]	Avg CV[f]
12 April	6871 – 6875	157 – 211	13 – 15	44°S – 70°S	158	204 ± 66	0.30
16 – 17 May	7061 – 7065	158 – 205	10 – 11	19°S – 49°S	176	176 ± 76	0.53
9 – 10 June	7191 – 7195	162 – 216	7 – 8	2°S – 34°S	190	197 ± 94	0.84
22 – 23 June	7261 – 7265	160 – 219	6 – 7	7°N – 25°S	198	190 ± 96	0.56
30 June – 1 July	7301 – 7305	163 – 207	5.5 – 6	10°N – 18°S	202	172 ± 90	0.62
11 – 12 July	7359 – 7368	159 – 199	4 – 5	19°N – 8°S	209	141 ± 76	1.55
15 – 16 Aug	7548 – 7557	153 – 194	1 – 1.5	46°N – 18°N	231	170 ± 70	0.98
12 – 13 Sept	7701 – 7710	150 – 188	21 – 22.5	67°N – 40°N	248	142 ± 75	0.83
24 – 25 Oct	7934 – 7938	152 – 198	10 – 16	65°N – 75°N	275	201 ± 87	0.42

[a]Altitude range of campaign measurements
[b]Local time range
[c]Latitude range
[d]Approximate solar longitude
[e]Averaged speed with one standard deviation in speed
[f]Averaged coefficient of variation - a dimensionless scalar quantity with larger values corresponding to greater orbit-to-orbit variability

mean speed calculated using each individual wind observation from all orbits in a campaign. With 5–10 orbits in a campaign, this means there are roughly 60–120 total measurements averaged for each campaign. Campaign averaged speeds for campaigns during the time period near the PEDE can be seen in Table 4.1. Since, at the phase of the mission where these measurements were obtained, MAVEN traversed a full 360° in longitude in about five orbits [*Jakosky et al.*, 2015], campaign averages act as a method of longitudinal averaging. This allows for potential longitudinal variability in the winds to be smoothed to some degree (see also *Roeten et al.* [2019]).

Note that an upper altitude limit of 220 km was imposed on the NGIMS data for this analysis, though only a few orbits in this entire wind dataset have observations above this altitude. This was done so that averaging was done over a more consistent range of altitudes for each campaign, since most of the measurements were taken within the nominal altitude range of ∼150–220 km.

Variability of the winds during a campaign is analyzed using the standard deviation of speed as well as through the coefficient of variation, a dimensionless scalar quantity that serves as a measure of the orbit-to-orbit variability of the winds related to both speed and direction. The multivariate version of the coefficient of variation calculated here was determined from zonal and meridional components of the wind observations using the formulation from *Albert and Zhang* [2010]:

$$CV = \left[\mu^{\mathrm{T}}\Sigma\mu/(\mu^{\mathrm{T}}\mu)^2\right]^{1/2} \tag{4.1}$$

where μ is the mean and Σ is the variance-covariance matrix of the zonal and meridional components. A larger coefficient of variation can correspond to large variability in either direction or speed, or variability in both. A coefficient of variation value of zero indicates the absence of orbit-to-orbit variability, while the higher the value, the more variability is present. This formulation is the same one used to describe orbit-to-orbit thermospheric wind variability in *Roeten et al.* [2019] and *Benna et al.* [2019].

In order to calculate the coefficient of variation, an averaged velocity profile for each campaign had to be calculated first. Data is taken from all orbits in a campaign and then is grouped according to sampling point location in latitude, local time, and altitude along MAVEN's trajectory (not combining the inbound and outbound segments of the orbit). Then an average value was found at each sampling location. Since a relatively small number of wind measurements can be taken every periapsis pass, typically one observation from each orbit was in a group. This produces a mean velocity profile along MAVEN's trajectory. Averaged velocity profiles for each campaign listed in Table 4.1 are shown as velocity vectors along MAVEN's trajectory in latitude and local time in Figure 4.1. The coefficient of variation is indicated by the color of the vectors, with redder colors indicating higher orbit-to-orbit variability. Another example showing these averaged velocity vectors along the spacecraft track can be seen in the Results section in Figure 4.3, which are plotted along with all the individual measurements from those campaigns. The campaign

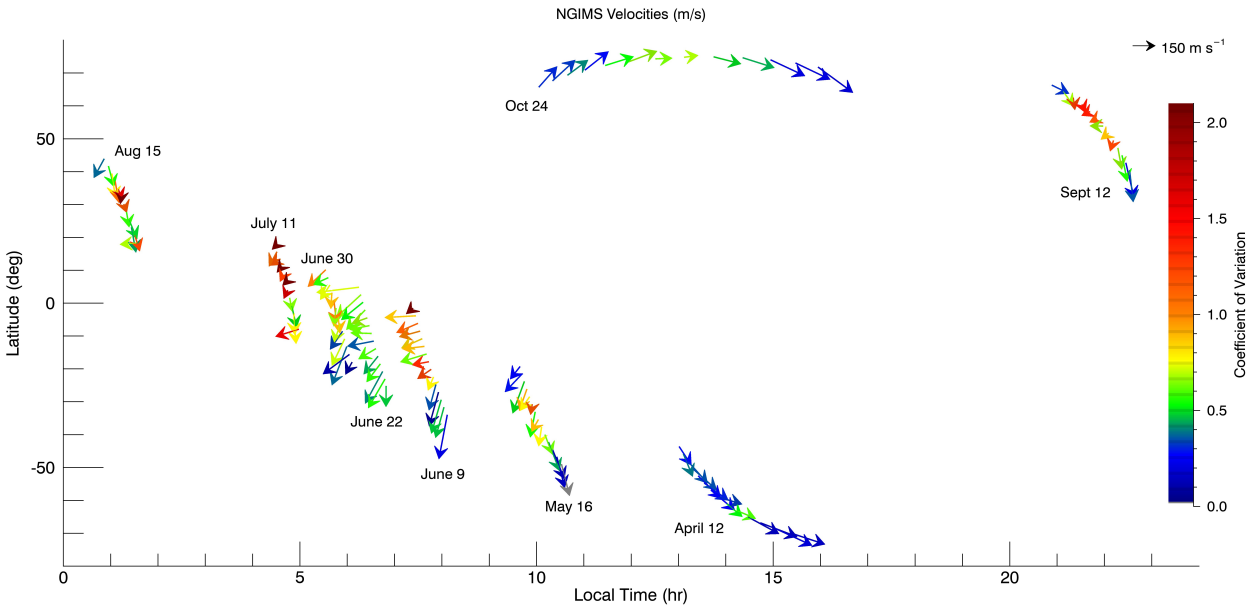

Figure 4.1: Latitude-local time map of vectors showing the averaged velocity profiles along the spacecraft track for the NGIMS wind observational campaigns listed in Table 4.1. Vector length corresponds to speed, and the direction the vector points to indicates the horizontal direction towards which the winds are directed (with northward flow indicated by an upward directed arrow and westward flow indicated by an arrow pointed to the left). Color corresponds to the coefficient of variation, with redder colors indicating higher orbit-to-orbit variability. The dates annotated on the plot are the first day of each observational campaign.

averaged coefficient of variation which is listed in Table 4.1 is the mean of the values of coefficient of variation found at each sampling point location along the trajectory.

4.5 Results

During the time period of the storm, from its onset to the beginning of the early decay phase (late May through about September), the fastest campaign-averaged wind speed observed was $\sim$200 m/s (see Figure 4.2). This maximum average speed was from the 9–10 June campaign, which occurred after the onset of the storm, but before the storm became planet encircling. As seen in Figure 4.2, averaged speeds gradually decrease after the 9–10 June campaign and reach a local minimum of $\sim$140 m/s during the 11–12 July campaign (right after the peak of the PEDE near 7–10 July) before slightly increasing again in the next campaign.

Note, however, that the campaign-averaged wind speeds observed by NGIMS during the PEDE are not notably different in magnitude than observed in other periods prior to or after the PEDE. As can be seen in the top plot in Figure 4.2, despite being somewhat elevated, the campaign-averaged

wind speed in the 9–10 June campaign does not differ greatly from that in the 24–25 October campaign (after the main decay of the PEDE) or the 12 April campaign (prior to the PEDE), both of which also had campaign-averaged speeds of ∼200 m/s. In fact, the 7–9 February campaign saw averaged wind speeds reach 240 m/s. Thus, while the timing of the maximum in speeds during the PEDE suggests it is related to the PEDE, the magnitude is not notably different than periods prior to or after the storm.

To further verify this, a two-sample student t-test was conducted on the 9–10 June campaign and both the 16–17 May campaign and the 12 April campaign, the two campaigns that occurred just prior to the onset of the PEDE. In both of these cases, the null hypothesis was that the campaign-averaged speeds were the same, with unknown variances and at the 5% significance level. Indeed, at this significance level, the null hypothesis could not be rejected for either set of campaigns, further indicating the speeds observed by MAVEN during the PEDE, while slightly elevated, do not differ significantly from those observed in the months prior to the onset of the PEDE.

In contrast to the slight but perhaps not significant increase in campaign-averaged wind speed during the PEDE, the variability in the thermospheric wind was observed to increase substantially. As measured by the campaign-averaged coefficient of variation, orbit-to-orbit variability in wind velocities increases during the PEDE compared to the time periods immediately before and afterward, as can be seen in the lower plot in Figure 4.2 (as well as in Figure 4.1). The 11–12 July campaign has the greatest averaged coefficient of variation of the campaigns during the PEDE, with a value over 50% larger than that for campaigns at similar Ls before and after the PEDE. Though still elevated throughout this stage of the PEDE, the coefficient of variation decreases gradually over the next few campaigns, indicating less orbit-to-orbit variability after the 11–12 July 2018 campaign. By the October 2018 campaign, notably less variability is observed as the average coefficient of variation has decreased to the lowest value calculated within that season.

Figure 4.3 shows all individual horizontal velocity measurements (gray vectors) along with average velocities (colored vectors) during three NGIMS wind campaigns: 11–12 July 2018 (close after the peak of the PEDE), 15–16 August 2018, and 24–25 October 2018 (late in storm decay). The October campaign shows winds that flow consistently from orbit-to-orbit, with individual measurements having similar speeds and directions. The July campaign, and to a slightly lesser extent, the August campaign show a much different sort of behavior, with both wind direction and speed seeming to change from orbit to orbit, as well as from one observation to another along the same orbit. This characteristic of a steady flow during the October campaign in respect to its orbit-to-orbit variability is similar to what was seen in the April 2018 campaign, which occurred prior to the dust storm (see Figure 4.1).

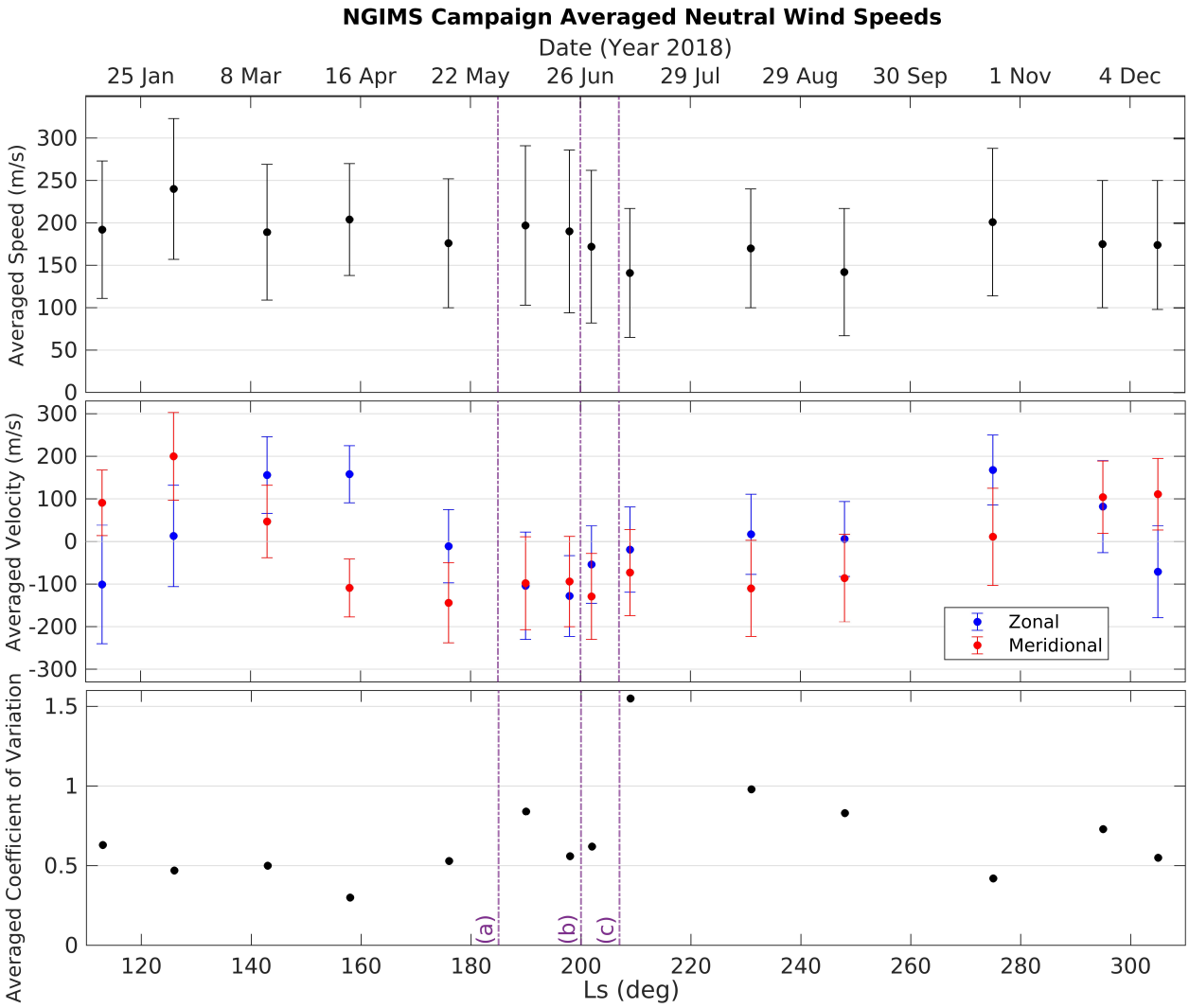

Figure 4.2: On the top plot, campaign-averaged speed is plotted vs solar longitude (Ls). Vertical bars show the 1 σ of speed for each campaign. The middle plot shows the campaign-averaged zonal (blue) and meridional (red) components of the observed velocities. The lower plot shows the campaign-averaged coefficient of variation vs Ls. Purple vertical dashed lines from left to right indicate important times during the development of the PEDE: (a) the onset of the storm, (b) the time at which MAVEN periapsis moved to the nightside, and (c) the peak of the PEDE.

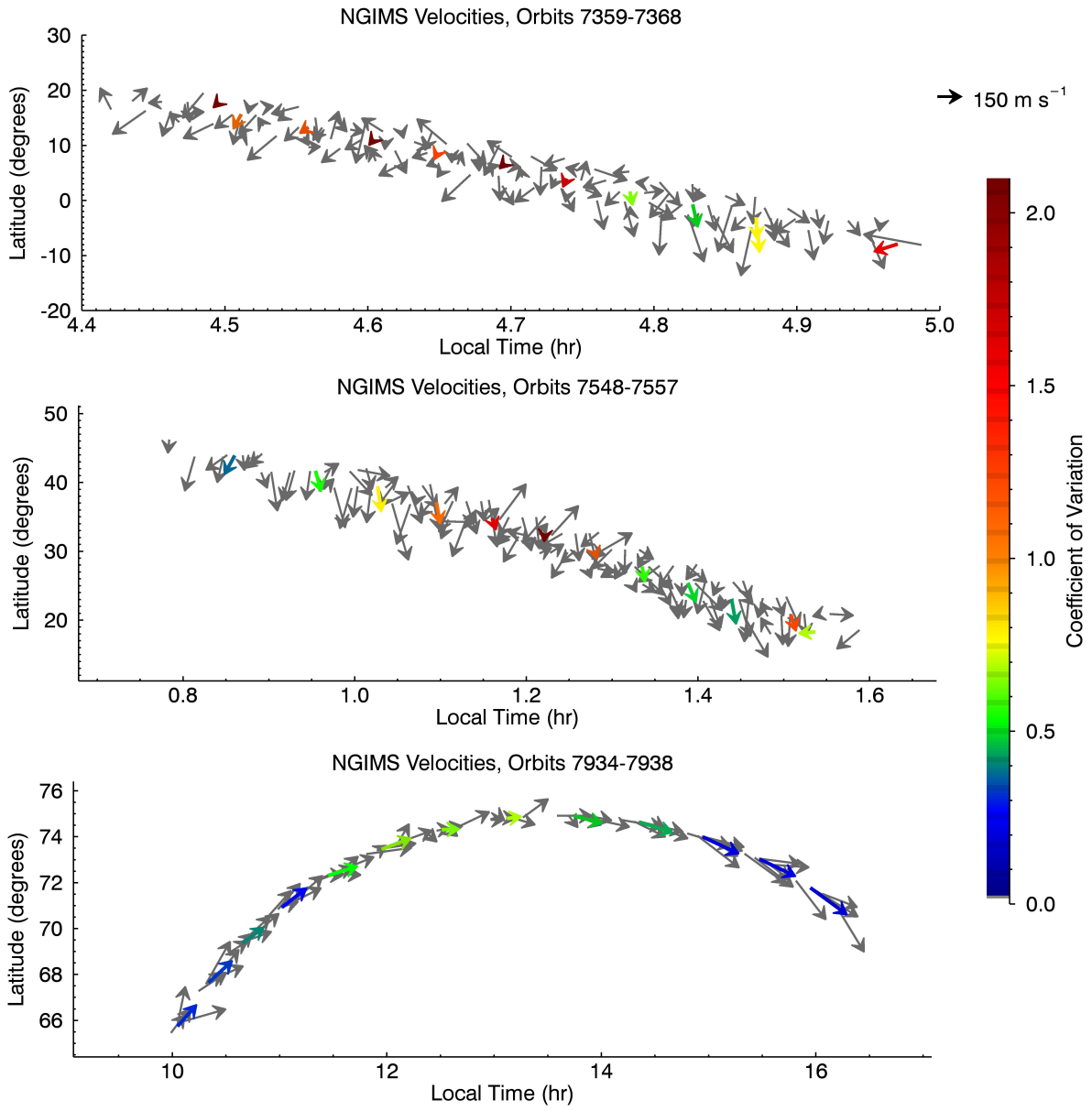

Figure 4.3: Wind measurements taken by NGIMS during the 11–12 July 2018 (top), 15–16 August 2018 (middle), and 24–25 October 2018 (bottom) campaigns in local time and latitude. Vector length corresponds to speed, and the direction the vector points to indicates the horizontal direction towards which the winds are directed (with northward flow indicated by an upward directed arrow and westward flow indicated by an arrow pointed to the left). Gray vectors show each individual wind velocity measurement. Colored vectors are averaged velocities along the spacecraft track, with colors corresponding to the coefficient of variation. Higher coefficient of variation values correspond to greater orbit-to-orbit variability.

4.6 Discussion

4.6.1 Potential Impacts of the PEDE on Thermospheric Wind Behavior

As was described in the previous section, variability in wind velocities, as determined by the campaign averaged coefficient of variation, was found to be at its greatest during the time period of the PEDE during the 11–12 July campaign, which occurred close after the peak of the storm, and then gradually diminished until after the 24–25 October campaign. This seems to indicate a substantial change in the amount of variability in the upper atmospheric winds from the development to decay phase of the storm, with the most variability found after the peak and into the early decay phase. The decrease in wind variability though the decay phase of the storm might be an additional indication that environmental conditions in the upper atmosphere are slowly returning back to the typical seasonal background. Specifically, the similarity in the behavior of the October campaign's wind velocities in respect to orbit-to-orbit variability and that of the April campaign (prior to the PEDE) might suggest that the flow in the upper atmosphere has largely returned to typical conditions for the season by this time, with minimal further influence of the PEDE on thermospheric winds. From MRO/MCS zonally averaged middle-atmospheric temperatures, *Kass et al.* [2020] roughly estimated that the PEDE may have lasted until late October, around Ls=270–280° (though the specific Ls is uncertain due to the instrument temporarily being turned off). This time frame generally agrees with that during which the variability in the thermospheric winds diminished.

It is possible that perturbations induced in the thermospheric densities during this time period by gravity waves (GWs) are connected to the variability observed in the NGIMS thermospheric wind velocities during the PEDE. An analysis by *Yiğit et al.* [2021b] of GW-related perturbations in CO_2 densities observed by NGIMS suggested that during the PEDE, GW activity nearly doubled in the thermosphere. The greatest orbit-to-orbit variability in NGIMS velocities observed during the PEDE was for the 11–12 July campaign, which is concurrent with the time of peak thermospheric GW activity as identified by *Yiğit et al.* [2021b]. Variability in velocities in campaigns after 11–12 July generally starts to decrease at the same time as GW activity was reported to begin to gradually diminish.

During the PEDE, the NGIMS wind campaign with the greatest orbit-to-orbit variability in velocities also occurred when the campaign-averaged wind speeds were the slowest. However, the trend over time for orbit-to-orbit variability in thermospheric velocities is different than the trend observed for changes in averaged speed only. Within the period of the dust storm, the campaign averaged speed has a local maximum right after storm onset (9–10 June), and then diminishes through the campaign right after the peak of the PEDE (11–12 July). The campaign averaged coefficient of variation is greatest right after the peak of the PEDE and then gradually decreases in the following campaigns. It might be noted that the 9–10 June campaign with the peak averaged

speed at the onset of the storm does not have the lowest average coefficient of variation, which might have been expected if orbit-to-orbit variability was the only process that drove average speed. It may also be notable that, if the slight increase in averaged wind speed during the 9–10 June campaign can be attributed to the 2018 PEDE, this local peak in speed occurred prior to the peak of the storm (as defined by *Kass et al.* [2020] around 7–10 July) or even before it become planet encircling (17 June).

4.6.2 Consideration of Potential Drivers of Wind Behavior Unrelated to the PEDE

The changing location of the NGIMS wind campaigns in latitude and local time (LT) during the PEDE must also be taken into account, which complicates the possible interpretation that the PEDE is the primary factor influencing the changes in the behavior thermospheric winds at this time. As can be seen in Table 4.1, periapsis location started at 6–7 LT for the first wind campaign that took place during the dust storm. Periapsis then precessed over the dawn terminator and onto the nightside through the peak and decay phases of the PEDE. Latitudes at periapsis also precess from low latitudes in the southern hemisphere to low-middle latitudes in the northern hemisphere. Simulations of the upper atmospheric circulation from the Mars Global Ionosphere-Thermosphere Model (M-GITM) have suggested that from midnight to dawn at low-mid latitudes, there is a broad zone of convergence in the thermospheric winds [*Bougher et al.*, 2015c]. In this convergence zone, thermospheric winds are generally expected to be more variable with, on average, slower speeds, though this is yet to be confirmed. Accelerometer data from MAVEN has also indicated increased variability in mass densities on the night side of the dawn and dusk terminators, and over the nightside in general [*Zurek et al.*, 2017]. Thus, part of the increased variability observed in the thermospheric velocities during the PEDE may be related to the precession of MAVEN's periapsis over the dawn terminator to the nightside.

Nonetheless, during the PEDE, calculated coefficient of variation values are larger than those in most other campaigns at times before or after the PEDE (including other campaigns within the same latitude-LT sector) and thus are likely in part associated with impacts from the dust storm. Campaign-averaged coefficient of variation values from March 2016 through December 2020 are plotted in Figure 4.4. The 11–12 July 2018 campaign has the fourth largest coefficient of variation value calculated for any of these campaigns. The three other campaigns outside of the time period associated with the PEDE which have greater averaged orbit-to-orbit variability do also occur on the nightside to near dawn in local time, but at different latitudes than the campaigns during the storm (the three campaigns with greater averaged orbit-to-orbit variability occur at -7°S to -35°S and 19–20 LT, 60°N to 74°N and 2–9 LT, and 30°N to 62°N and 22–24 LT). However, as can be

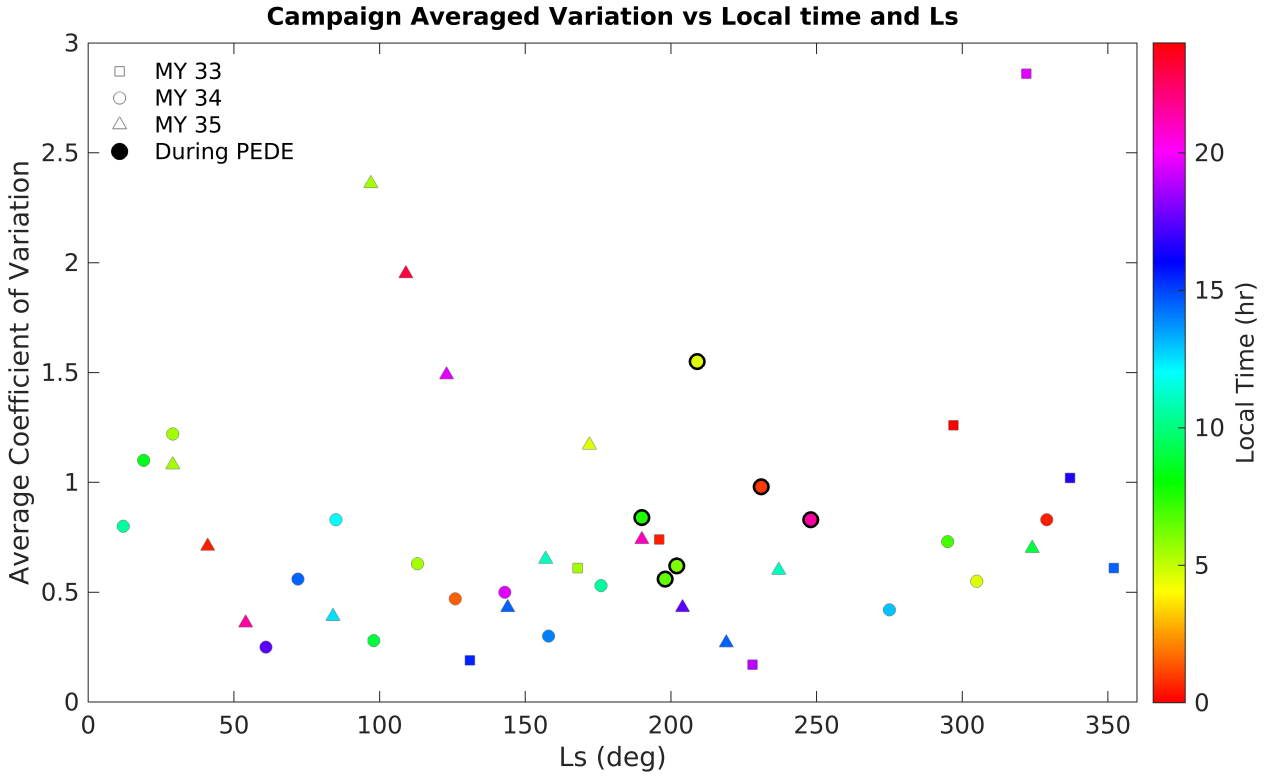

Figure 4.4: The averaged coefficient of variation for each campaign from the start of the NGIMS wind observations through December 2020. Higher coefficient of variation values correspond to greater orbit-to-orbit variability. Color corresponds to the mean local time of the observation. Different shaped symbols differentiate campaigns from Mars years (MY) 33, 34, and 35. The x-axis, solar longitude (Ls), indicates at what time in the Martian year the observation took place. Circles with a bold black edge indicate campaigns that occurred during the 2018 PEDE. Note that the greatest campaign-averaged coefficient of variation during the PEDE is the 11-12 July 2018 campaign at Ls$\sim$210 near the peak of the PEDE.

seen in this figure, not all campaigns that occur on the nightside have orbit-to-orbit variability to the extent seen in these campaigns.

The larger average coefficient of variation for just a few campaigns seen in Figure 4.4 suggests that while large orbit-to-orbit variability can occur during global-scale dust storms, these storms are not the only process to produce such variability. Of these few campaigns, only the campaign at Ls$\sim$320 was concurrent in timing with any large-scale dust activity (i.e., the onset of a regional dust storm, in this case). Future studies are needed to address what other processes could be driving greater orbit-to-orbit variability in Martian thermospheric winds.

Besides dust storms, another source that could drive large changes in the thermosphere, and potentially wind velocities at these altitudes as well, is large transient solar events. For instance, it was found that thermospheric densities and temperatures responded to an X class flare in 2017 [e.g.

Elrod et al., 2018; *Jain et al.*, 2018]. However, no flares or Mars-directed coronal mass ejections occurred during the NGIMS wind campaigns spanning the June through July 2018 time frame.

Another potential consideration for some of the campaigns during the PEDE is variability in thermospheric densities due to large orbit-to-orbit topographical variations, which is most likely to occur when MAVEN periapsis is at mid-latitudes.

4.6.3 Comparisons to Other Upper Atmospheric Wind Observations and Modeling Studies

Determining the relative importance of the impacts of the PEDE on the thermospheric winds remains challenging since the NGIMS observations are the only direct measurements of upper atmospheric winds during a global-scale dust storm at Mars. However, zonal upper atmospheric wind speeds were derived by *Baird et al.* [2007] from Mars Global Surveyor accelerometer and rate data during a regional dust storm at Mars in 1997. This study found that derived zonal winds increased near storm onset by ∼200 m/s above the average value, approaching 300 m/s at the 120–135 km altitude range. In contrast, the mean winds found using NGIMS measurements during the PEDE only reached ∼200 m/s. This was only 20 m/s higher than the campaign prior (before the dust storm began developing). It may be somewhat unexpected that wind speeds during the onset of the 2018 dust storm did not increase as much as observed during a regional storm. However, it is possible that the thermospheric wind speeds during the 2018 PEDE could have peaked to greater values between NGIMS observational wind campaigns for a short period, and decreased again by the time of the next observational period. Additionally, the NGIMS wind campaigns span somewhat higher thermospheric altitudes, from ∼150–220 km. Averaging may also be different. Furthermore, these storms occurred at different seasons (for *Baird et al.* [2007], Ls∼300, nearer to southern hemisphere summer solstice as opposed to close to equinox for the onset of the 2018 PEDE). Thus, there are many potential factors which might contribute to the apparent difference in response seen in the thermospheric wind during these two large-scale dust events.

While the NGIMS wind observations during the 2018 PEDE are significantly the first in-situ measurements of thermospheric winds during a Martian global dust storm, this dataset has a notable limitation of observations only occurring in relatively short-duration campaigns. More comprehensive and higher-cadence observations are needed to develop a more complete picture of how thermospheric winds are perturbed during a global dust storm at Mars, something that could be accomplished by a future Mars orbiter.

Though there is a lack of observational data on thermospheric winds during large Martian dust storms prior to MAVEN, several modeling studies have been done to examine the impact of the 2018 PEDE or previous equinoctial global dust storms on the global circulation pattern. These

studies have suggested that during such global dust storms, the general circulation and mean winds in the middle to upper atmosphere can undergo significant changes, even prior to the peak of the storm [e.g. *Medvedev et al.*, 2013; *Kuroda et al.*, 2020; *González-Galindo et al.*, 2015]. A few examples of these are mentioned in more detail below.

A modeling study from *Medvedev et al.* [2013] using the Max Planck Martian General Circulation Model simulated the MY 25 equinoctial global dust storm from the time of its onset to near the peak (approximately over the growth phase). Analyzing zonally averaged quantities, they found stronger zonal winds in the middle to upper atmosphere during the dust storm as well as indications of an enhanced northward transport near the mesopause and lower thermosphere (with the highest altitudes included in the analysis near $\sim$150 km, or 10^{-5} Pa), particularly in the north hemisphere. Like in other modeling studies, this was seen to be a result of the modification of the circulation during the storm from two meridional circulating cells to one dominant overturning cell, a behavior more typical of later in the season [*Medvedev et al.*, 2013]. Another modeling study by *González-Galindo et al.* [2015], using the Laboratoire de Météorologie Dynamique Mars General Circulation Model (LMD-MGCM) simulated the MY 25 equinoctial global dust storm and examined resulting zonally averaged fields from the dayside during the mature phase of the storm. They found that their model produced a reinforced westward jet in the mesosphere and thermosphere during the global dust storm, particularly in the north hemisphere. The zonal mean meridional winds were found to strengthen below $\sim$100 km ($\sim$0.01 Pa), but were dampened above that level through the model top (10^{-7} Pa, $\sim$200 km) at all latitudes [*González-Galindo et al.*, 2015].

Interestingly, most of these model results indicate an intensification of at least one component of the middle-upper atmosphere winds, which seems in apparent contrast to the slower NGIMS campaign-averaged speeds seen near the peak of the 2018 PEDE in this study. Since one might expect at least some influence by the mean winds to be observable in these campaign-averaged values, it in turn might be expected that campaign averaged wind speeds should increase during the dust storm, rather than decrease as is observed after the local maximum in speed following storm onset. Even in the separate zonal and meridional components, as seen in the middle plot of Figure 4.2, this does not seem to be the case. The averaged meridional component stays relatively steady near -100 m/s from the early June campaign through the September campaign; no clear trend emerges. The zonal component begins to decrease after the early July campaign, switching sign and becoming westerly through the long decay phase of the dust storm. However, this latter behavior can likely more so be associated with the change in latitude and local time of MAVEN's track through the thermosphere as it makes these in-situ wind measurements.

One important factor to discuss in comparing results from these NGIMS observations with previous modeling studies is the altitudes over which the NGIMS observations were taken, at

roughly 150–220 km. While the results from *Medvedev et al.* [2013] suggest enhanced zonal winds and intensified northward transport in the mesosphere and lower thermosphere, the top of the altitude range discussed approaches 150 km. As such, it is uncertain whether their findings would also be expected to hold true at altitudes much higher than this level, and as a result, might not be ideal to compare to the NGIMS wind campaigns, which begin at altitudes of 150 km or above. The LMD-MGCM from *González-Galindo et al.* [2015] extends to higher altitudes, however, and they find that while mean zonal winds increase at all altitudes in the middle-upper atmosphere during the MY 25 storm, the mean meridional flow was slower above a certain pressure level, roughly 100 km. Noting that the *González-Galindo et al.* [2015] study has run their GCM over the mature phase of the MY 25 storm, this corresponds to the period near the peak of the 2018 PEDE, during which NGIMS observes relatively slower averaged wind speeds. This might agree with the idea of a damped meridional circulation at these altitudes. However, a significant caveat is that the *González-Galindo et al.* [2015] study looked exclusively at LT=12, or local noon. By the time of the peak of the 2018 PEDE, NGIMS periapsis had transitioned over to the nightside, where different flow characteristics might be expected. Indeed, this suggests that future Mars GCM modeling studies might be required for the 2018 PEDE event which extend to the exobase and specifically look at both dayside and nightside in order to have a closer comparison to the NGIMS wind dataset.

4.7 Conclusions

During the time period of the 2018 planet encircling dust event (PEDE), the NGIMS instrument onboard MAVEN completed several observational campaigns to measure neutral thermospheric wind velocities. During this period, a slight (but not statistically significant) increase of campaign-averaged wind speeds was observed coinciding with the time period after the onset of the storm, but prior to it becoming planet encircling. The campaign-averaged speeds reached $\sim$200 m/s at this time. Over the next four wind campaigns (during which time the PEDE reached its peak and began to gradually decay), averaged wind speeds began to decrease to $\sim$140 m/s before rebounding slightly. In addition, the average orbit-to-orbit variability in the thermospheric wind velocities was observed to increase during the time period concurrent with the mature stage of the PEDE. The variability increased shortly after the peak of the PEDE to an extent greater than observed in most other wind observational campaigns prior to and shortly after the PEDE. Orbit-to-orbit variability remained elevated through the early decay phase before the flow became more coherent again late in the decay phase, perhaps indicating a return to typical seasonal conditions by this time. During the PEDE, the thermospheric winds seem to become most variable from orbit-to-orbit and the campaign-averaged speed reaches a minimum value very close to the time of the

peak of the storm. It remains important, however, to note that it is possible that the interpretation that the observed changes in the averaged wind speed and orbit-to-orbit variability are a response to the PEDE is complicated by the changing location of the MAVEN periapsis as it passes over the dawn terminator to the nightside. Future modeling studies and additional thermospheric wind observations will be important to investigate and further understand the separate influences of location, season, and evolving global dust storm effects upon the thermospheric winds.

4.8 Acknowledgments and Data Availability Statement

This work was supported by NASA Headquarters under the NASA Earth and Space Science Fellowship Program - Grant 80NSSC18K1238 (K.J. Roeten). Funding was also provided by the MAVEN project, Grant NNH10CC04C (S.W. Bougher). Additionally, the material is based upon work supported by NASA under award number 80GSFC21M0002 (M. Benna, M.K. Elrod). The NGIMS dataset used in this study is available on the Planetary Data System (http://pds-atmospheres.nmsu.edu/data_and_services/atmospheres_data/MAVEN/ngims.html).

CHAPTER 5

Conclusions

The work in this thesis has provided an analysis of the behavior of the neutral winds in the thermosphere of Mars, including through an examination of how this behavior may be impacted through coupling with the lower atmosphere. Using a 3-D ground-to-exobase Mars GCM called M-GITM and new MAVEN/NGIMS thermospheric neutral wind observations, the effects of gravity waves propagating up from the lower atmosphere as well as the impacts of the most recent global dust storm were examined. Results highlighting the potential response to these drivers indicate the importance of better understanding this coupling with the lower atmosphere. In Chapter 1, three key research questions were proposed, and addressed in each of the three following chapters.

5.1 Summary of the First Study: Initial Data-Model Comparison of Thermospheric Winds

How well do simulations from a general circulation model that is primarily driven by solar forcing at thermospheric altitudes compare to the MAVEN/NGIMS neutral wind observations?

Measurements from five NGIMS neutral wind observational campaigns were compared to simulations of the Martian thermosphere from M-GITM. Velocities in some of these campaigns were able to be replicated to some degree by M-GITM simulations, either in speed, direction, or both. In campaigns such as those from September 2016 and February 2018, M-GITM produced a flow direction which matched that suggested by the observations, while underpredicting averaged speeds by up to 150 m/s. Other campaigns, such as the May 2017 campaign and the January 2017 campaign, saw large disparities in the comparison in both speed and direction. Since M-GITM is primarily driven by solar EUV forcing at these altitudes, these data-model comparisons indicate the relative importance of solar forcing in driving the winds under the different seasonal, local time, and latitude conditions during these different campaigns. In campaigns with better data-model comparisons, solar forcing appears to be the primary influence on the winds, but in the cases of

poor comparisons, processes not yet included in the model seem to be more or equally important as the nominal solar forcing.

5.2 Summary of the Second Study: Modeling the Effects of Gravity Waves in the Thermosphere

How do the mean thermospheric winds and temperature structure respond to the effects of gravity waves which propagate up from the lower atmosphere?

A modern whole-atmosphere, nonlinear, non-orographic gravity wave parameterization scheme which includes both momentum deposition and thermal effects of GWs [*Yiğit et al.*, 2008] has been incorporated into the M-GITM model. A series of sensitivity tests show the scheme is robust within the model, demonstrated by the relatively small changes that result when key parameters are changed compared to the notable differences that result from the addition of the scheme itself into M-GITM. In both equinox and solstice simulations, significant momentum deposition was found to occur at altitudes ranging from ∼90-170 km. Temporally and zonally averaged GW drag on the order of magnitudes of several hundreds of meters per second per sol up to over 1000 m/s/sol is found at these altitudes. This agrees reasonably well with simulations in the lower thermosphere from *Medvedev et al.* [2011b]. GW effects produce notable modifications to the thermospheric winds and temperature structure in these new M-GITM simulations. Mean thermospheric winds, in general, slow significantly. Especially at middle latitudes in the southern summer hemisphere, wind speeds can be reduced by up to a factor of two. Additionally, mean temperatures in the thermosphere above ∼120 km are cooler when GW effects are included in the model, which also acts to improve a dayside data-model comparison with the NGIMS derived DD2 temperature profile. Data-model comparisons with some of the wind campaigns originally examined in Chapter 2 resulted in an improvement in the averaged representation of velocities in the January 2017 campaign, but little to no improvement in the May 2017 campaign. Overall, the effects of GWs propagating from the lower atmosphere are found to be capable of generating a significant thermal and dynamical impact in the upper atmosphere, and need to be represented in all Mars GCMs which extend to the upper atmosphere.

5.3 Summary of the Third Study: Thermospheric Wind Behavior During the 2018 Global Dust Storm

Do winds in the thermosphere respond to global dust storms at Mars?

NGIMS thermospheric wind observations were examined during the time period of the 2018 Mars global dust storm to determine whether there was any change in behavior that could be attributed to the storm. The campaign-averaged wind speed was found to increase slightly (but not significantly, in a statistical sense) to nearly $\sim$200 m/s during the time period near the onset of the storm. Averaged speeds then gradually decreased through the mature stage of the storm. However, substantial orbit-to-orbit variability was seen during the mature and into the decay stage of the storm, especially near in time to the peak of the storm. It is possible that the reduction of variability in thermospheric velocities could serve as an indicator of when the upper atmospheric response to the dust storm has minimized during the long decay. The changing latitude-local time location of the NGIMS observations (especially the shift to the nightside of the planet) complicates the interpretation of the role of the dust storm in the observed wind behavior, however, and also needs to be taken into consideration. Nonetheless, the timing, and in the case of orbit-to-orbit variability, the magnitude of some of these changes make it seem likely that at least part of the observed response is connected to the global dust storm.

5.4 New Questions and Future Research

Both the modeling studies presented here suggest that while thermospheric velocities (and temperatures) can be accurately replicated by M-GITM to some degree, there still seems to be physical processes not fully represented in the model, the relative importance of which may not be completely understood or appreciated. The second two studies in this thesis examine two ways in which the upper atmosphere is coupled to the lower atmosphere. These results demonstrate that impacts from the lower atmosphere, particularly that of gravity waves, should not be neglected by the Mars aeronomy community.

These studies also bring up further questions about thermospheric winds, their variability, and the processes that drive them. It was seen in Chapter 3 that even after the effects of GWs were included in M-GITM, there were still aspects of the neutral wind observations that M-GITM could not replicate. While the GW scheme does notably improve the modeled winds and temperatures in a general sense, there are too few observational constraints currently available at Mars to refine certain aspects of the scheme, such as the expected source flux and how it varies with latitude, local time, and season. Nonetheless, if future observations and data analysis were able to better quantify such characteristics of the GW spectrum, the GW scheme could be adjusted to account for this. In addition, a more complete treatment of other lower atmospheric physical processes within M-GITM could further improve data-model comparisons. This might be especially influential in regards to the GW scheme now employed within M-GITM, as calculations of the evolution of GWs within the scheme take into account the background winds throughout the simulated atmosphere.

It is likely that there are still other processes that shape thermospheric velocities which are not included in the model currently. For instance, the role of orographic GWs in the thermosphere is still somewhat unclear. Analysis of density datasets at thermospheric altitudes from MGS and Mars Odyssey aerobraking campaigns has suggested that the GWs that propagate up to the thermosphere do not follow the expected distribution pattern of what would be expected from waves which are launched off of the terrain [*Creasey et al.*, 2006]. However, analysis of NGIMS wind campaigns near low latitudes has indicated a residual downhill flow that could be propagated into the thermosphere through orographic GWs [*Benna et al.*, 2019]. Ideally, both an orographic GW scheme and a non-orographic GW scheme would be included in a GCM framework. Furthermore, while the studies presented in Chapter 3 and Chapter 4 primarily examine two examples of types of coupling with the lower atmosphere as processes that can have large potential impacts on the thermospheric winds, it is also possible ion drag could play a role, as it is known to do at Earth [e.g. *Schunk and Nagy*, 2009]. However, since Mars does not have a global magnetic field, but only smaller crustal fields, it might not be anticipated that this effect would be as large at Mars as it is at the poles of Earth.

Chapter 4 examines the potential impacts of the global dust storm on the thermospheric winds using data-analysis. A step forward for this analysis would be to compare these NGIMS wind observations during the global dust storm to a M-GITM simulation of the event. Data model comparisons have been conducted between an M-GITM simulation of the 2018 storm and MAVEN/IUVS temperatures [*Jain et al.*, 2020]; however, this analysis has not yet been extended to the NGIMS velocities. In this comparison of IUVS temperatures with M-GITM simulations, while the model was able to replicate observed temperatures before the dust storm and during the early part of the storm, it was not able to reproduce the temperature trend near the peak of the storm [*Jain et al.*, 2020]. These M-GITM simulations did include time-varying dust optical depths and vertical dust distributions obtained from MRO/MCS [i.e. *Kleinböhl et al.*, 2009], and thus used a more sophisticated representation of dust than was included in this body of work. They did not, however, include the effects of subgrid-scale GWs in the M-GITM simulations, as was done in Chapter 3. If the GW scheme were to be included in M-GITM simulations of the 2018 global dust storm, it is possible that the parameters used within the scheme (see Section 3.4.2) for the baseline case might not be the most appropriate choices for a dust storm case, though again, this is poorly constrained. There have been studies of the 2018 global dust storm, however, that did clearly indicate a change in the behavior of GW activity in the middle and upper atmosphere during the storm [*Leelavathi et al.*, 2020; *Yiğit et al.*, 2021b; *Kuroda et al.*, 2020]. High-resolution simulations from *Kuroda et al.* [2020] found that near the peak of the storm, while GW activity in the lower atmosphere decreases by a factor of two, GW energy and momentum fluxes found in the middle atmosphere doubled. The authors of that study suggested that even though the GW source flux might decrease during

this stage of the dust storm, changes in the large-scale circulation (the mean background winds) in the lower and middle atmosphere caused by the storm acted to facilitate vertical wave propagation, allowing more GWs to propagate to higher altitudes than typical [*Kuroda et al.*, 2020]. This idea seems to be further confirmed through analysis of NGIMS density data during the dust storm, which suggested that GW activity in the thermosphere ($\sim$160-225 km) doubled during the peak of the storm [*Yiğit et al.*, 2021b]. Thus, due to complicated feedbacks between radiative forcing, apparent modifications to the general circulation, and changing gravity wave generation and propagation, utilizing a GW parameterization scheme in a M-GITM simulation of the 2018 global dust storm event is a complex task, requiring dedicated future study.

Overall, while questions still remain, it is clear that our capability to study thermospheric winds has increased due to the novel NGIMS neutral wind dataset, but also through improvements to numerical tools, such as through the inclusion of a modern GW scheme into M-GITM. In order to continue improvements in this direction, ground-to-exobase GCMs are needed to further explore the importance of vertical coupling, especially through utilization of modern parameterization schemes for subgrid-scale physical processes like GW effects, which are a key part of the coupled Martian atmosphere. Furthermore, an increase in the number of available thermospheric wind datasets would help to better validate models and provide observations across a broader set of conditions, which would improve our understanding of interannual variability as well as seasonal and geographical variability. While the wind observational campaigns by NGIMS have provided a look into the Martian thermospheric winds like never before, these should ideally be augmented in the future by observations from a new Mars orbiter with an instrument dedicated to wind measurements in the middle and upper atmosphere.

BIBLIOGRAPHY

Albert, A., and L. Zhang, A novel definition of the multivariate coefficient of variation, *Biometrical Journal*, *52*, 667–675, 2010.

Ando, H., T. Imamura, T. Tsuda, S. Tellmann, M. Pätzold, and B. Häusler, Vertical wavenumber spectra of gravity waves in the Venus atmosphere obtained from Venus Express radio occultation data: Evidence for saturation, *J. Atmos. Sci.*, *72*, 2318–2329, 2015.

Angelats i Coll, M., F. Forget, M. A. López-Valverde, and F. González-Galindo, The first Mars thermospheric general circulation model: The Martian atmosphere from the ground to 240 km, *Geophysical Research Letters*, *32*, 4201–+, 2005.

Baird, D. T., R. Tolson, S. Bougher, and B. Steers, Zonal wind calculations from Mars Global Surveyor accelerometer and rate data, *Journal of Spacecraft and Rockets*, *44*, 1180–1187, 2007.

Barnes, J. R., R. M. Haberle, R. J. Wilson, S. R. Lewis, J. R. Murphy, and P. L. Read, *The Global Circulation*, p. 229–294, Cambridge Planetary Science, Cambridge University Press, 2017.

Bell, J. M., S. W. Bougher, and J. R. Murphy, Vertical dust mixing and the interannual variations in the Mars thermosphere, *Journal of Geophysical Research: Planets (1991–2012)*, *112*, 2007.

Benna, M., P. R. Mahaffy, J. M. Grebowsky, J. L. Fox, R. V. Yelle, and B. M. Jakosky, First measurements of composition and dynamics of the Martian ionosphere by MAVEN's Neutral Gas and Ion Mass Spectrometer, *Geophysical Research Letters*, *42*, 8958–8965, 2015.

Benna, M., S. W. Bougher, Y. Lee, K. J. Roeten, E. Yiğit, P. R. Mahaffy, and B. M. Jakosky, Global circulation of Mars' upper atmosphere, *Science*, *366*, 1363–1366, 2019.

Bertaux, J., et al., Nightglow in the upper atmosphere of Mars and implications for atmospheric transport, *Science*, *307*, 566–569, 2005.

Bougher, S., G. Keating, R. Zurek, J. Murphy, R. Haberle, J. Hollingsworth, and R. T. Clancy, Mars Global Surveyor aerobraking: Atmospheric trends and model interpretation, *Advances in Space Research*, *23*, 1887, 1999.

Bougher, S. W., R. G. Roble, E. C. Ridley, and R. E. Dickinson, The Mars thermosphere 2. General circulation with coupled dynamics and composition, *J. Geophys. Res.*, *95(B9)*, 14,811–14,827, 1990.

Bougher, S. W., C. G. Fesen, E. C. Ridley, and R. W. Zurek, Mars mesosphere and thermosphere coupling: Semidiurnal tides, *J. Geophys. Res.*, *95(E2)*, 3281—3295, 1993.

Bougher, S. W., S. Engel, R. G. Roble, and B. Foster, Comparative terrestrial planet thermospheres 2. Solar cycle variation of global structure and winds at equinox, *J. Geophys. Res.*, *1041*, 16,591–16,611, 1999.

Bougher, S. W., S. Engel, R. G. Roble, and B. Foster, Comparative terrestrial planet thermospheres 3. Solar cycle variation of global structure and winds at solstices, *J. Geophys. Res.*, *105*, 17,669–17,692, 2000.

Bougher, S. W., R. G. Roble, and T. Fuller-Rowell, Simulations of the upper atmospheres of the terrestrial planets, *Geophysical Monograph Series*, *130*, 261–288, 2002.

Bougher, S. W., J. M. Bell, J. R. Murphy, M. A. Lopez-Valverde, and P. G. Withers, Polar warming in the Mars thermosphere: Seasonal variations owing to changing insolation and dust distributions, *Geophys. Res. Lett.*, *330*, L02,203, 2006.

Bougher, S. W., T. M. McDunn, K. A. Zoldak, and J. M. Forbes, Solar cycle variability of Mars dayside exospheric temperatures: Model evaluation of underlying thermal balances, *Geophys. Res. Lett.*, *360*, L05,201, 2009.

Bougher, S. W., T. E. Cravens, J. Grebowksy, and J. Luhmann, The aeronomy of Mars: Characterization by MAVEN of the upper atmosphere reservoir that regulates volatile escape, *Space Sci. Reviews*, *195*, 423–456, 2015a.

Bougher, S. W., B. M. Jakosky, J. Halekas, J. Grebowsky, J. G. Luhmann, and others, Early MAVEN dip deep campaign reveals thermosphere and ionosphere variability, *Science*, *350*, 1–7, 2015b.

Bougher, S. W., D. Pawlowski, J. M. Bell, S. Nelli, T. McDunn, J. R. Murphy, M. Chizek, and A. Ridley, Mars global ionosphere-thermosphere model: Solar cycle, seasonal, and diurnal variations of the Mars upper atmosphere, *J. Geophys. Res.*, *120*, 311–342, 2015c.

Bougher, S. W., D. A. Brain, J. L. Fox, F. González-Galindo, C. Simon-Wedlund, and P. G. Withers, *Upper Neutral Atmosphere and Ionosphere*, p. 433–463, Cambridge Planetary Science, Cambridge University Press, 2017a.

Bougher, S. W., et al., The structure and variability of Mars dayside thermosphere from MAVEN NGIMS and IUVS measurements: Seasonal and solar activity trends in scale heights and temperatures, *Journal of Geophysical Research: Space Physics*, *122*, 1296–1313, 2017b.

Cantor, B. A., and M. C. Malin, MRO MARCI observations of the evolution of the 2018 planet-encircling dust event, in *AGU FM 2018*, 2018.

Cantor, B. A., P. B. James, M. Caplinger, and M. Wolff, Martian dust storms: 1999 Mars Orbiter camera observations, *Journal of Geophysical Research*, *106*, 653–687, 2001.

Chaufray, J.-Y., M. Chaffin, J. Deighan, S. Jain, N. Schneider, M. Mayyasi, and B. Jakosky, Effect of the 2018 Martian global dust storm on the CO_2 density in the lower nightside thermosphere observed from MAVEN/IUVS Lyman-alpha absorption, *Geophysical Research Letters*, *47*, e2019GL082,889, 2020.

Conrath, B. J., Thermal structure of the Martian atmosphere during the dissipation of the dust storm of 1971, *Icarus*, *24*, 36–46, 1975.

Creasey, J. E., J. M. Forbes, and G. M. Keating, Density variability at scales typical of gravity waves observed in Mars' thermosphere by the MGS accelerometer, *Geophysical Research Letters*, *33*, 2006.

Elrod, M. K., S. Bougher, J. Bell, P. R. Mahaffy, M. Benna, S. Stone, R. Yelle, and B. Jakosky, He bulge revealed: He and CO_2 diurnal and seasonal variations in the upper atmosphere of Mars as detected by MAVEN NGIMS, *Journal of Geophysical Research: Space Physics*, *122*, 2564–2573, 2017.

Elrod, M. K., S. M. Curry, E. M. B. Thiemann, and S. K. Jain, September 2017 solar flare event: Rapid heating of the Martian neutral upper atmosphere from the X-class flare as observed by MAVEN, *Geophysical Research Letters*, *45*, 8803–8810, 2018.

Elrod, M. K., S. W. Bougher, K. Roeten, R. Sharrar, and J. Murphy, Structural and compositional changes in the upper atmosphere related to the PEDE-2018 dust event on Mars as observed by MAVEN NGIMS, *Geophysical Research Letters*, *47*, e2019GL084,378, 2020.

England, S. L., G. Liu, E. Yiğit, P. R. Mahaffy, M. Elrod, M. Benna, H. Nakagawa, N. Terada, and B. Jakosky, MAVEN NGIMS observations of atmospheric gravity waves in the Martian thermosphere, *Journal of Geophysical Research: Space Physics*, *122*, 2310–2335, 2017.

Ergun, R. E., M. W. Morooka, L. A. Andersson, C. M. Fowler, G. T. Delory, D. J. Andrews, A. I. Eriksson, T. McEnulty, and B. M. Jakosky, Dayside electron temperature and density profiles at Mars: First results from the MAVEN Langmuir probe and waves instrument, *Geophysical Research Letters*, *42*, 8846–8853, 2015.

Fang, X., S. W. Bougher, R. E. Johnson, Y. Ma, and M. W. Liemohn, The importance of pickup oxygen ion precipitation to the Mars upper atmosphere under extreme solar wind conditions, *Geophys. Res. Lett.*, *40*, 1922–1927, 2013.

Fang, X., et al., Mars upper atmospheric responses to the 10 September 2017 solar flare: A global, time-dependent simulation, *Geophysical Research Letters*, *46*, 9334–9343, 2019.

Forbes, J. M., S. Bruinsma, and F. G. Lemoine, Solar rotation effects on the thermospheres of Mars and Earth, *Science*, *312*, 1366–1368, 2006.

Forbes, J. M., F. G. Lemoine, S. L. Bruinsma, M. D. Smith, and X. Zhang, Solar flux variability of Mars' exosphere densities and temperatures, *Geophysical Research Letters*, *35*, 2008.

Forbes, J. M., S. L. Bruinsma, E. Doornbos, and X. Zhang, Gravity wave-induced variability of the middle thermosphere, *J. Geophys. Res. Space Physics*, *121*, 6914–6923, 2016.

Forget, F., F. Montmessin, J.-L. Bertaux, F. González-Galindo, S. Lebonnois, E. Quermerais, A. Reberac, E. Dimarellis, and M. A. Lopez-Valverde, Density and temperatures of the upper Martian atmosphere measured by stellar occultations with Mars Express SPICAM, *J. Geophys. Res.*, *114*, 2009.

Fox, J. L., and K. Y. Sung, Solar activity variations of the Venus thermosphere/ionosphere, *J. Geophys. Res.*, *106*, 21,305–21,336, 2001.

Fritts, D. C., L. Wang, and R. H. Tolson, Mean and gravity wave structures and variability in the Mars upper atmosphere inferred from Mars Global Surveyor and Mars Odyssey aerobraking densities, *Journal of Geophysical Research: Space Physics (1978–2012)*, *111*, 2006.

Gagné, M.-E., J.-L. Bertaux, F. González-Galindo, S. M. L. Melo, F. Montmessin, and K. Strong, New nitric oxide (NO) nightglow measurements with SPICAM/MEx as a tracer of Mars upper atmosphere circulation and comparison with LMD-MGCM model prediction: Evidence for asymmetric hemispheres, *Journal of Geophysical Research: Planets*, *118*, 2172–2179, 2013.

Gkouvelis, L., J.-C. Gérard, F. González-Galindo, B. Hubert, and N. M. Schneider, Isobar altitude variations in the upper mesosphere observed with IUVS-MAVEN in response to Martian dust storms, *Geophysical Research Letters*, *47*, e2020GL087,468, 2020.

González-Galindo, F., G. Gilli, and M. A. López-Valverde, Nitrogen and ionospheric chemistry in the thermospheric LMD-MGCM, in *Third International Workshop on The Mars Atmosphere: Modeling and Observations*, p. 9007, 2008, lPI Contribution No. 1447.

González-Galindo, F., F. Forget, M. López-Valverde, M. Angelats i Coll, and E. Millour, A ground-to-exosphere Martian general circulation model: 1. Seasonal, diurnal, and solar cycle variation of thermospheric temperatures, *Journal of Geophysical Research: Planets*, *114*, 2009.

González-Galindo, F., F. Forget, M. A. López-Valverde, and M. Angelats i Coll, A ground-to-exosphere Martian general circulation model: 2. Atmosphere during solstice conditions–Thermospheric polar warming, *Journal of Geophysical Research (Planets)*, *114*, E08,004, 2009.

González-Galindo, F., S. W. Bougher, and M. e. a. López-Valverde, Thermal and wind structure of the Martian thermosphere as given by two general circulation models, *Planet. Space Sci.*, *58*, 1832–1849, 2010.

González-Galindo, F., J.-Y. Chaufray, M. A. López-Valverde, G. Gilli, F. Forget, F. Leblanc, R. Modolo, S. Hess, and M. Yagi, 3D Martian Ionosphere model: I. The photochemical ionosphere below 180 km, *Journal of Geophysical Research*, *118*, 2105–2123, 2013.

González-Galindo, F., M. A. López-Valverde, F. Forget, M. García-Comas, E. Millour, and L. Montabone, Variability of the Martian thermosphere during eight Martian years as simulated by a ground-to-exosphere global circulation model, *Journal of Geophysical Research: Planets*, *120*, 2020–2035, 2015.

Gu, H., J. Cui, D.-D. Niu, Y.-T. Cao, X.-S. Wu, J. Li, Z.-P. Wu, F. He, and Y. Wei, Neutral heating efficiency in the dayside Martian upper atmosphere, *The Astronomical Journal*, *159*, 39, 2020.

Guzewich, S. D., A. D. Toigo, M. I. Richardson, C. E. Newman, E. R. Talaat, D. W. Waugh, and T. H. McConnochie, The impact of a realistic vertical dust distribution on the simulation of the Martian general circulation, *Journal of Geophysical Research: Planets*, *118*, 980–993, 2013.

Haberle, R. M., J. L. Hollingsworth, A. Colaprete, A. F. C. Bridger, C. P. McKay, J. R. Murphy, J. Schaeffer, and R. Freedman, The NASA/AMES Mars General Circulation Model: Model Improvements and comparison with observations, in *Published Conference Abstract, International Workshop: Mars Atmosphere Modelling and Observations*, 2003.

Haberle, R. M., et al., General circulation model simulations of the Mars Pathfinder atmospheric structure investigation/meteorology data, *Journal of Geophysical Research*, *104*, 8957–8974, 1999.

Hartogh, P., A. S. Medvedev, T. Kuroda, R. Saito, G. Villanueva, A. G. Feofilov, A. A. Kutepov, and U. Berger, Description and climatology of a new general circulation model of the Martian atmosphere, *Journal of Geophysical Research: Planets*, *110*, 2005.

Heavens, N. G., D. J. McCleese, M. I. Richardson, D. M. Kass, A. Kleinböhl, and J. T. Schofield, Structure and dynamics of the Martian lower and middle atmosphere as observed by the Mars Climate Sounder: 2. Implications of the thermal structure and aerosol distributions for the mean meridional circulation, *Journal of Geophysical Research: Planets*, *116*, 2011a.

Heavens, N. G., D. M. Kass, A. Kleinböhl, and J. T. Schofield, A multiannual record of gravity wave activity in Mars's lower atmosphere from on-planet observations by the Mars Climate Sounder, *Icarus*, *341*, 113,630, 2020.

Heavens, N. G., A. Pankine, J. M. Battalio, C. Wright, D. M. Kass, A. Kleinböhl, S. Piqueux, and J. T. Schofield, Mars Climate Sounder observations of gravity wave activity throughout Mars's lower atmosphere, *The Planetary Science Journal*, *3*, 57, 2022.

Heavens, N. G., et al., The vertical distribution of dust in the Martian atmosphere during northern spring and summer: Observations by the Mars Climate Sounder and analysis of zonal average vertical dust profiles, *Journal of Geophysical Research: Planets*, *116*, 2011b.

Hinson, D., M. Pätzold, S. Tellmann, B. Häusler, and G. Tyler, The depth of the convective boundary layer on Mars, *Icarus*, *198*, 57–66, 2008.

Holton, J. R., *An introduction to dynamic meteorology*, International Geophysics Series, 4 ed., Elsevier Academic Press,, Burlington, MA, 2004.

Hughes, J., F. Gasperini, and J. M. Forbes, Solar rotation effects in martian thermospheric density as revealed by five years of MAVEN observations, *Journal of Geophysical Research: Planets*, *127*, e2021JE007,036, 2022.

Jain, S., E. Soto, J. Evans, J. Deighan, N. Schneider, and S. Bougher, Thermal structure of Mars' middle and upper atmospheres: Understanding the impacts of dynamics and solar forcing, *Icarus*, p. 114703, 2021.

Jain, S. K., et al., The structure and variability of Mars upper atmosphere as seen in MAVEN/IUVS dayglow observations, *Geophys. Res. Lett.*, *42*, 9023–9030, 2015.

Jain, S. K., et al., Martian thermospheric response to an X8.2 solar flare on 10 September 2017 as seen by MAVEN/IUVS, *Geophysical Research Letters*, *45*, 7312–7319, 2018.

Jain, S. K., et al., Martian thermospheric warming associated with the planet encircling dust event of 2018, *Geophysical Research Letters*, *47*, e2019GL085,302, 2020.

Jakosky, B. M., R. P. Lin, J. M. Grebowksy, J. G. Luhmann, and others, The Mars Atmosphere and Volatile Evolution (MAVEN) Mission, *Space Sci. Reviews*, *195*, 3–48, 2015.

Jesch, D., A. S. Medvedev, F. Castellini, E. Yiğit, and P. Hartogh, Density fluctuations in the lower thermosphere of Mars retrieved from the ExoMars Trace Gas Orbiter (TGO) aerobraking, *Atmosphere*, *10*, 620, 2019.

Kahre, M. A., J. R. Murphy, C. E. Newman, R. J. Wilson, B. A. Cantor, M. T. Lemmon, and M. J. Wolff, *The Mars Dust Cycle*, p. 295–337, Cambridge Planetary Science, Cambridge University Press, 2017.

Kass, D. M., A. Kleinböhl, D. J. McCleese, J. T. Schofield, and M. D. Smith, Interannual similarity in the Martian atmosphere during the dust storm season, *Geophysical Research Letters*, *43*, 6111–6118, 2016.

Kass, D. M., J. T. Schofield, A. Kleinböhl, D. J. McCleese, N. G. Heavens, J. H. Shirley, and L. J. Steele, Mars Climate Sounder Observation of Mars' 2018 global dust storm, *Geophysical Research Letters*, *47*, e2019GL083,931, 2020.

Keating, G., S. Bougher, M. Theriot, R. Tolson, R. Zurek, R. Blanchard, J. Murphy, and J.-L. Bertaux, Mars neutral upper atmosphere temporal and spatial variations discovered from the accelerometer science experiment aboard Mars Reconnaissance Orbiter, in *Lunar and Planetary Institute Science Conference Abstracts*, vol. 38, p. 2074, 2007.

Keating, G. M., and E. J. Prior, The winter helium bulge, *Space Res.*, *8*, 982–992, 1968.

Keating, G. M., et al., The structure of the upper atmosphere of Mars: In situ accelerometer measurements from Mars Global Surveyor, *Science*, *279*, 1672–1676, 1998.

Kleinböhl, A., et al., Mars Climate Sounder limb profile retrieval of atmospheric temperature, pressure, and dust and water ice opacity, *Journal of Geophysical Research*, *114*, E10,006, 2009.

Kuroda, T., A. S. Medvedev, E. Yiğit, and P. Hartogh, A global view of gravity waves in the Martian atmosphere inferred from a high-resolution general circulation model, *Geophysical Research Letters*, *42*, 9213–9222, 2015.

Kuroda, T., A. S. Medvedev, E. Yiğit, and P. Hartogh, Global distribution of gravity wave sources and fields in the Martian atmosphere during equinox and solstice inferred from a high-resolution general circulation model, *Journal of the Atmospheric Sciences*, *73*, 4895 – 4909, 2016.

Kuroda, T., A. S. Medvedev, and E. Yiğit, Gravity wave activity in the atmosphere of Mars during the 2018 global dust storm: Simulations with a high-resolution model, *Journal of Geophysical Research: Planets*, *125*, e2020JE006,556, 2020.

Leblanc, F., J. Y. Chaufray, J. Lilensten, O. Witasse, and J.-L. Bertaux, Martian dayglow as seen by the SPICAM UV spectrograph on Mars Express, *Journal of Geophysical Research*, *111*, 2006.

Leelavathi, V., N. Venkateswara Rao, and S. V. B. Rao, Interannual variability of atmospheric gravity waves in the Martian thermosphere: Effects of the 2018 planet-encircling dust event, *J. Geophys. Res. Planets*, *125*, e2020JE006,649, 2020.

Lewis, S. R., M. Collins, P. L. Read, F. Forget, F. Hourdin, R. Fournier, C. Hourdin, O. Talagrand, and J.-P. Huot, A climate database for Mars, *J. Geophys. Res.*, *104*, 24,177–24,194, 1999.

Lilienthal, F., E. Yiğit, N. Samtleben, and C. Jacobi, Variability of gravity wave effects on the zonal mean circulation and migrating terdiurnal tide as studied with the middle and upper atmosphere model (MUAM2019) using a nonlinear gravity wave scheme, *Front. Astron. Space Sci.*, *2020*, 7:588,956, 2020.

Lillis, R. J., S. W. Bougher, F. González-Galindo, F. Forget, M. D. Smith, and P. C. Chamberlin, Four Martian years of nightside upper thermospheric mass densities derived from electron reflectometry: Method extension and comparison with GCM simulations, *Journal of Geophysical Research: Planets*, *115*, 2010.

Liu, X., W. Wang, J. P. Thayer, A. Burns, E. Sutton, S. C. Solomon, L. Qian, and G. Lucas, The winter helium bulge revisited, *Geophysical Research Letters*, *41*, 6603–6609, 2014.

Mahaffy, P. R., M. Benna, M. Elrod, R. V. Yelle, S. W. Bougher, S. W. Stone, and B. M. Jakosky, Structure and composition of the neutral upper atmosphere of Mars from the MAVEN NGIMS investigation, *Geophys. Res. Lett.*, *42*, 8951–8957, 2015a.

Mahaffy, P. R., M. Benna, T. King, D. N. Harpold, and R. e. a. Arvey, The Neutral Gas and Ion Mass Spectrometer on the Mars Atmosphere and Volatile Evolution Mission, *Space Sci. Reviews*, *195*, 49–73, 2015b.

Martinez, G., et al., The modern near-surface Martian climate: A review of in-situ meteorological data from Viking to Curiosity, *Space Science Reviews*, *212*, 295–338, 2017.

McCleese, D., et al., Structure and dynamics of the Martian lower and middle atmosphere as observed by the Mars Climate Sounder: Seasonal variations in zonal mean temperature, dust, and water ice aerosols, *Journal of Geophysical Research: Planets (1991–2012)*, *115*, 2010.

McDunn, T. L., S. W. Bougher, J. Murphy, M. D. Smith, F. Forget, J.-L. Bertaux, and F. Montmessin, Simulating the density and thermal structure of the middle atmosphere (80-130 km) of Mars using the MGCM-MTGCM: A comparison with MEX/SPICAM observations, *Icarus*, *206*, 5–17, 2010.

Medvedev, A. S., and G. P. Klaassen, Parameterization of gravity wave momentum deposition based on nonlinear wave interactions: Basic formulation and sensitivity tests, *Journal of Atmospheric and Solar-Terrestrial Physics*, *62*, 1015–1033, 2000.

Medvedev, A. S., and E. Yiğit, Thermal effects of internal gravity waves in the Martian upper atmosphere, *Geophys. Res. Lett.*, *39*, 2012.

Medvedev, A. S., and E. Yiğit, Gravity waves in planetary atmospheres: Their effects and parameterization in global circulation models, *Atmosphere*, *10*, 2019.

Medvedev, A. S., E. Yiğit, and P. Hartogh, Estimates of gravity wave drag on Mars: indication of a possible lower thermosphere wind reversal, *Icarus*, *211*, 909–912, 2011a.

Medvedev, A. S., E. Yiğit, P. Hartogh, and E. Becker, Influence of gravity waves on the Martian atmosphere: General circulation modeling, *J. Geophys. Res.*, *116*, 2011b.

Medvedev, A. S., E. Yiğit, T. Kuroda, and P. Hartogh, General circulation modeling of the Martian upper atmosphere during global dust storms, *J. Geophys. Res. Planets*, *118*, 1–13, 2013.

Medvedev, A. S., F. González-Galindo, E. Yiğit, A. G. Feofilov, F. Forget, and P. Hartogh, Cooling of the Martian thermosphere by CO_2 radiation and gravity waves: An intercomparison study with two general circulation models, *J. Geophys. Res. Planets*, *120*, 913–927, 2015.

Medvedev, A. S., E. Yiğit, and P. Hartogh, Ion friction and quantification of the geomagnetic influence on gravity wave propagation and dissipation in the thermosphere-ionosphere, *J. Geophys. Res. Space Physics*, *122*, 12,464–12,475, 2017.

Medvedev, A. S., et al., Comparison of the Martian thermospheric density and temperature from IUVS/MAVEN data and general circulation modeling, *Geophys. Res. Lett.*, *43*, 3095–3104, 2016.

Miyoshi, Y., and E. Yiğit, Impact of gravity wave drag on the thermospheric circulation: Implementation of a nonlinear gravity wave parameterization in a whole atmosphere model, *Annales Geophysicae*, *37*, 955–969, 2019.

Montmessin, F., F. Forget, P. Rannou, M. Cabane, and R. Haberle, Origin and role of water ice clouds in the Martian water cycle as inferred from a general circulation model, *Journal of Geophysical Research: Planets (1991–2012)*, *109*, 2004.

Montmessin, F., et al., Subvisible CO_2 ice clouds detected in the mesosphere of Mars, *Icarus*, *183*, 403–410, 2006.

Määttänen, A., et al., Mapping the mesospheric CO_2 clouds on Mars: MEx/OMEGA and MEx/HRSC observations and challenges for atmospheric models, *Icarus*, *209*, 452–469, 2010.

National Academies of Sciences, a. M., Engineering, *Vision and Voyages for Planetary Science in the Decade 2013-2022*, The National Academies Press, Washington, DC, 2011.

National Academies of Sciences, a. M., Engineering, *Origins, Worlds, Life: A Decadal Strategy for Planetary Science and Astrobiology 2023-2032*, The National Academies Press, Washington, DC, 2022.

Nier, A., and M. B. McElroy, Composition and structure of Mars' upper atmosphere: Results from the neutral mass spectrometers on Viking 1 and 2, *Journal of Geophysical Research*, *82*, 4341–4349, 1977.

Parish, H. F., G. Schubert, M. Hickey, and R. L. Walterscheid, Propagation of tropospheric gravity waves into the upper atmosphere of Mars, *Icarus*, *203*, 28–37, 2009.

Ridley, A., Y. Deng, and G. Tòth, The global ionosphere-thermosphere model, *J. Atmos. Sol-Terr. Phys.*, *68*, 839, 2006.

Roeten, K. J., S. W. Bougher, M. Benna, P. R. Mahaffy, Y. Lee, D. Pawlowski, F. González-Galindo, and M. A. López-Valverde, MAVEN/NGIMS thermospheric neutral wind observations: Interpretation using the M-GITM general circulation model, *Journal of Geophysical Research: Planets*, *124*, 3283–3303, 2019.

Roeten, K. J., S. W. Bougher, M. Benna, and M. K. Elrod, MAVEN/NGIMS wind observations in the Martian thermosphere during the 2018 planet encircling dust event, *Icarus*, *382*, 115,006, 2022a.

Roeten, K. J., S. W. Bougher, E. Yiğit, A. Medvedev, M. Benna, and M. K. Elrod, Impacts of gravity waves in the Martian thermosphere: The Mars Global Ionosphere-Thermosphere Model coupled with a whole atmosphere gravity wave scheme, *Journal of Geophysical Research: Planets*, 2022b.

Rohrbaugh, R., J. Nisbet, E. Bleuler, and J. Herman, The effect of energetically produced O_2^+ on the ion temperatures of the Martian thermosphere, *Journal of Geophysical Research: Space Physics*, *84*, 3327–3338, 1979.

Sakib, M. N., and E. Yiğit, A brief overview of gravity wave retrieval techniques from observations, *Front. Astron. Space Sci.*, *9*, 2022.

Schneider, N. M., et al., Imaging of Martian circulation patterns and atmospheric tides through MAVEN/IUVS nightglow observations, *Journal of Geophysical Research: Space Physics*, *125*, e2019JA027,318, 2020.

Schunk, R., and A. Nagy, *Ionospheres: Physics, Plasma Physics, and Chemistry*, Cambridge Atmospheric and Space Science Series, 2 ed., Cambridge University Press, 2009.

Seidelmann, P. K., et al., Report of the IAU/IAG working group on cartographic coordinates and rotational elements of the planets and satellites: 2000, *Celestial Mechanics and Dynamical Astronomy*, *82*, 83–111, 1/2002.

Shaposhnikov, D. S., A. S. Medvedev, A. V. Rodin, and P. Hartogh, Seasonal water "pump" in the atmosphere of Mars: Vertical transport to the thermosphere, *Geophys. Res. Lett.*, *46*, 4161–4169, 2019.

Shaposhnikov, D. S., A. S. Medvedev, A. V. Rodin, E. Yiğit, and P. Hartogh, Martian dust storms and gravity waves: Disentangling water transport to the upper atmosphere, *J. Geophys. Res. Planets*, *127*, 2022.

Siddle, A., I. Mueller-Wodarg, S. Stone, and R. Yelle, Global characteristics of gravity waves in the upper atmosphere of Mars as measured by MAVEN/NGIMS, *Icarus*, *333*, 12–21, 2019.

Smith, M. D., THEMIS observations of Mars aerosol optical depth from 2002-2008, *Icarus*, *202*, 444–452, 2009.

Snowden, D., R.-V. Yelle, J. Cui, J.-E. Wahlund, N. J. T. Edberg, and K. Agren, The thermal structure of Titan's upper atmosphere: 1. Temperature profiles from Cassini INMS observations, *Icarus*, *226*, 552–582, 2013.

Starichenko, E. D., et al., Gravity wave activity in the Martian atmosphere at altitudes 20–160 km from ACS/TGO occultation measurements, *Journal of Geophysical Research: Planets*, *126*, e2021JE006,899, 2021.

Stewart, A. I., Mariner 6 and 7 ultraviolet spectrometer experiment: Implications for CO_2^+, CO, and O airglow, *Journal of Geophysical Research*, *77*, 1, 1972.

Stewart, A. I., C. Barth, C. Hord, and A. Lane, Mariner 9 ultraviolet spectrometer experiment: Structure of Mars' upper atmosphere, *Icarus*, *17*, 469–474, 1972.

Stiepen, A., et al., Nitric oxide nightglow and Martian mesospheric circulation from MAVEN/IUVS observations and LMD-MGCM predictions, *Journal of Geophysical Research: Space Physics*, *122*, 5782–5797, 2017.

Stone, S. W., R. V. Yelle, M. Benna, M. K. Elrod, and P. R. Mahaffy, Thermal structure of the Martian upper atmosphere from MAVEN NGIMS, *Journal of Geophysical Research: Planets*, *123*, 2842–2867, 2018.

Sánchez-Lavega, A., T. del Río-Gaztelurrutia, J. Hernández-Bernal, and M. Delcroix, The onset and growth of the 2018 Martian global dust storm, *Geophysical Research Letters*, *46*, 6101–6108, 2019.

Terada, N., et al., Global distribution and parameter dependences of gravity wave activity in the Martian upper thermosphere derived from MAVEN/NGIMS observations, *Journal of Geophysical Research: Space Physics*, *122*, 2374–2397, 2017.

Thiemann, E. M. B., P. C. Chamberlin, F. G. Eparvier, B. Templeman, T. N. Woods, S. W. Bougher, and B. M. Jakosky, The MAVEN EUVM model of solar spectral irradiance variability at Mars: Algorithms and results, *Journal of Geophysical Research: Space Physics*, *122*, 2748–2767, 2017.

Thiemann, E. M. B., F. G. Eparvier, S. W. Bougher, M. Dominique, L. Andersson, Z. Girazian, M. D. Pilinski, B. Templeman, and B. M. Jakosky, Mars thermospheric variability revealed by MAVEN EUVM solar occultations: Structure at aphelion and perihelion and response to EUV forcing, *Journal of Geophysical Research: Planets*, *123*, 2248–2269, 2018.

Tolson, R., A. Dwyer, J. Hanna, G. Keating, B. George, P. Escalera, and M. Werner, Application of accelerometer data to Mars Odyssey aerobraking and atmospheric modeling, *Journal of Spacecraft and Rockets*, *42*, 435–443, 2005.

Tolson, R., G. Keating, R. Zurek, S. Bougher, C. Justus, and D. Fritts, Application of acclerometer data to atmospheric modeling during Mars aerobraking operations, *Journal of Spacecraft and Rockets*, *44*, 1172–1179, 2007.

Vals, M., A. Spiga, F. Forget, E. Millour, L. Montabone, and F. Lott, Study of gravity waves distribution and propagation in the thermosphere of Mars based on MGS, ODY, MRO, and MAVEN density measurements, *Planetary and Space Science*, *178*, 104,708, 2019.

Venkateswara Rao, N., N. Gupta, and U. R. Kadhane, Enhanced densities in the Martian thermosphere associated with the 2018 planet-encircling dust event: Results from MENCA/MOM and NGIMS/MAVEN, *Journal of Geophysical Research: Planets*, *125*, e2020JE006,430, 2020.

Watanabe, S., and S. Miyahara, Quantification of the gravity wave forcing of the migrating diurnal tide in a gravity wave–resolving general circulation model, *J. Geophys. Res.*, *114*, 2009.

Winchester, C., and D. Rees, Numerical models of the Martian coupled thermosphere and ionosphere, *Advances in Space Research*, *15*, 51 – 68, 1995.

Wu, Z., T. Li, N. G. Heavens, C. E. Newman, M. I. Richardson, C. Yang, J. Li, and J. Cui, Earth-like thermal and dynamical coupling processes in the Martian climate system, *Earth-Science Reviews*, *229*, 104,023, 2022.

Yiğit, E., A. S. Medvedev, and P. Hartogh, Variations of the martian thermospheric gravity-wave activity during the recent solar minimum as observed by MAVEN, *APJ*, *920*, 69, 2021.

Yiğit, E., and A. S. Medvedev, Heating and cooling of the thermosphere by internal gravity waves, *Geophys. Res. Lett.*, *36*, 2009.

Yiğit, E., and A. S. Medvedev, Internal wave coupling processes in Earth's atmosphere, *Adv. Space Res.*, *55*, 983–1003, 2015.

Yiğit, E., and A. S. Medvedev, Obscure waves in planetary atmospheres, *Physics Today*, *6*, 40–46, 2019.

Yiğit, E., A. D. Aylward, and A. S. Medvedev, Parameterization of the effects of vertically propagating gravity waves for thermosphere general circulation models: Sensitivity study, *J. Geophys. Res.*, *113*, 2008.

Yiğit, E., A. S. Medvedev, A. D. Aylward, P. Hartogh, and M. J. Harris, Modeling the effects of gravity wave momentum deposition on the general circulation above the turbopause, *J. Geophys. Res.*, *114*, 2009.

Yiğit, E., A. S. Medvedev, and P. Hartogh, Influence of gravity waves on the climatology of high-altitude Martian carbon dioxide ice clouds, *Annales Geophysicae*, *36*, 1631–1646, 2018.

Yiğit, E., A. S. Alexander, and M. Ern, Effects of latitude-dependent gravity wave source variations on the middle and upper atmosphere, *Front. Astron. Space Sci.*, *7*, 2021a.

Yiğit, E., A. S. Medvedev, M. Benna, and B. M. Jakosky, Dust storm-enhanced gravity wave activity in the Martian thermosphere observed by MAVEN and implications for atmospheric escape, *Geophysical Research Letters*, *48*, e2020GL092,095, 2021b.

Yiğit, E., S. L. England, G. Liu, A. S. Medvedev, P. R. Mahaffy, T. Kuroda, and B. M. Jakosky, High-altitude gravity waves in the Martian thermosphere observed by MAVEN/NGIMS and modeled by a gravity wave scheme, *Geophysical Research Letters*, *42*, 8993–9000, 2015.

Zurek, R. W., R. A. Tolson, S. W. Bougher, R. A. Lugo, D. T. Baird, J. M. Bell, and B. M. Jakosky, Mars thermosphere as seen in MAVEN accelerometer data, *Journal of Geophysical Research: Space Physics*, *122*, 3798–3814, 2017.